MULTI-FIDELITY DESIGN OF AN INTEGRAL THERMAL PROTECTION SYSTEM FOR FUTURE SPACE VEHICLE DURING RE-ENTRY

By

ANURAG SHARMA

A DISSERTATION PRESENTED TO THE GRADUATE SCHOOL
OF THE UNIVERSITY OF FLORIDA IN PARTIAL FULFILLMENT
OF THE REQUIREMENTS FOR THE DEGREE OF
DOCTOR OF PHILOSOPHY

UNIVERSITY OF FLORIDA

2010

To my parents Jagdish Prasad Sharma and Sujata Sharma, sister Shraddha Sharma and all my family members

ACKNOWLEDGMENTS

I would like to acknowledge my advisors Dr. Bhavani Sankar and Dr. Raphael T. Haftka for all their tutelage, support, and encouragement. Their patience in dealing with the thousands of questions I had for them throughout the course of this research and their advice were invaluable. I also sincerely thank my dissertation committee members Dr. Peter Ifju, Dr. Nam Ho Kim and Dr. Jack Mecholsky for evaluating my research work and my candidature for the PhD degree. I would also like to thank specially Dr. Kim for his course on Advanced Finite Element Methods which helped me in understanding the basics on how to write the input files in ABAQUS®. Finally I would like to thank all my fellow lab mates.

TABLE OF CONTENTS

page

LIST OF TABLES

Table page

LIST OF FIGURES

LIST OF ABBREVIATIONS

AFRSI	advanced flexible reusable surface insulation
ARMOR	advanced-adapted, robust, metallic, operable, reusable
CEV	crew exploration vehicle
CRS	correction response surface
FEA	finite element analysis
FEM	finite element method
FRCI	fibrous refractory composite insulation
HRSI	high-temperature reusable surface insulation
ITPS	integrated thermal protection system
LRSI	low-temperature reusable surface insulation
NASA	National Aeronautics and Space Administration
PRS	polynomial response surface
RCC	reinforced carbon-carbon
RLV	reusable launch vehicle
RSA	response surface approximations
RSI	reusable surface insulation
SSTO	single-stage-to-orbit
TPS	thermal protection system
2D	two-dimensional
3D	three-dimensional

LIST OF SYMBOLS

a	panel length (x-direction)
A_{44}	shearing stiffness (y-direction)
A_{55}	shearing stiffness (x-direction)
$[A]$	extensional stiffness matrix
$[B]$	coupling stiffness matrix
b	panel width (y-direction)
$[D]$	bending stiffness matrix
$D_{11}^{'}$	reduced stiffness matrix (x-direction)
$D_{22}^{'}$	reduced stiffness matrix (y-direction)
d	height of the sandwich panel
ε_0	midplane strain
κ	curvature
L_{ex}	length of the cantilever beam (x-direction)
L_{ey}	length of the cantilever beam (y-direction)
M	moment resultant
M^T	thermal moment resultant
N	force resultant
N^T	thermal force resultant
$2p$	unit cell length
P_o	pressure acting on the cantilever beam
Q_x, Q_y	transverse shear force
s	web length
t_T, t_{TF}	top face sheet thickness
t_{BF}	bottom face sheet thickness

t_W	web thickness
θ	web inclination
u	unit cell displacement (x-direction)
$u_0\ (x,y)$	mid-plane displacement (x-direction)
v	unit cell displacement (y-direction)
$v_0\ (x,y)$	mid-plane displacement (y-direction)
w	unit cell vertical displacement (z-direction)
$\psi_x(x,y), \psi_y(x,y)$	rotations of plate's cross section
θ_x, θ_y	global rotations
γ_{xz}, γ_{yz}	transverse shear strains
$S_{Multi-Fidelity}$	multi-fidelity response surface approximations
S^{3D}	high-fidelity response surface approximations
S^{2D}	low-fidelity response surface approximations
S^{Diff_CRS}	CRS based on the difference between 3D and 2D
S^{Ratio_CRS}	CRS based on the ratio between 3D and 2D

Abstract of Dissertation Presented to the Graduate School
of the University of Florida in Partial Fulfillment of the
Requirements for the Degree of Doctor of Philosophy

MULTI-FIDELITY DESIGN OF AN INTEGRAL THERMAL PROTECTION SYSTEM FOR FUTURE SPACE VEHICLE DURING RE-ENTRY

By

Anurag Sharma

December 2010

Chair: Bhavani V. Sankar
Co-Chair: Raphael T. Haftka
Major: Mechanical Engineering

The primary function of a thermal protection system (TPS) is to protect the space vehicle from extreme aerodynamic heating and to maintain the underlying structure within acceptable temperature limits. Currently used TPS are not load bearing members. One potential method of saving weight is to have a load-bearing TPS that performs both thermal and structural functions. One such concept called the Integrated Thermal Protection System (ITPS) uses a corrugated-core sandwich structure. Optimization of an ITPS requires thousands of three-dimensional (high-fidelity model) simulations, which is very expensive. Hence, a finite element (FE) based homogenization procedure is developed in which the ITPS is modeled as an equivalent orthotropic plate. The results for deflection and stresses obtained using the plate model (low fidelity model) are not very accurate. The high-fidelity model is analyzed at only few designs in order to reduce the cost, and these results in errors in the response surfaces based only on the high-fidelity model. To resolve this difficulty, the low fidelity two-dimensional (2D) plate models is fitted with a high quality surrogate, which is then corrected by using a small number of high fidelity three-dimensional (3D) finite element

analyses. Fitting the difference or the ratio between the high fidelity analyses and the low fidelity surrogate with a response surface approximation allows construction of the so called correction response surface. This multi-fidelity or variable-complexity modeling requires significantly fewer high fidelity analyses for a given accuracy.

A MATLAB® and a JAVA code has been developed in conjunction with the Surrogate Toolbox in order to carry out these FE analyses automatically using ABAQUS®. The multi-fidelity response surface approximation (RSA) is used to optimize the mass of the ITPS for a given material combination and loading conditions. For the same given accuracy, multi-fidelity response surface took 30 percent less time as compared to the full 3D response surface. Further, one can choose the best correction model based on the data without the test points, and the test points also confirmed the choice.

CHAPTER 1
INTRODUCTION

Motivation

Space exploration has always been a source of national pride for United States as well for others. It is a valuable tool in our quest to understand the universe. The Hubble Space Telescope provides us with an understanding of the history of our galaxy and offers a glimpse into others. Satellite programs like Solar Radiation and Climate Experiment (SORCE) and Gravity Recovery and Climate Experiment (GRACE) gives us the ability to fully take on the climate change crisis as a nation and a world. The capabilities of spacecraft and other high-speed flight vehicles are being taken to exciting new levels with ventures like the International Space Station and commercial space programs like the ongoing space tourism and space-based communications. As we try to fly farther, faster and more often, reusability of these flight vehicles becomes of greater importance due to their reduced costs and decreased turnaround time between flights. It is therefore important that decreasing the cost of launching a space vehicle is one of the vital requirements of the space industry. The use of space is becoming more regular, therefore future space vehicle needs to be completely reusable, have higher functional extensibility, and have a lower running cost than the existing Space Shuttle [5].

One of the NASA's foremost goals has been to lessen the cost of carrying a pound of payload by an order of magnitude [6]. It has been found that a single-stage-to-orbit (SSTO) reusable launch vehicle (RLV) can help to achieve this target. Regardless of many challenges and difficulties, SSTO is something worth trying with such an increased demand for space access. An expendable rocket vehicle, such as the

Russian Proton and US Delta offers one of the least costly ways to deliver a payload with the payload cost varying from $4,000 to $20,000 per pound [7], but for every launch a completely new launch vehicle is required. A major step towards reusability starts with the improvement of the thermal protection system (TPS) of these vehicles. As we push our boundaries beyond earth's lower orbit to Mars and beyond, new space vehicles such as hypersonic Crew Exploration Vehicle (CEV), air breathing vehicles [1], military space planes [2] and unmanned experiment return capsules [3] are being developed, and TPS will be occupying a huge area on the exteriors and will form the primary part of the launch weight. Since the TPS is such an expensive and intrinsic part of the design of space vehicles [4], there will be new and interesting ideas to explore for years to come.

The Space Shuttle which is not fully reusable, offers a good but a costly launch system. One of the most expensive maintenance systems for the Shuttle Orbiter is the TPS. Between flights the approximate maintenance time is 40,000 hours [8, 9]. Lockheed Martin came up with an SSTO design, i.e. Venture Star, which could reduce the cost of launching a satellite by 1/10th as compared to the Space Shuttle [10]. However, due to many technological challenges the program was cancelled. Currently, NASA is planning to use Ares I to launch Orion, the spacecraft being designed for NASA human space flight missions after the Space Shuttle is retired in 2010.

It has been widely confirmed by the aerospace community that altogether independent, reusable single-stage vehicle could decrease the costs considerably. In future the reusable SSTOs would be the main focus of research as the cost of each launch will be lessened by making a reusable sophisticated vehicle that launches at

regular quick intervals with minimal maintenance. Such vehicles will have an ample region to be covered with TPS, because the fuel tanks will be an integral part required for launch. As a result of the massive TPS coverage region, a need for a lightweight TPS is essential to keep the vehicle launch cost and weight moderate and affordable. The major reduction in the payload delivering costs is the rationale for the advancement of a future space vehicle.

Thermal Protection System

Thermal Protection System (TPS) is the barrier that shields the space vehicle from aerodynamic heating during atmospheric reentry. The atmospheric gas causes surface friction and compression on the vehicle surface which results in high aerodynamic heating. The vehicle's structure and entry path in combination with the kind of thermal protection system used characterize the vehicle’s temperature distribution [18]. High reentry speeds greater than Mach 20 causes such heating, which is adequate enough to damage the vehicle structure. The previous space vehicles such as Mercury, Gemini, and Apollo had blunt bodies to give a “stand-off bow shock” [11 – 17]. The result is that most of the heat is expended to the surrounding air. Furthermore, these vehicles had ablative materials that change directly into gas at high temperature. The sublimation action consumes thermal energy from high aerodynamic heating and wears away the material from the surface. Thermal blankets and insulating tiles are used on the bottom region of the Space Shuttle [9, 19] to consume and radiate heat while blocking conduction to the aluminum substructure. It consists of approximately 25,000 tiles which act as a heat resistant blanket. The black tiles on the bottom of the orbiter should be able to bear 2,000 ^{o}F during reentry. During reentry, shock waves are generated on the orbiter and those tiles are needed to protect the aluminum skin of the orbiter, which

cannot withstand temperatures over 350 ^{o}F without structural failure. Since the temperatures can go up to 2,000 ^{o}F, this four inch thick tile has to dissipate a large amount of heat. Further, these tiles are attached to the orbiter aluminum structure with a strain isolation pad in between. If these tiles are attached directly to the aluminum, any strains such as mechanical or thermal in the aluminum may cause substantial tensile strains in the tiles, which could cause cracking.

Requirements for a Thermal Protection System

The principal objective of a TPS is to keep the temperature of the underlying structure within specified limits. The TPS should be shielded from different types of environments like the ground lightning strike, hail strike, bird strike, and on-orbit debris/micro-meteoroid hypervelocity impact, etc [10]. The basic requirements that the TPS should satisfy are given below and are similar to that mentioned in [20, 21].

Thermal Loading: TPS is subjected to varying temperature distributions. At a given time, the side facing the sun will have a temperature of about 250 ^{o}F and the side away from the sun will be at about -150 ^{o}F. TPS panels which are attached to cryogenic fuel tanks are subjected to low temperatures before takeoff and also in space. Such varying temperatures cause temperature gradient which can result in very high thermal stresses and can also cause creep and other inelastic behavior at elevated temperatures. In order to prevent the vehicle from catastrophic failure, the TPS should be able to bear such varying temperatures at all flight environments [22].

Aerodynamic Pressure Load: The flight environments and space vehicle location determine if the aerodynamic pressure load pulls the TPS panel off the vehicle or be compressive in nature. The compressive pressure load could cause the outer surface, loading attachments, and support hardware to bend considerably and thereby changing

the aerodynamic shape of the vehicle. The TPS should be able to avoid failure and fracture under these varying pressure loads [10].

Panel Deformations: The panel deflection should be within acceptable bounds under any given loading condition. The deformation could occur due to pressure, thermal bowing or acoustic and dynamic loads. Depending on the space vehicle location and flight environments, the deformation can vary considerably. However, for any condition, premature transformation to turbulence (which would greatly escalate the surface heating) [9], should be averted in order to maintain a suitable aerodynamic surface.

Foreign Object Impact: TPS must be able to bear any foreign particle collision under any flight environments. The impingement could be during launch and landing from low speed debris, impacts at hypervelocity from on-orbit debris or/and from weather related impacts such as hail and rain. The Space Shuttle Columbia was one of the victims of such debris impact on the TPS tiles. The debris struck the leading edge of the left wing, damaging the Shuttle's thermal protection system (TPS) [28] (Figure 1-1).

Chemical Corrosion: At very extreme temperatures, TPS materials become sensitive to oxidation. TPS properties may change significantly due to this chemical attack. This results in further degradation in structural performance and temperature capabilities. TPS material should be resistant towards chemical corrosion.

For RLV's, decreasing the mass of the TPS has been the primary focus for making the efficiency better. Vehicle with reduced mass requires fewer energy and fuel, thereby carrying more payloads. Vehicle's performance can be increased further

by using a better material and coating to enhance TPS performance so that it could perform in more extreme thermal environments.

Decreasing the cost of the TPS has become a main issue, with more use of RLV's for various civilian and military applications. Enhanced design and newer analysis procedures, approaches, materials, coatings and fabrication and installation methods need to be evolved in order to lessen the costs [9]. Cost reduction could be increased further by making it more durable and robust. Further improving these attributes will also decrease the cost and time for repair and replacements, as they will have greater resistance to impact and handling damages. All of these will decrease the recurring costs; enhance the working envelope of the vehicle and thereby allowing movement in all environments and rapid turnaround between flights [23]. All these attributes are strongly interdependent, often directly conflicting, and require compromises in the design process to reach an acceptable solution. Finally, the approach should lead to the optimal combination of these features, such that a robust, operable and weight-efficient TPS can be developed.

Approaches

Extreme thermal environments can be dealt in various ways during hypersonic flight. As more air-breathing hypersonic vehicles are being developed, newer and efficient ways to restricting these extreme temperatures need to be developed to meet the severe thermal structural changes. These techniques include both TPS and hot structures and these concepts can be commonly categorized as: passive, semi-passive, and actively cooled approaches [24].

Passive: They can be further divided into three approaches: An *insulated* structure is used to resist mild heat flux, subjected to smaller time periods. Figure 1-2

[24] shows the insulated structure for the Space Shuttle Orbiter elevons. Thermal radiation is generally the mechanism to remove heat. It absorbs most of the heat through insulation, thereby maintaining the structure beneath with an acceptable temperature range.

The *heat sink structure* can be used for a transient situation where the heat flux is mild. When the heating of the surface occurs, most of the heat is absorbed by the structure and the remaining is radiated to the ambient. The structure capacity to absorb heat depends on its mass, specific heat capacity, maximum acceptable temperature increase and the initial temperature of the structure material. The example shown in Figure 1-3 [24] is of the leading edges of X-15 which uses a heat sink structure.

A *hot structure* also works under mild heat fluxes. The structure reaches a steady state condition when greater heat loads are applied for longer time duration. In this the temperature of the whole structure raises to a higher temperature. Some of the heat is radiated away by the top surface and the remaining heat is conducted inside. It also has the capability to provide a more robust exterior surface. Because of these attributes, it is being considered for control surfaces and wings of RLV's (Figure 1-4) [24].

Semi-Passive: A semi-passive technique like a *heat pipe* can be used where large heat flux persists for long time. The heat is carried away by a working fluid to an alternative region where the heat is radiated out. Heat-pipe-cooled wing leading edges are one of the examples [25] (Figure 1-5). Another semi-passive technique for managing extreme temperature is *Ablators* [26]. It is used for regions where the heat flux is very large and persists for very short time. It obstructs the heat by ablation and in this process, the ablator material chars out. It can be used only once (Figure 1-6) [24].

Active: Active cooling is used where heat fluxes are very large and remain for a lengthier duration of time. *Convective cooling* is one type of active cooling. The Space Shuttle main engine (SSME) is one of the examples of convective cooling (Figure 1-7) [24]. The Space Shuttle propulsion system uses a convecting cooling process. The coolant takes up the heat and carries it away. Though the structure remains hot, the temperature is within the acceptable range maintained by the active cooling (Figure 1-8) [36].

Other types of active cooling are *Film cooling* and *Transpiration cooling*. Both of them work for larger heat fluxes and longer duration of time. In film cooling, at a specific place, the coolant is infused into a flow at an upstream location. It functions as a thin, cool insulating layer (Figure 1-9) [24]. However, in transpiration cooling, coolant is infused constantly at larger areas, through a porous structure into the hot gas flow in order to lessen the heat flux in the structure. Cooled carbon/carbon (C/C) combustion chamber as shown in Figure 1-10 [24] is an example of transpiration cooling.

Background on Past TPS

The initial missions of NASA such as Gemini, Apollo, and Mars Viking used ablative TPS that were conformed for the limited entry environment [27]. An all-ablative system TPS was used for the Apollo mission. It used molded solid tiles of Avcoat 5026-22, fused to stainless steel honeycomb sandwich [5]. In order to further reduce the density, newer types of ablator were inspected. One of them was an Avcoat 5026-39 which had a weight of 37-lb/ft^3 and was much lighter as compared to the previous materials. The Avcoat 5026-39 is put into an open honeycomb of phenolic glass, which is then bonded to the steel. Though this ablative material was very promising, after Mars Viking NASA, the concept of using an ablative TPS entirely started to die out and NASA

started moving the research towards reusable TPS in support of Space Shuttle. The TPS is spread over approximately the whole orbiter surface, and it composes of eight different materials in various places; based on the amount of heat shield it requires [29].

- Reinforced carbon-carbon (RCC) [29]: For re-entry temperatures greater than 2,300 ^{o}F, RCC is used. In the Space Shuttle orbiter, it is used in the nose cap and wing leading edges.

- High Temperature Reusable Surface Insulation Tiles (HRSI) [29]: The HRSI tiles are used where the temperature is below 2,300 ^{o}F. It consists of high-purity silica 99.8-percent amorphous fiber insulation and they are held together using ceramic bonding. They are generally low-density material and the ranges of thickness are between 1 and 5 inches. It is used in upper forward fuselage, forward fuselage windows, complete lower side of the orbiter, some part of the orbital maneuvering system and reaction control system pods, the leading and trailing edges of the vertical stabilizer; wing glove areas; elevon trailing edges; and the upper body flap surface [29].

- Fibrous Refractory Composite Insulation Tiles (FRCI) [29]: In order to replace the HRSI tiles, FRCI tiles were developed. The tiles were coated black in order to lessen the coating's sensitivity towards cracking while they are handled and used. The FRCI tiles were 10 percent less dense as compared to the HRSI tiles and had better strength and durability as well [29].

- Low-temperature Reusable Surface Insulation Tiles (LRSI) [29]: The LRSI tiles are used where the temperature is less than 1,200 ^{o}F. They are approximately 8 inches square in size and are coated with a moisture resistant materials on the top and the sides [29].

- Advanced Flexible Reusable Surface Insulation Tiles (AFRSI) [29]: In order to replace the LRSI tiles, AFRSI tiles were developed. The composite fabric insulation and the white fabric are stitched together to form a quilted layer. They are generally low-density material (8–9 pounds per cubic foot) and the ranges of thickness are between 0.45 and 0.95 inches [29].

- Felt Reusable Surface Insulation Tiles (FRSI) [29]: For areas where temperature is less than 700 ^{o}F, FRSI tiles are used. It is used on the upper payload bay doors, some sections of the mid fuselage, upper wind surface, and OMS/RCS pods [29]. They are approximately 3–4 feet square in size and the thicknesses ranges from 0.16 to 0.4 inches. FRSI uses Nomex felt reusable surface insulation.

- Durable Advanced Reusable Surface Insulation (DURAFRSI) [29]: DURAFRSI contains high purity silica fibers bonded by woven ceramic yarns. It is very much like the AFRSI, primarily the more advanced AFRSI.

This reusable surface insulation (RSI) arrangement is installed in various processes [30] (Figure 1-11). In order to guard the aluminum skin and to help it to bond with the adhesive room-temperature vulcanizing rubber (RTV), a primer (Koropon) is put on to the shuttle aluminum skin. The RTV is then bonded to the strain isolation pad (SIP) to sustain the mechanical loads. Another layer of RTV bonds is superimposed on to the SIP. Nearly 24,000 different types of tiles are installed on to the space shuttle orbiter. To account for the increase in size due to thermal expansion, gaps are provided in between these tiles.

However, these ceramic-based tiles were brittle in nature and required considerable repair between flights [19]. Further, the coefficient of thermal expansion for the aluminum and tiles varies considerably; hence the TPS cannot be installed directly on to the aluminum skin as it could lead to cracking of the tiles. Next came the X-33 RLV recommended by Lockheed Martin, which was expected to be a half-scale single-stage-to-orbit (SSTO) RLV. For the first time, it would use a metallic TPS [9, 31] on the windward surface. The metallic system was selected because it was found to be more robust, greater protection from moisture, and lesser life-cycle costs as compared to the ceramic tile designs. The reusable metallic TPS had low mass, required fewer repairs and had greater strength to bear mechanical and thermal loads than the ceramic tiles. On X-33, two kinds of metallic systems were tried, i.e. PM-1000 [32,33] and Inconel 617 [34].

Figure 1-12 [31] shows the schematic of the TPS architecture on to the windward area of the X-33. Every TPS panel comprises of two metallic face sheets, i.e. inner and outer sheets with a metallic honeycomb core in between. Underneath the inner face

sheet is an insulating layer packed inside in an Inconel foilbag that is connected to the rear end of the honeycomb panels. The insulation layer should be able to maintain the underlying structure within 450 ^{o}K. The TPS panels are connected to the beneath structure through a standoff at every joint. Creep and strength properties at extreme temperatures were the main criteria to select the honeycomb materials.

These stand-off TPS concepts can be employed on a cold or warm structure. The stand-off TPS has an advantage that it develops the required “aeroshell” by connecting the TPS panels to the stand-off brackets (Figure 1-13) [24]. The biggest confrontation with this concept is to shift the aero loads. Transferring of thermal loads is not a problem, as the standoff overlaps and seals within the panels, checking the gas penetration to protect the structure underneath. They are approximately 18 inch square in size and can bear temperatures up to 1,800°F, based on the type of metallic alloy considered [24]. However, for these hypersonic vehicles there is always a need for greater temperature resistance TPS. So a ceramic matrix composite (CMC) standoff TPS [24] was also explored (Figure 1-14). The outer CMC panel makes the “aeroshell” in addition to the oxidation protection whereas the stand-off TPS takes in the inner insulation. The high temperature seals and a connector are utilized to secure the inner structure and the exterior CMC panel together. Again the biggest confrontation is its ability to withstand the aero and pressure loads and not the thermal loads. Further, it should also be able to bear acoustic and vibration loads.

Following these advancements, additional enhancements were made resulting in the ARMOR TPS [23, 37]. In order to overcome some of the limitations of the previous metallic TPS approaches (e.g., Multiwall, X-33), the ARMOR TPS (Figure 1-15) was

developed. The design of ARMOR TPS is such that it minimizes the thermal radiation in the space within the panels, supports joint and edge sealing on the cooler internal surface of the panels, and lessens the effect of thermal expansion on the internal and external face sheet independent of each other. It had conformable surface so that any conflict in the thermal expansion between the honeycomb and the frames can be accommodated. Further, the standoff system used in the ARMOR TPS used for joining the TPS panels to the stiffened structures was found to be of very less weight. The ARMOR TPS standoff system is illustrated in Figure 1-16 [36] with the primary structure being a cryogenic tank that needs to be protected from the extreme aerodynamic heating.

At present, a range of advanced TPS concepts are also being examined at NASA. One of them is Tailorable Advanced Blanket Insulation (TABI) [39]. It was an enhancement over the present AFRSI used on the shuttle orbiter and was manufactured at NASA Ames Research Center. Intrinsically woven corrugations have greater strength and can survive temperatures up to 2,200 ^{o}F, better than the current AFRSI. Windward sides of the reentry space vehicle are one of the most critical areas and it is expected that TABI can be utilized there [39] (Figure 1-17). The TABI constitutes of an external ceramic fabric with C-9 coating, 6 lb/ft^3 Q-fiber felt insulation, ceramic fabric corrugations, and a fabric internal layer. Room temperature vulcanizing (RTV) adhesive are used to bond the TABI to the structure.

One of the very new TPS is the quilted blanket TPS, called the Conformal Reusable Insulation (CRI) [39] (Figure 1-18), is made by Boeing Huntington Beach to further enhance the performance as compared to the current TPS used on the Space

Shuttle orbiter. Based on the matrix composition used on the CRI, the temperature limit can vary from 1,800°F-2000°F. The CRI is manufactured using a unique method by putting the ceramic batting material in between the ceramic fiber face sheets and this "rigidization" approach significantly improves the fabrication of CRI, with perfectly flat blankets and excellent dimensional precision.

The latest spacecraft thermal protection systems are the Boeing Rigid Insulation (BRI) and Alumina Enhanced Thermal Barrier (AETB) ceramic tile with Toughened Uni-Piece Fibrous Insulation (TUFI) coating [40], which have a very high operational temperature. AETB was manufactured at the Ames Research Center and it has excellent strength and durability. It can protect areas where temperatures are as high as 2,500 ^{o}F. The AETB ceramic tiles are approximately 8 inches square in size and are coated with TUFI. Strain isolation pads (SIPs) are used between the AETB tiles and the substructure to compensate for the thermal expansion mismatch between the two.

Integral Thermal Protection System

With the recent emphasis on commercial RLV's, reducing TPS cost has become an increasingly important consideration. The costs for development, fabrication, installation, fuel required to carry it and maintenance all contribute to the total life-cycle cost. Reduced life cycle costs imply design drivers such as robustness and operability to lower maintenance costs. A robust TPS is not easily damaged by its design environment and may be able to tolerate some damage without requiring immediate repair. An operable TPS should be easily inspected, removed and replaced, maintained, and repaired if necessary. Low maintenance is especially important for RLV's for which rapid turnaround is critical to economic viability.

In particular, weight of the TPS is one of the most important design criteria, as TPS occupies huge area on the vehicle surface and thus a huge factor for cost. Low mass is important for TPS, carried by a high speed vehicle which must be accelerated and/or decelerated through large changes in velocity. The energy to accelerate additional TPS mass requires additional fuel, and a larger vehicle to contain that fuel, or a reduction in payload mass. Consequently, TPS designs are primarily performance driven, that is, designed for minimum mass to perform the thermal function. The substructure beneath the TPS bears all the mechanical loads. Further, due to the brittle nature and low strength of tiles, ceramic tile TPS must be isolated from the mechanical strains of the underlying sub structure. This is accomplished by the felt strain isolation pad (SIP). Thus, the TPS was used as an add-on to the structure of the hypersonic vehicle. Further, the tiles have been susceptible to impact damage, and have required waterproofing after each flight. Inspections, repairs, and waterproofing are time-consuming and costly.

These add-on concepts had many other problems. One of them is the incompatibility of the load bearing structure and the TPS, thereby compromising the strength of the surface of the space vehicle. The tiles may not bond really well with the structure, which could result in slackening and separation of tiles from the structure and thereby causing catastrophic failure of the space vehicle. The newer TPS approaches like the BRI and AETB also overcome some of the limitations of the add-on TPS concept. One of the potential ways of saving weight is to combine the load bearing function and the TPS function into one single structure, known as Integral Thermal Protection System (ITPS). One such concept for ITPS uses a corrugated-core sandwich

structure. An ITPS is a sandwich panel composed of two thin faces separated by a corrugated core structure which can be of homogeneous materials such as metals or orthotropic materials such as composite laminates. The two thin faces are the top face sheet (TFS) and the bottom face sheet (BFS) with a corrugated web in between (Figure 1-19). The sandwich panel is composed of several unit cells placed adjacent to each other. The empty space in the corrugated core will be filled with a non load-bearing insulation such as Safill®. It combines the three passive TPS concepts of hot structure, insulated structure and heat sink. The outer and inner walls of ITPS carry the airframe loads, with the outer wall operating hot and the inner wall insulated. It is thermally integrated, has a higher structural efficiency, and is potentially lower maintenance. The outer surface is a robust, high-temperature material. The wall thickness helps provide stiffness and the large integrated structure eliminates/reduces surface gaps and steps.

Sandwich structures generally have good damage tolerance properties and can withstand small object impact. Sandwich structures can largely categorized into foam core sandwich and truss core sandwich (Figure 1-20).The insulating structural foam core of the sandwich panel has high temperature capability and low conductivity. Composite sandwich panels used in these applications offer significant weight savings leading to increased payload and greater range of travel, reduced electromagnetic and acoustic signatures, better corrosion resistance, and lower maintenance cost when compared to traditional metallic panels [41]. The truss core sandwich panels have discrete connections between the hot and cool face sheets. It has good load bearing capability along with the insulation. It has an acceptable structural connections and acceptable heat shorts. Corrugated core sandwich panel (Figure 1-19) is considered in

the present study. Other truss core sandwich panels are also being investigated by other research groups. The core geometries analyzed were truss-cores with tetragonal, pyramidal, and kagome configurations [42, 43, 44] and prismatic cores with corrugated and diamond (or textile) configurations [45, 46, 47]. In all of these panels bending, transverse shear and crushing loads were considered for analysis. However, the heights of these sandwich panels were approximately 20 to 30 mm which were very small as compared to the ITPS panels (70–90 mm) because TPS dictates that the height be as large as possible to increase the heat conduction path.

The biggest challenge of an ITPS is that the requirements of a load-bearing member and a TPS are contradictory to one another. A TPS is required to have low conductivity and high service temperatures. Materials satisfying these conditions are ceramic materials, which are also plagued by poor structural properties like low impact resistance, low tensile strength and low fracture toughness. On the other hand, a robust load-bearing structure needs to have high tensile strength and fracture toughness and good impact resistance. Materials that satisfy these requirements are metals and metallic alloys, which have relatively high conductivity and low service temperatures. The challenge is to combine these functions into one structure satisfying all the required constraints.

The top face sheet is a hot structure and ceramic composites such as SiC/SiC composites and titanium alloys (Ti-6Al-4V) are candidate materials. The web could also be made of similar composite. From weight efficiency point of view the bottom face sheet is expected to be a heat sink for the ITPS; therefore a material that has a high heat capacity is needed for the bottom face sheet. The bottom face sheet will also

experience a major portion of the in-plane stresses because of the attachment mechanisms of stringers and frames to the space vehicle. Therefore, a high Young's Modulus material with a high heat capacity is suitable for the bottom face sheet. Thus there are several design variables - geometric and material property variables. The design of such a TPS will require several thousand analyses to obtain a minimum mass design. When the uncertainties in properties, dimensions and loads are taken into account, the computational costs will be prohibitively high. Hence, there is a need to develop efficient methods for analysis and design of ITPS for future space vehicles.

Dissertation Organization or Outline

The objectives of this research are:

- Develop a finite element analysis based homogenization method to model the composite ITPS as a homogeneous orthotropic plate.
- Perform simulations on the 2D plate model to obtain responses such as stresses and displacements as a function of the design variables to create 2D response surfaces (2D-RS).
- Develop a simplified buckling analysis and compare it with the 3D buckling analysis to create a 2D response surfaces.
- Develop correction response surface using algebraic surrogates (CRS).
- Develop a multi-fidelity analysis to compute the response variables to optimize the design.

The chapters are organized as follows. In Chapter 2, a finite element (FE) based micromechanical analysis procedure is developed for modeling corrugated sandwich panels as 2D orthotropic plates. The equivalent stiffness parameters such as the extensional, bending, coupling and shear stiffnesses of the ITPS are obtained. These parameters are input into 2D FE plate model. In Chapter 3, a FE based homogenization and reverse homogenization procedure is described. The equivalent plate responses

such as the stresses and displacements are obtained, when subjected to thermal and pressure loads. The plate responses are also compared with the corresponding 3D analysis. In Chapter 4, the key design drivers of the ITPS are identified. The ITPS is optimized for a minimum mass design while satisfying all of the constraints. The constraints are generated using a response surface. Different types of response surfaces are explored and based on the error of the fit; the best response surface is used. Finally, in Chapter 5, an overview of this dissertation research and findings are presented.

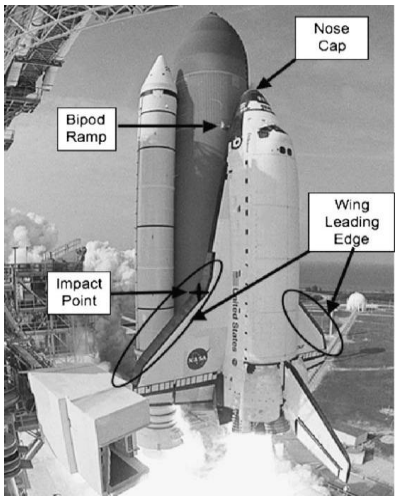

Figure 1-1. Space Shuttle photograph showing release point of 1.7-lb foam at the bipod ramp and the impact point on the left wing leading edge (Lyle, K.H., & Fasanella, E.L., "Permanent set of the Space Shuttle Thermal Protection System Reinforced Carbon–Carbon material",Journal of Composites, Part A 40 (2009) 702–708).

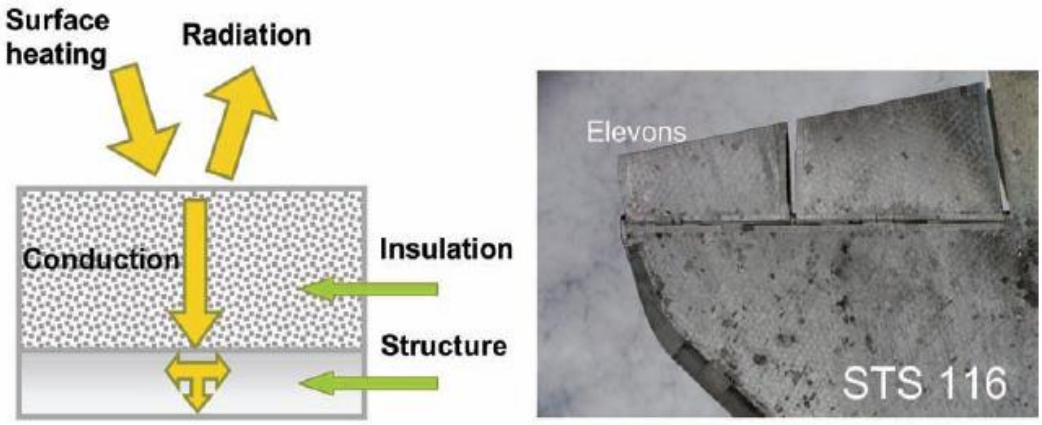

Figure 1-2. Schematic and photograph (Space Shuttle Orbiter elevons) of an insulated structure (Glass, D.E.,"Ceramic Matrix Composite (CMC) Thermal Protection Systems (TPS) and Hot Structures for Hypersonic Vehicles", 15th Space plane and Hypersonic Systems and Technologies Conference, AIAA 2008–2682).

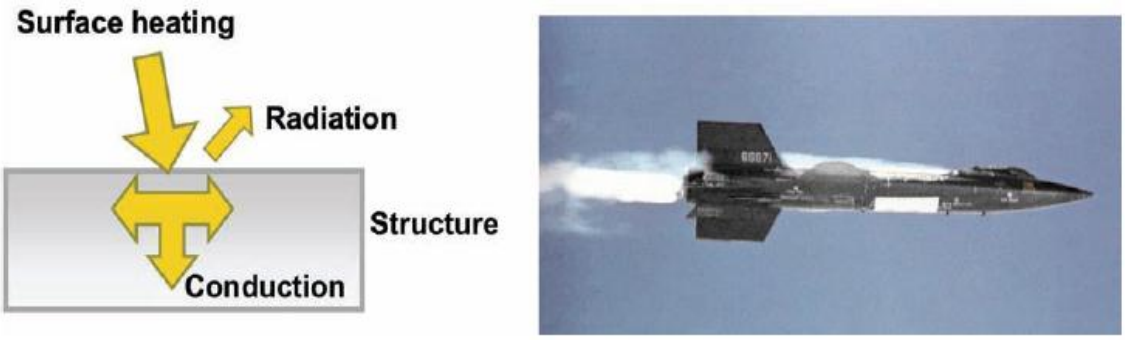

Figure 1-3. Schematic and photograph (X-15) of a heat sink structure (Glass, D.E.,"Ceramic Matrix Composite (CMC) Thermal Protection Systems (TPS) and Hot Structures for Hypersonic Vehicles", 15th Space plane and Hypersonic Systems and Technologies Conference, AIAA 2008–2682).

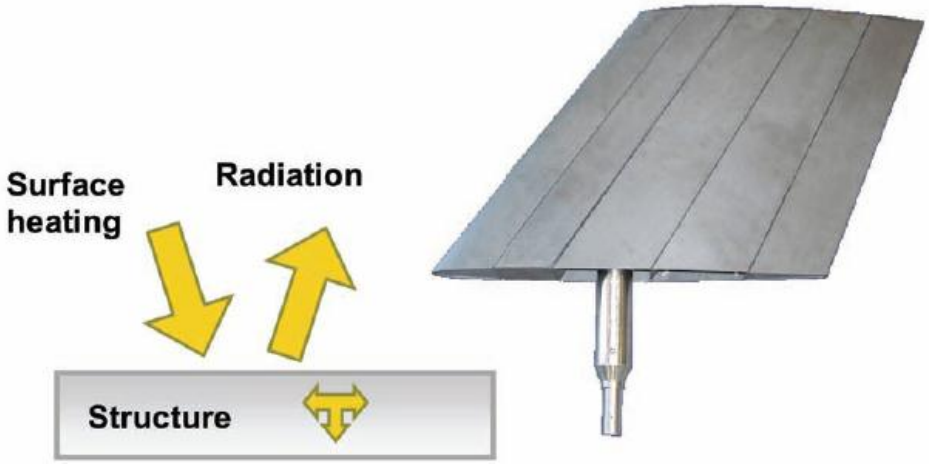

Figure 1-4. Schematic and photograph of a hot structure (Glass, D.E.,"Ceramic Matrix Composite (CMC) Thermal Protection Systems (TPS) and Hot Structures for Hypersonic Vehicles", 15th Space plane and Hypersonic Systems and Technologies Conference, AIAA 2008–2682).

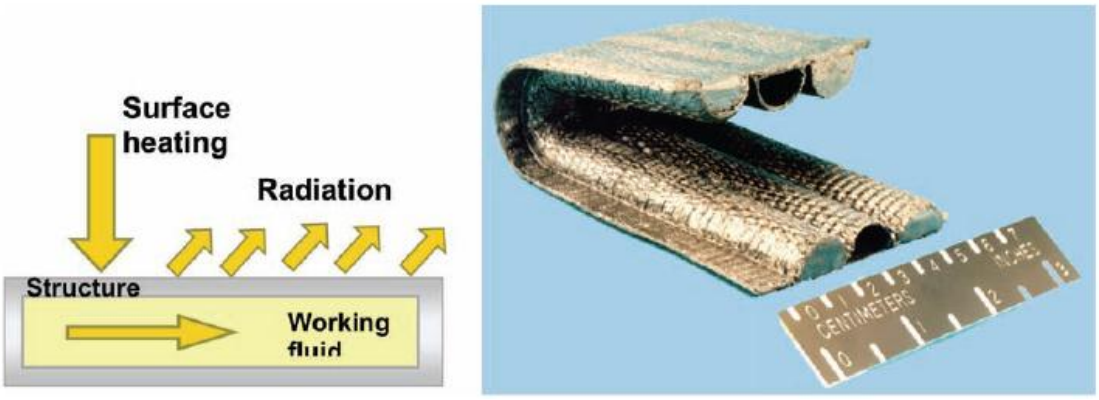

Figure 1-5. Schematic and photograph of a heat-pipe-cooled leading edge (Glass, D.E.,"Ceramic Matrix Composite (CMC) Thermal Protection Systems (TPS) and Hot Structures for Hypersonic Vehicles", 15th Space plane and Hypersonic Systems and Technologies Conference, AIAA 2008–2682).

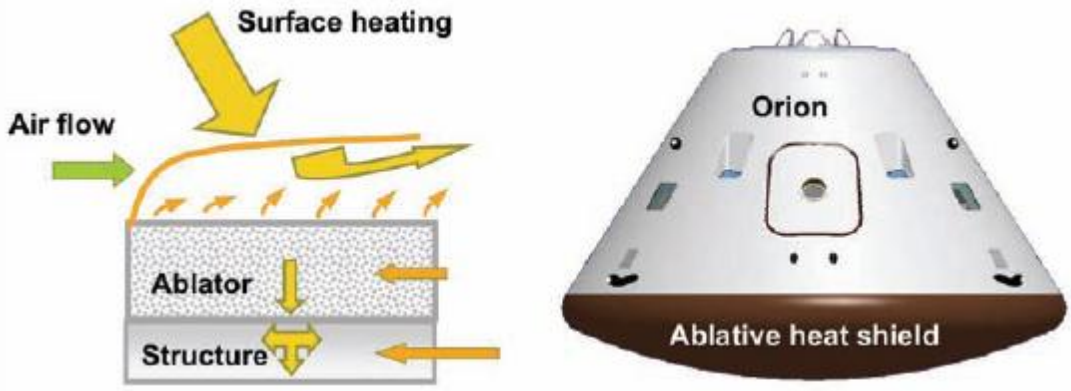

Figure 1-6. Schematic and photograph of an ablative heat shield (Glass, D.E.,"Ceramic Matrix Composite (CMC) Thermal Protection Systems (TPS) and Hot Structures for Hypersonic Vehicles", 15th Space plane and Hypersonic Systems and Technologies Conference, AIAA 2008–2682).

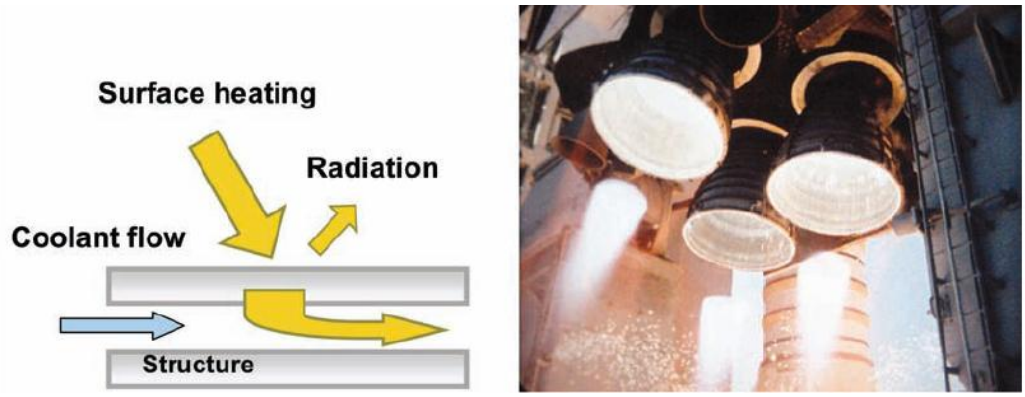

Figure 1-7. Schematic and photograph of actively convective cooling structure (Glass, D.E.,"Ceramic Matrix Composite (CMC) Thermal Protection Systems (TPS) and Hot Structures for Hypersonic Vehicles", 15th Space plane and Hypersonic Systems and Technologies Conference, AIAA 2008–2682).

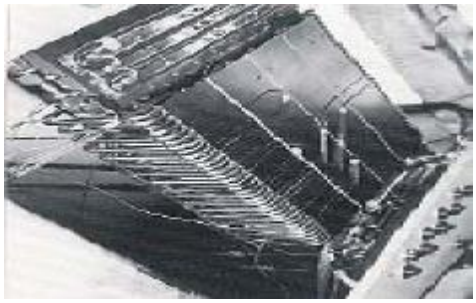

Figure 1-8. NASP actively convective cooling panel (Blosser, M., "Thermal Protection Systems for Reusable Launch Vehicles", Short Course: Thermal Control Hardware, Thermal & Fluids Analysis Workshop, Hampton, VA, August 22, 2003).

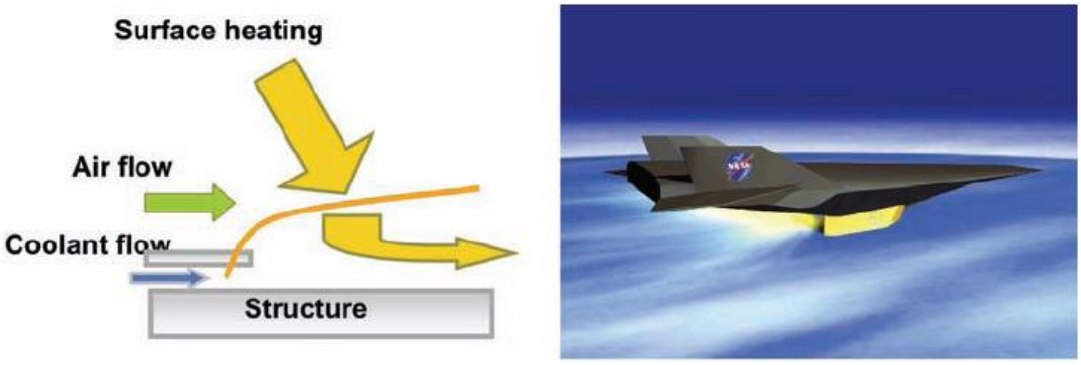

Figure 1-9. Schematic of film cooling and drawing of a hypersonic vehicle (Glass, D.E.,"Ceramic Matrix Composite (CMC) Thermal Protection Systems (TPS) and Hot Structures for Hypersonic Vehicles", 15th Space plane and Hypersonic Systems and Technologies Conference, AIAA 2008–2682).

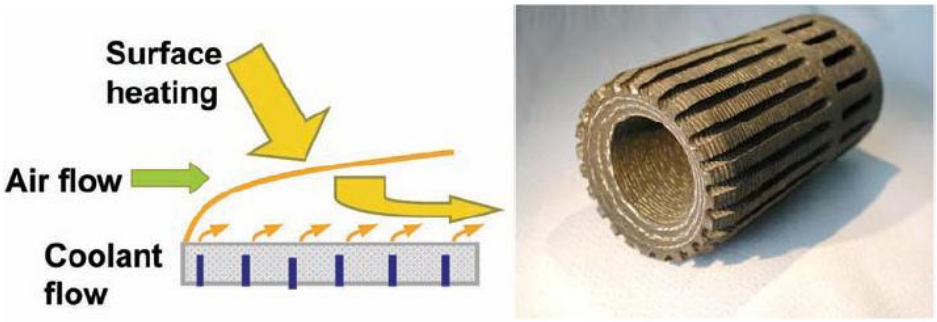

Figure 1-10. Schematic of transpiration cooling and a C/C cooled combustion chamber test article (Glass, D.E.,"Ceramic Matrix Composite (CMC) Thermal Protection Systems (TPS) and Hot Structures for Hypersonic Vehicles", 15th Space plane and Hypersonic Systems and Technologies Conference, AIAA 2008–2682).

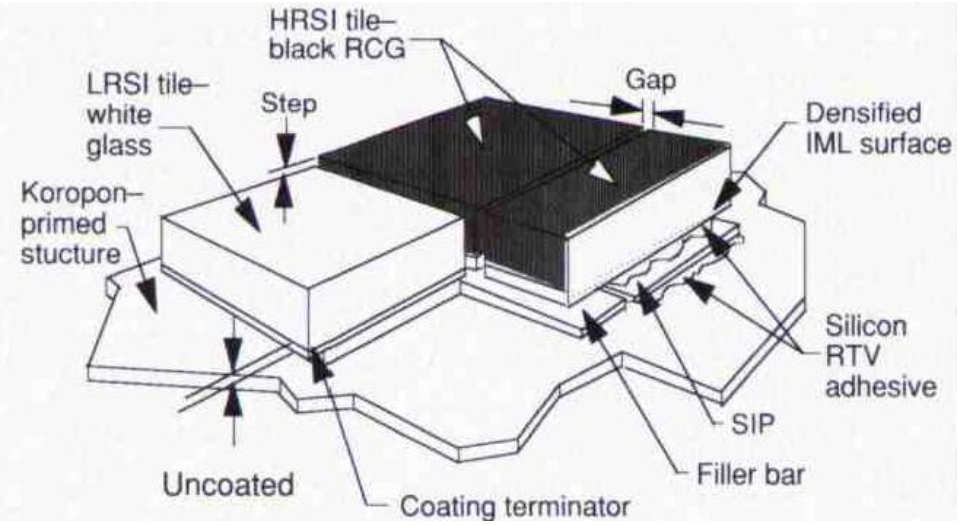

Figure 1-11. Schematic of RSI Installation (Leiser, Daniel B., "Shuttle Thermal Protection System", American Ceramic Society Bulletin; Aug2004, Vol. 83 Issue 8, p44–47).

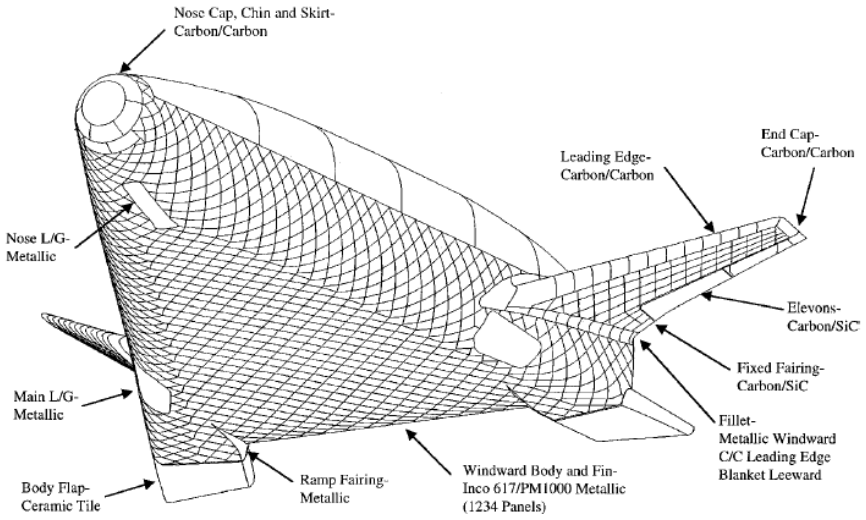

Figure 1-12. X-33 windward surface configuration (Surface Heating Effects of X-33 Vehicle Thermal-Protection-System Panel Bowing, Palmer, G., and Sherman, B., Journal of Spacecraft and Rockets, Vol. 36, No. 6, November–December 1999).

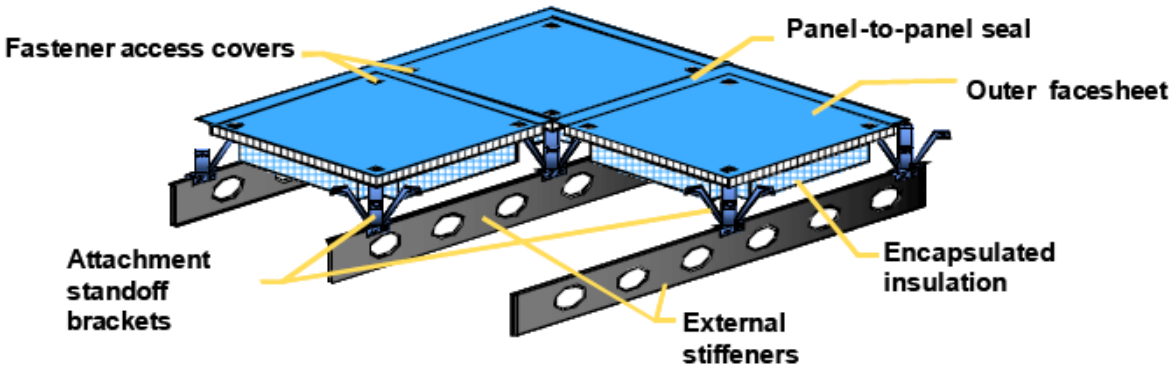

Figure 1-13. Metallic TPS concept for windward surface of X-33 (Glass, D.E.,"Ceramic Matrix Composite (CMC) Thermal Protection Systems (TPS) and Hot Structures for Hypersonic Vehicles", 15th Space plane and Hypersonic Systems and Technologies Conference, AIAA 2008–2682).

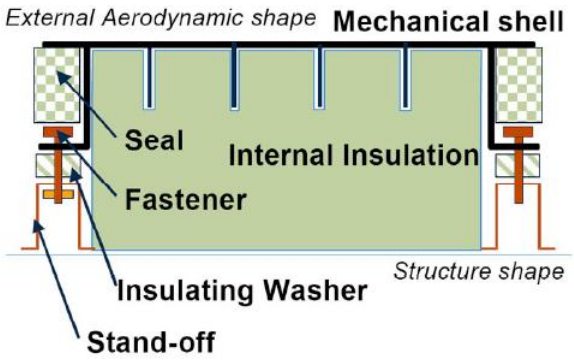

Figure 1-14. Schematic drawing of the CMC TPS (Glass, D.E.,"Ceramic Matrix Composite (CMC) Thermal Protection Systems (TPS) and Hot Structures for Hypersonic Vehicles", 15th Space plane and Hypersonic Systems and Technologies Conference, AIAA 2008–2682).

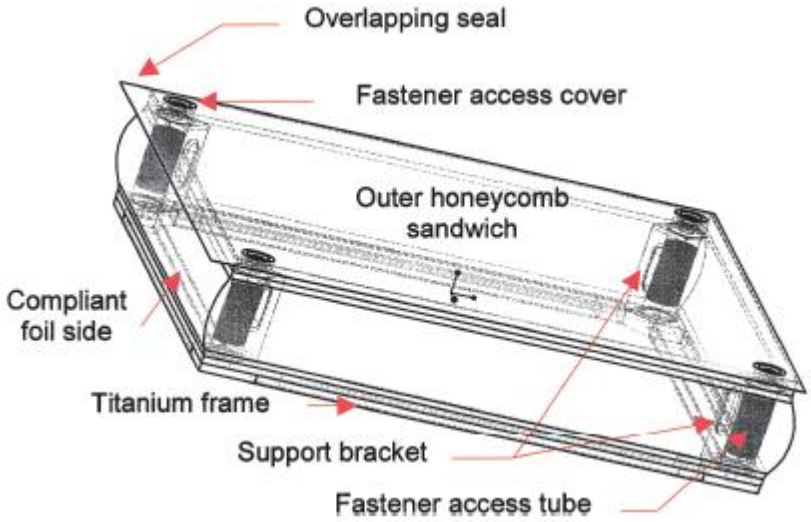

Figure 1-15. ARMOR TPS Panel (Blosser, M. L., "Fundamental Modeling and Thermal Performance Issues for Metallic Thermal Protection System Concept," *Journal of Spacecraft and Rockets*, Vol. 41, No. 2, Mar–Apr 2004, pp. 195–206).

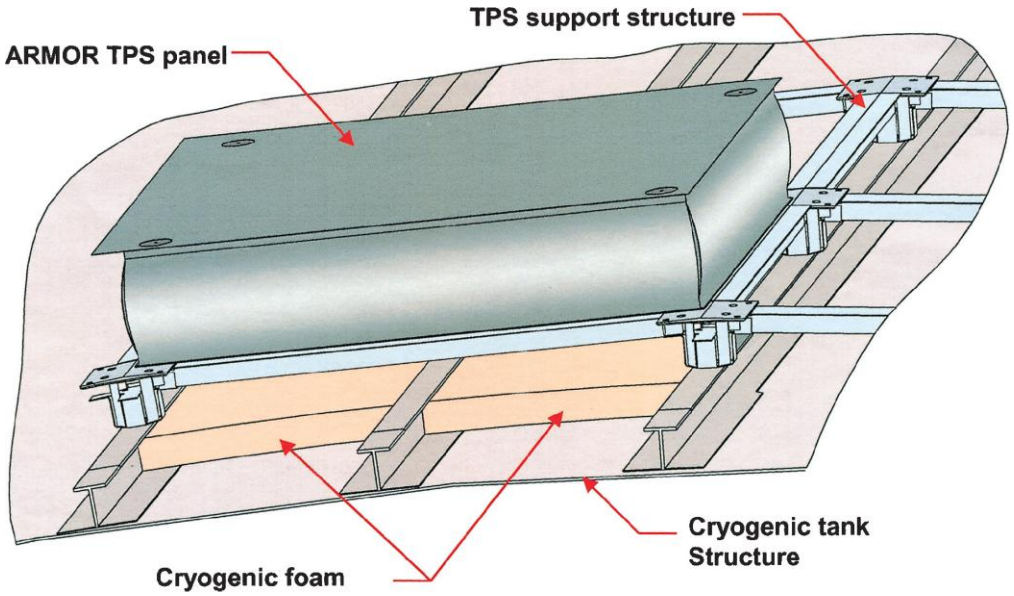

Figure 1-16. ARMOR TPS integrated with Cryogenic Tank (Blosser, M., "Thermal Protection Systems for Reusable Launch Vehicles", Short Course: Thermal Control Hardware, Thermal & Fluids Analysis Workshop, Hampton, VA, August 22, 2003).

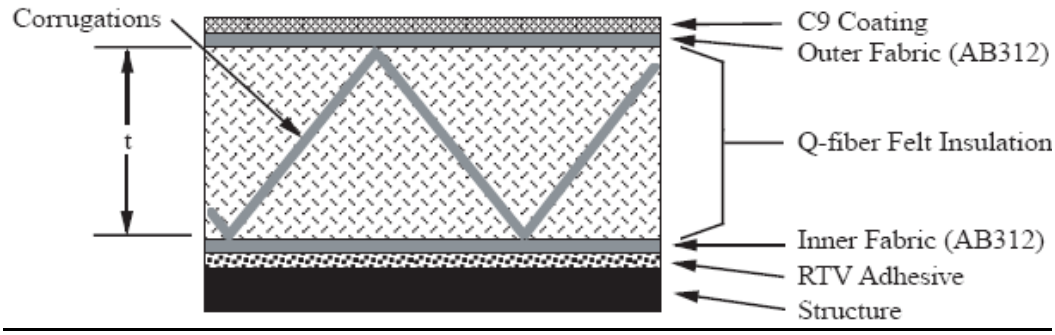

Figure 1-17. TABI Thermal Protection System (Chiu, S.A., and Pitts, W.C.,"Reusable Surface Insulation for Reentry Spacecraft", AIAA Paper 91–0695, 29th Aerospace Sciences Meeting, Jan. 1991).

Figure 1-18. CRI-blanket with rigidized outer surface (Blosser, M., "Thermal Protection Systems for Reusable Launch Vehicles", Short Course: Thermal Control Hardware, Thermal & Fluids Analysis Workshop, Hampton, VA, August 22, 2003).

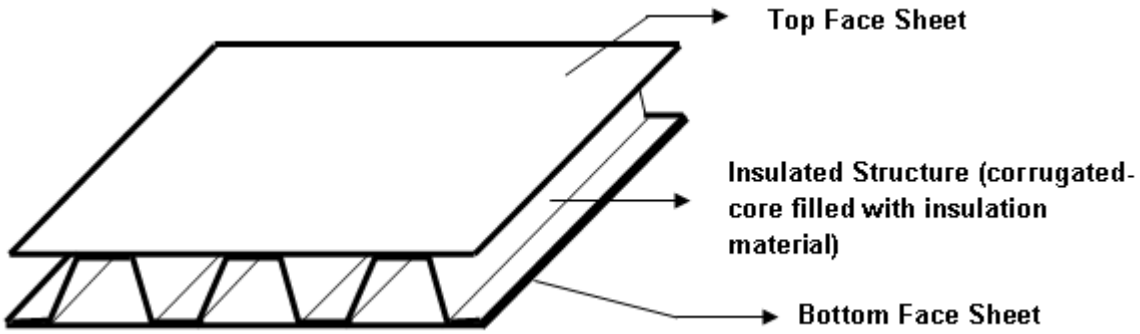

Figure 1-19. A corrugated-core sandwich structure concept for Integrated Thermal Protection System (ITPS).

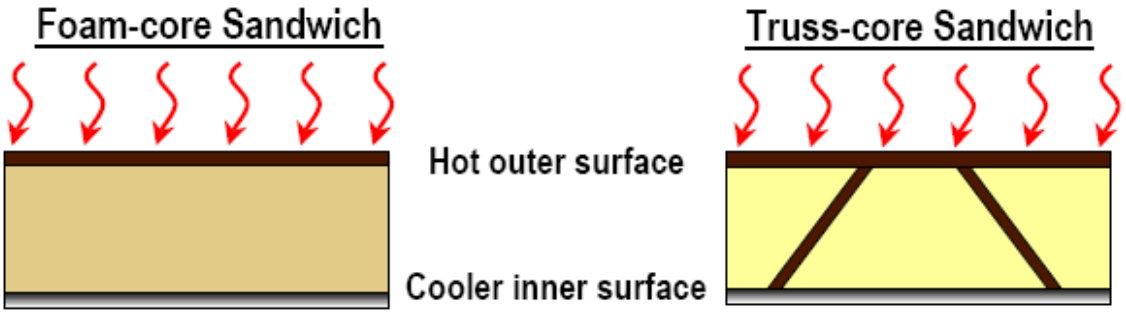

Figure 1-20. Schematic diagram of two sandwich panels (Blosser, M., "Thermal Protection Systems for Reusable Launch Vehicles", Short Course: Thermal Control Hardware, Thermal & Fluids Analysis Workshop, Hampton, VA, August 22, 2003).

CHAPTER 2
FINITE ELEMENT BASED MICROMECHANICS MODELS OF THE INTEGRATED THERMAL PROTECTION SYSTEM

Corrugated Core Sandwich Structure

A sandwich structure is most commonly made up of two thin stiff faces separated by a very lightweight core material. By selecting appropriate dimensions and materials for the face sheets and core, outstanding stiffness and strength at low weight of the sandwich panel are achieved [48, 49]. Regardless of the core design, it should be stiff and strong in directions out-of-plane in order to keep the faces separated and parallel under in-plane and transverse normal loadings. Since the face sheets are thin, most of the out-of-plane shear load is carried by the core, and it therefore should be stiff and strong in shear. In addition it should be able to take some bending and twisting as well [50].

Analytical and micromechanical analyses have been performed on corrugated sandwich panels since as early as 1940. Corrugated core sandwich panels were homogenized as a thick plate and equivalent stiffnesses were determined using force distortion relationship [51, 52]. Elastic stiffnesses of the z-core and c-core sandwich panels were also analyzed using the same homogenization methods [55, 56]. Lok and Cheng [57, 58] also derived the transverse shear stiffness properties from the unit cell approach. They also validated its stiffness properties by deriving the close form solution for maximum deflection, when the panel is subjected to uniform lateral load and compared it with 3D finite element method. Carlson et al [59] using the first order shear deformation laminated plate theory approach derived the various stiffnesses of corrugated core sandwich panels They found that in-plane extensional and shear stiffnesses, and bending and twisting stiffnesses are dominated by the extensional and

shear stiffnesses of the face sheets and their predictions agreed favorably with measured data. The measured transverse shear stiffnesses, however, were substantially less than the numerically predicted values, especially perpendicular to the corrugations. Cheng et al [50] reviewed and derived analytically the elastic stiffness of a corrugated core sandwich panel using the Mindlin-Reissner plate theory. The stiffness properties derived is verified by applying uniform pressure load and found that the higher ratio of the core depth to web thickness results to more deflection and more susceptible to buckling. In [62], Nordstrand et al, a theoretical study on how various core shapes influence the effective transverse shear moduli is presented. An upper limit of the transverse shear modulus across the corrugations is calculated assuming rigid facings. The reduction of the effective shear modulus across the corrugation due to deformations of the facings is quantified and the results are compared with classical plate theory and finite elements. Also, sandwich panels were designed using analytical equations to carry prescribed combinations of moment and transverse force when a realistic minimum crushing strength is imposed. These formulas were used for imposing the constraints in the optimization problem to obtain a panel with minimum weight [53, 54].

Another application where the corrugated core is used is cardboards (Figure 2-1). It is a combination of paperboards, usually two flat liners and one inner fluted corrugated medium. It is often used for making corrugated boxes for shipping or storing products. The various tools and analytical methods that have been developed could also be applied for ITPS structures.

Biancolini [60] derived the equivalent stiffness properties of corrugated boards by performing static condensation of the stiffness matrix obtained using the finite element model of the full panel. Buannic et al. [61] used asymptotic expansion based analytical method for deriving the equivalent properties of corrugated panel. Talbi, Batti et al [63], has developed the equivalent stiffness of the analytical homogenization model for corrugated cardboard and numerically implemented using a 3-node shell element. They also compared the results with 3D model under different types of loading like tension, compression, bending, transverse shear, in plane shear and torsion. In Isakasson et al [64], the corrugated board panel is divided into an arbitrary number of thin virtual layers. For each virtual layer, a unique effective elastic modulus is calculated. Then, the elastic properties in all layers are assembled together in order to analyze a corrugated board as a continuous structure having equivalent mechanical properties to a real structure. It uses the strain energy approach to calculate the effective modulus for a corrugated core. Also assuming that the transverse shear strain will vary through the plate thickness, they developed an analytical expression for shear correction factors using the energy approach. The capability of the model to properly capture and simulate the mechanical behavior of corrugated boards subjected to plate bending as well as three-point-bending has been demonstrated and are also compared to experiments on corrugated board panels of varying geometry. Martinez et al [65, 66] uses a strain energy approach and a transformation deformation matrix to determine analytically the equivalent stiffness matrix of the sandwich panel.

Geometric Variables and Material Properties

The geometry of the ITPS structure with corrugated-core design is shown in Figure 2-2. This geometry can be completely described using the following 6 geometric variables:

- Thickness of top face sheet (TFS), $t_{TF.}$
- Thickness of webs, t_W.
- Thickness of bottom face sheet (BFS), t_{BF}.
- Angle of corrugations, θ.
- Height of the sandwich panel (center-to-center distance between top and bottom face sheets), d.
- Length of a unit-cell of the panel, $2p$.

Unit Cell Analysis

Micromechanical finite element analysis of a unit cell was performed to determine the extensional, bending, coupling and transverse shear stiffness of the equivalent orthotropic plate. This would require the prediction of the effective (macroscopic) properties of the panel from its constituent (microscopic) components-the top face sheet, bottom face sheets and the webs. The relationship between the unit cell macro stresses and macro strains provided the constitutive relations for the material. Thus, the in-plane extensional and shear response and out-of-plane (transverse) shear response of an orthotropic panel are governed by the following constitutive relation:

$$\begin{bmatrix} N_x \\ N_y \\ Q_y \\ Q_x \\ N_{xy} \\ M_x \\ M_y \\ M_{xy} \end{bmatrix} = \begin{bmatrix} A_{11} & A_{12} & 0 & 0 & 0 & B_{11} & B_{12} & 0 \\ A_{12} & A_{22} & 0 & 0 & 0 & B_{12} & B_{22} & 0 \\ 0 & 0 & A_{44} & 0 & 0 & 0 & 0 & 0 \\ 0 & 0 & 0 & A_{55} & 0 & 0 & 0 & 0 \\ 0 & 0 & 0 & 0 & A_{66} & 0 & 0 & B_{66} \\ B_{11} & B_{12} & 0 & 0 & 0 & D_{11} & D_{12} & 0 \\ B_{12} & B_{22} & 0 & 0 & 0 & D_{12} & D_{22} & 0 \\ 0 & 0 & 0 & 0 & B_{66} & 0 & 0 & D_{66} \end{bmatrix} \begin{Bmatrix} \varepsilon_{x0} \\ \varepsilon_{y0} \\ \gamma_{yz} \\ \gamma_{xz} \\ \gamma_{xy0} \\ \kappa_x \\ \kappa_y \\ \kappa_{xy} \end{Bmatrix} \quad (2\text{-}1)$$

For considering the ITPS panel as an orthotropic plate, the following assumptions were made:

- The displacements are small compared to the panel thickness.
- The ITPS panel has a much larger *L/d* ratio, say greater than eight, for the homogenization to be applicable.
- The plate deformation in the thickness direction is negligible.
- There is no local buckling on the face sheets and the core thickness remains constant.

Unlike the analytical models the face sheets and web laminates need not be symmetric with respect to their own mid-planes and also the top and bottom face sheets need not be identical as the finite element (FE) approach can capture any variable material properties and geometries. An FE analysis is performed on the unit cell using the commercial ABAQUS® finite element program. The ITPS unit cell is modeled with eight node shell elements and the stiffness properties are obtained by forcing the unit cell to six linearly independent deformations. Deformations, in-plane strains, and curvatures, are imposed on the FEM model by enforcing periodic displacement boundary conditions derived in the next section. To prevent rigid body motion one of the corner nodes is also fixed.

Periodic Boundary Conditions

For the derivation of periodic boundary condition, we will consider the displacement field $u(x,y,z), v(x,y,z) \text{ and } w(x,y,z)$ within the unit cell, which is a hexahedron of size *a*×*b*×*h*. Our goal is to determine a set of boundary conditions (BCs) that need to be applied on the surfaces of the unit cell such that the average deformation in the unit cell is equal to a given value. There are infinite sets of BCs for a given average strain. However, when the condition of periodicity is imposed, the periodic BCs become almost unique. Before we derive the periodic BCs for various average deformations, there are few assumptions which are used in the derivation. They are as follows:

- Materials are homogeneous and orthotropic.
- Plate is assumed to be in the *xy*-plane with unit cells repeating in the *x* and *y* directions (Figure 2-3).
- The plate is subjected to a uniform state of strain in the macroscopic sense (Figure 2-3).
- All unit cells have identical stress and strain fields in micro scale. For the continuity of micro stresses across the unit cell it is required that tractions are equal and opposite at corresponding points on opposite faces of the unit cell.

For the derivation it is worth noting that the various unit cells must undergo identical deformations. This requires that the deformed surface S_{+x} - the surface normal to the positive *x* direction - should be obtained by translating and rotating the deformed surface S_{-x} (Figure 2-4). Then one can write:

$$\begin{aligned} u(a,y,z) - u(0,y,z) &= C_1 + R_1 z \\ v(a,y,z) - v(0,y,z) &= C_2 - R_2 z \\ w(a,y,z) - w(0,y,z) &= C_3 + R_2 y \end{aligned} \tag{2-2}$$

where the constants C_1, C_2 and C_3 represent the rigid body translations in the *x, y* and *z* directions, respectively, and R_1 and R_2 represent rotations about the *y*- and *x*-axes, respectively. Similarly, one can relate the displacements on the two parallel surfaces *y*=0 and *y*=*b* as

$$\begin{aligned} u(x,b,z) - u(x,0,z) &= C_4 + R_3 z \\ v(x,b,z) - v(x,0,z) &= C_5 - R_4 z \\ w(x,b,z) - w(x,0,z) &= C_6 - R_3 x \end{aligned} \tag{2-3}$$

where the constants C_4, C_5 and C_6 represent the rigid body translations in the *x*, *y* and *z* directions, respectively, and R_3 and R_4 represent rotations about the *y*- and *x*-axes, respectively.

The procedure for determining the constants *C*'s and *R*'s is described below. Consider the homogeneous deformation of a plate. Then, the mid-plane strains and curvatures are constant throughout the plate, and they can be written as:

$$\varepsilon_{x0} = \frac{\partial u_0}{\partial x} = \bar{\varepsilon}_{x0},\ \varepsilon_{y0} = \frac{\partial v_0}{\partial y} = \bar{\varepsilon}_{y0},\ \gamma_{xy0} = \frac{\partial u_0}{\partial y} + \frac{\partial v_0}{\partial x} = \bar{\gamma}_{xy0} \tag{2-4}$$

$$\kappa_x = \frac{\partial \psi_x}{\partial x} = \bar{\kappa}_x, \kappa_y = \frac{\partial \psi_y}{\partial y} = \bar{\kappa}_y, \kappa_{xy} = \frac{\partial \psi_x}{\partial y} + \frac{\partial \psi_x}{\partial y} = \bar{\kappa}_{xy}, \tag{2-5}$$

In Equation 2-4 and Equation 2-5 the quantities with an over bar denote the constant values of the deformation. The mid-plane displacements are denoted by $u_0(x,y)$ and $v_0(x,y)$, and the rotations are $\psi_x(x,y)$ and $\psi_y(x,y)$. It should be noted that in the case of homogeneous deformation, in-plane force resultants, N_x, N_y and N_{xy}, and moment resultants, M_x, M_y and M_{xy}, are also constant throughout the plate. Then, from the plate equilibrium equations given below one can note that the transverse shear forces, Q_x and Q_y, must vanish for the case of homogeneous deformation:

$$Q_x = \frac{\partial M_x}{\partial x} + \frac{\partial M_{xy}}{\partial y},\ Q_y = \frac{\partial M_{xy}}{\partial x} + \frac{\partial M_y}{\partial y} \tag{2-6}$$

Assuming that in-plane and transverse shear deformations are uncoupled, which is the case in most plates and plate-like structures, the transverse shear strains should also vanish:

$$\begin{aligned} \gamma_{xz} &= \psi_x + \frac{\partial w}{\partial x} = 0 \Rightarrow \frac{\partial w}{\partial x} = -\psi_x \\ \gamma_{yz} &= \psi_y + \frac{\partial w}{\partial y} = 0 \Rightarrow \frac{\partial w}{\partial y} = -\psi_y \end{aligned} \tag{2-7}$$

where *w(x,y)* is the transverse deflection of the plate.

The three differential equations for u_0 and v_0 in Equation 2-4 can be integrated to obtain:

$$\begin{aligned} u_0(x,y) &= \bar{\varepsilon}_{x0} x + \frac{1}{2}\bar{\gamma}_{xy0} y \\ v_0(x,y) &= \frac{1}{2}\bar{\gamma}_{xy0} x + \bar{\varepsilon}_{y0} y \end{aligned} \tag{2-8}$$

In deriving the above we have used the conditions that rigid body displacements and the rigid body rotation about the *z*- axis vanish. Similarly integrating the three equations for $\psi_x(x,y)$ and $\psi_y(x,y)$ in Equation 2-5 and the two equations for *w*(*x*,*y*) in Equation 2-7 we obtain:

$$\begin{aligned} \psi_x(x,y) &= \bar{\kappa}_x x + \frac{1}{2}\bar{\kappa}_{xy} y \\ \psi_y(x,y) &= \frac{1}{2}\bar{\kappa}_{xy} x + \bar{\kappa}_y y \\ w(x,y) &= -\frac{1}{2}\left(\bar{\kappa}_x x^2 + \bar{\kappa}_{xy} xy + \bar{\kappa}_y y^2\right) \end{aligned} \tag{2-9}$$

Again, in deriving the above we have used the condition that $\psi_x(0,0) = \psi_y(0,0) = w(0,0) = 0.$

Expressions in Equation 2-8 and Equation 2-9 represent a homogeneous deformation in a plate. We use this displacement field to calculate the relative displacements in Equation 2-2 and Equation 2-3. For example, consider:

$$u(a,y,z)-u(0,y,z)=\left[u_0(a,y,z)-u_0(0,y,z)\right]+z\left[\psi_x(a,y,z)-\psi_x(0,y,z)\right] \quad (2\text{-}10)$$

Substituting for the mid-plane displacements and rotations from Equation 2-8 and Equation 2-9 into Equation 2-10 we obtain:

$$u(a,y,z)-u(0,y,z)=\bar{\varepsilon}_{x0}a+z\bar{\kappa}_x a \quad (2\text{-}11)$$

Comparing the above relative displacement with that in Equation 2-2 the constants C_1 and R_1 can be derived as:

$$C_1=\bar{\varepsilon}_{x0}a,\ \ R_1=\bar{\kappa}_x a \quad (2\text{-}12)$$

Similarly from the other relative displacements in Equation 2-2 we can derive the other constants also as shown below:

$$C_2=\frac{1}{2}\bar{\gamma}_{xy0}a,\ \ R_2=-\frac{1}{2}\bar{\kappa}_{xy}a,\ C_3=-\frac{1}{2}\bar{\kappa}_x a^2 \quad (2\text{-}13)$$

Using the relative displacements in Equation 2-3 we derive the following:

$$\begin{aligned} &C_4=\frac{1}{2}\bar{\gamma}_{xy0}b,\ \ C_5=\bar{\varepsilon}_{y0}b,\ \ C_6=-\frac{1}{2}\bar{\kappa}_y b^2 \\ &R_3=\frac{1}{2}\bar{\kappa}_{xy}b,\ \ R_4=-\bar{\kappa}_y b \end{aligned} \quad (2\text{-}14)$$

Substituting for *C*'s and *R*'s in Equation 2-2 and Equation 2-3, we obtain the periodic boundary conditions as:

$$\begin{aligned} u(a,y,z)-u(0,y,z)&=\bar{\varepsilon}_{x0}a+\bar{\kappa}_x az \\ v(a,y,z)-v(0,y,z)&=\frac{1}{2}\bar{\gamma}_{xy0}a+\frac{1}{2}\bar{\kappa}_{xy}az \\ w(a,y,z)-w(0,y,z)&=-\frac{1}{2}\bar{\kappa}_x a^2-\frac{1}{2}\bar{\kappa}_{xy}ay \end{aligned} \quad (2\text{-}15)$$

$$
\begin{aligned}
u(x,b,z) - u(x,0,z) &= \frac{1}{2}\bar{\gamma}_{xy0} b + \frac{1}{2}\bar{\kappa}_{xy} bz \\
v(x,b,z) - v(x,0,z) &= \bar{\varepsilon}_{y0} b + \bar{\kappa}_{y} bz \\
w(x,b,z) - w(x,0,z) &= -\frac{1}{2}\bar{\kappa}_{y} b^2 - \frac{1}{2}\bar{\kappa}_{xy} bx
\end{aligned}
\tag{2-16}
$$

The periodic boundary conditions (PBCs) in Equation 2-15 and Equation 2-16 are presented in Table 2-1.

It should be mentioned that the PBCs in Table 2-1 are in terms of displacements *u*, *v* and *w*, and can be implemented easily when solid elements are used in the FE model of the unit cell. However, there are instances when shell elements are used to model the unit cell of a plate with microstructure. In such cases the above BCs have to be modified to include the rotational DOFs present at the nodes of shell elements. First we note that only those BCs that depend on *z* in Table 2-1 will be modified. Noting that the global rotations θ_x and θ_y, respectively about the *x*- and *y*- axes, are related to the displacement gradients as $\frac{\partial u}{\partial z} = +\theta_y$ and $\frac{\partial v}{\partial z} = -\theta_x$, we derive the additional PBCs for rotations as shown in Table 2-2. The PBCs for three in plane strains and three curvatures are in terms of non-zero boundary conditions in *u*, *v*, *w*, θ_x and θ_y.

The procedure for determining the ABD stiffness matrix is as follows. There are six macroscopic deformations which have to be applied independently as shown in Table 2-3. The unit cell is forced to six linearly independent deformations. One deformation is considered to be non zero and all other deformations are equal to zero. For example, the deformation, ε_{x0} = 1 is applied and the rest of the macroscopic strains and curvature are maintained to be zero. By doing this, the nodal stresses are obtained at the boundaries from the FE output after the analysis (Figure 2-5). Using the nodal stresses the nodal forces are obtained, and nodal moments are obtained by multiplying the nodal

forces by the distance from the mid plane. The nodal forces and moments of the boundary nodes are then summed to obtain the force and moment resultants as:

$$\begin{aligned}
\left[N_x, M_x\right] &= \frac{1}{b}\sum_{m=1}^{tn}[1, z]F_x^{(m)}(a, y, z) \;\rightarrow\; \text{For the face } x = a \\
\left[N_{xy}, M_{xy}\right] &= \frac{1}{b}\sum_{m=1}^{tn}[1, z]F_y^{(m)}(a, y, z) \;\rightarrow\; \text{For the face } x = a \\
\left[N_y, M_y\right] &= \frac{1}{a}\sum_{m=1}^{tn}[1, z]F_y^{(m)}(x, b, z) \;\rightarrow\; \text{For the face } y = b
\end{aligned} \tag{2-17}$$

where $F_x^{(m)}$ and $F_y^{(m)}$ are the nodal forces in the *x* and *y* directions at the m^{th} node and '*tn*' is the total number of nodes on the face.

From the force and moment resultants calculated, the first column of the stiffness matrix is obtained. The same procedure is repeated for other five cases and the ABD matrix is fully populated. If the process is performed correctly, the stiffness matrix comes out to be symmetric.

Transverse Shear Stiffness A_{44} and A_{55}

Past studies have indicated that the corrugated core sandwich panels have low transverse shear rigidity and thus transverse shear deformations are significant. In addition to the ABD matrix, there is a need to estimate the transverse shear stiffness terms A_{44} and A_{55} for the equivalent orthotropic plate. However, there is a contradiction in terms of transverse shear stiffness homogenization. Homogenization assumes every unit cell is subjected to identical deformations which are valid under in-plane forces or bending moments. Whenever a transverse shear force is applied, the shear force is constant along the entire structure. However, the bending moment will vary linearly along the structure because by definition, the shear force is $\frac{dM}{dx}$, the gradient of bending moment. That means whenever there is a shear force, there has to be a variation of the

bending moment. This variation of the bending moment along the length of the structure violates this homogenization that every unit cell is subjected to identical force and moment resultant and deformations. Therefore, there is a kind of conundrum here. Analyzing one unit cell to obtain the average transverse shear stiffness of the structure is not possible. Instead we take a one-dimensional beam with length of several unit cells. Below a finite element based method is described to obtain the required transverse shear stiffness properties, A_{44} and A_{55}.

Cantilever Beam, with Pressure Load on the Top Face Sheet: In the present approach a beam is considered that consists of one unit cell in the width direction and several unit cells (say 10) in the length direction. The beam is clamped at one end. The beam is subjected to a uniformly distributed load. The deflection of the plate is obtained using a one-dimensional plate with unit cells in one direction (*x* and *y* direction for A_{55} and A_{44}, respectively). Figure 2-6 and Figure 2-7 shows the typical mesh and finite element model for the estimation of the transverse shear stiffness A_{55} and A_{44}, respectively.

The same structure is analyzed using a plate model. The transverse deflection obtained is compared with the shear deformable plate theory deflection, which consists of bending and shears deflections. Using shear deformable plate theory one can derive an expression for the transverse deflection in the direction where we have continuous webs (for transverse shear stiffness, A_{55}) as:

$$w(L_{ex}) = -\frac{P_0 L_{ex}^2}{2A_{55}} - \frac{P_0 L_{ex}^{\ 4}}{8D_{11}^{'}}$$
$$D_{11}^{'} = D_{11} - \frac{B_{11}^2}{A_{11}} \qquad (2\text{-}18)$$

From Equation 2-18, the FE transverse deflection solution is compared to the plate deflection solution. The FE result for deflection is exact. The second term on the right hand side of the Equation 2-18, is the bending deflection term which can be calculated. The reduced stiffness coefficient D_{11}' is used for unsymmetric beams and it can be calculated, as the A_{11}, B_{11} and D_{11} are already known from the ABD stiffness as mentioned in the previous section. Therefore, once the bending deflection term is taken away from the total FE transverse deflection, the remaining term is due to transverse shear, from which A_{55} can be calculated. Similarly, the transverse shear stiffness A_{44} can be derived in the direction where we do not have continuous webs as given below:

$$w(L_{ey}) = -\frac{P_0 L_{ey}^2}{2A_{44}} - \frac{P_0 L_{ey}^4}{8D_{22}^{'}}$$
$$D_{22}^{'} = D_{22} - \frac{B_{22}^2}{A_{22}} \qquad (2\text{-}19)$$

The ABD matrices and the transverse shear stiffness A_{44} and A_{55} obtained using homogenization are then inputted into the FE program for the two-dimensional homogenized plate analysis. We will validate our calculation of the transverse shear stiffness by assuming it as a shear deformable plate. We will also compare the maximum transverse deflection with the 3D model under the pressure load as discussed in the Results section.

Results

For verification of the effectiveness of the FE based homogenization method, consider a corrugated-core sandwich panel unit cell with the following dimensions: p = 25 mm, d = 70 mm, t_{TF} = 1.2 mm, t_{BF} = 7.49 mm, t_w = 1.63 mm, θ = 85^o. For the 3D FE analysis the whole panel consists of 40 unit cells. In the example, the TFS and the web

are modeled using Titanium alloy, Ti-6Al-4V (E_1 = 109 GPa and ν = 0.3) and the BFS is modeled using Beryllium alloy (E_1 = 290 GPa and ν = 0.063) [20]. For the 3D FE model, one fourth of the ITPS panel containing half the total number of unit cells is modeled using ABAQUS® finite element (FE) software. The model uses approximately 75,000 eight-node shell elements (S8R). The mesh convergence was ascertained by reducing the dimension of the element's edges by half and repeatedly solving the pressure analysis till the maximum transverse deflection was less than 2%. The boundary conditions considered are: fixed vertical displacements for the bottom face sheet (w = 0) and fixed rotations for the top face sheet ($\theta_x = \theta_y = 0$) on the edges of the panel. On the symmetric edges, symmetric boundary conditions are used (Figure 2-8).

For the homogenized model, again the one-fourth plate is used due to symmetry. Shell elements in ABAQUS® finite element (FE) software were used. The model used a total of 40,400 eight-node shell elements (S8R). A simply supported boundary condition is considered along the boundary of the plate (w = 0). The plate edges were allowed to move in the horizontal plane (Figure 2-9).

Stiffness Matrix of an ITPS Sandwich Panel

The equivalent stiffness constants of the orthotropic plate were obtained using homogenization described in the previous section (Section-Periodic Boundary Conditions). Due to different thicknesses and different material properties of the TFS and BFS, there will be a coupling between the extensional and bending deformations. Figure 2-10 shows how the unit cell deforms for the six cases when it is forced to six linearly independent deformations. The values are given below:

$$[A]=\begin{bmatrix}2.83 & 0.18 & 0\\ 0.18 & 2.33 & 0\\ 0 & 0 & 1.07\end{bmatrix}\times 10^{9}\,\frac{N}{m},\quad [B]=\begin{bmatrix}-71.45 & -3.36 & 0\\ -3.36 & -71.45 & 0\\ 0 & 0 & -34.05\end{bmatrix}\times 10^{6}\,N$$
$$[D]=\begin{bmatrix}3.06 & 0.22 & 0\\ 0.22 & 2.85 & 0\\ 0 & 0 & 1.32\end{bmatrix}\times 10^{6}\,N-m \qquad (2\text{-}20)$$

In order to verify the calculation of *ABD* matrix, a one dimensional plate (in this case along *x*- direction) is taken (Figure 2-11). The BC's on the two sides are given by *y = 0* and *y = b* under plane-strain conditions. The edge at *x = 0* is clamped, whereas at the other end given by at *x = a*, a uniform bending moment is applied. The reduced stiffness (for this case D_{11}') is inputted into the 2D FE model and the analysis is performed. The plate deflection due to uniform bending moment is compared with the exact 3D FE analysis (Figure 2-12). Figure 2-13 shows the comparison of the deflection between the plate model and the 3D deflection and as seen from the graph they both compares well. This verifies that our calculation for A_{11}, B_{11} and D_{11} is correct.

Similarly, A_{22}, B_{22} and D_{22} is verified by repeating the unit cells along the *y*-direction and comparing the exact 3D FE deflection under uniform moment (Figure 2-14) and comparing the 2D FE plate deflection under uniform moment. This time the reduced stiffness D_{22}' is inputted into the 2D FE model. Figure 2-15 shows the comparison between the two. There is a slight error near the boundary where the bending moment is applied. The bending moment is uniform throughout the plate whereas in the exact 3D FE model the bending moment becomes uniform only at a distance away from the point of application due to St. Venant's phenomenon. Therefore, there is a slight discrepancy in the prediction of deflection near the point of application of bending moment. Also, there are infinite numbers of unit cells along *x*- direction,

whereas there are discreet numbers of unit cells along *y*- direction. Hence, the deflection error in the case along the *y*- direction is greater than that in the *x*- direction. However, this validates that the calculation of the ABD stiffness matrix is correct.

Prediction of Transverse Shear Stiffness

As mentioned earlier, the transverse shear stiffnesses, A_{44} and A_{55} are predicted by applying the pressure load for clamped boundary conditions and comparing the total deflection with the plate deflection which is composed of bending and shear deflections (Figure 2-6 and Figure 2-7). The accuracy of the transverse shear stiffness results depends on the length of the beam. If a very long beam is considered, then the bending deflection dominates the shear deflection (Equation 2-18 and Equation 2-19), leading to errors in the calculation of the shear stiffnesses. The shear stiffness is evaluated based on shear deformation, which is small compared to bending deformation. On the other hand, short beams, wherein the shear is significant, have other problems. For a short beam, the shear deformation is significant; however the boundary effects come into play. There are two boundary effects. One the way the structure is supported or clamped, which propagates for some distance. The other effect comes from the way the load is applied and that comes from the free surface where there is some end effects. Therefore, these two effects contribute significantly to the deflection when a short beam is considered, which leads to errors. So, there has to be an optimum value, which could be neither too short nor too long in order to have a good estimate of the shear deflection. But again this estimate of shear deflection depends on the transverse shear stiffness itself, in fact on the ratio between the transverse shear stiffness and the bending stiffness. Therefore different beams, different cross-sections need different lengths to get accurate values of the transverse shear stiffness.

As seen from Figure 2-16, when the beam is very short, large error occurs due to boundary conditions at the support. This is not the correct value. However as the length of the beam increases the value almost converges to the steady state value. In Figure 2-16, the graph shows the transverse shear stiffness, A_{44} which was obtained on displacements at different points from one beam analysis of 20 unit cells. Therefore, for this type of beams, L/d = 10 should be good where the shear deformation are comparable to bending deformation and also it is not a very short beam so the boundary effects due to support also dies out. Next we look into the estimation of transverse shear stiffness, A_{55}. As seen from Figure 2-17, again large errors are seen due to boundary effects for very short beams. Also again when the beam length becomes larger and longer, the value of shear stiffness starts increasing, which is a numerical error as explained earlier. Actually the transverse shear stiffness, A_{55} is very high, approximately three orders high as compared to A_{44}, which means that for higher transverse shear stiffness, the shear deflection will be very small and as the beam length gets longer the transverse shear deformation effect becomes even small compared to the beam length and thus we encounter numerical errors. Therefore, we are not able to attain a constant value even though theoretically it was suppose to have constant shear stiffness at larger lengths. Again for approximately L/d = 10 should be good for which shear deformation is still comparable to bending deformation, though it was smaller as compared for A_{44}. This was the best we could do for this particular structure. Now having determined the *ABD* stiffness matrix and the transverse shear stiffness, we are going to validate the values as mentioned in the next section.

Validation of Transverse Shear Stiffness

The extension, bending, coupling and the transverse shear stiffnesses calculated above are validated by assuming the corrugated core sandwich panel of the ITPS as a thick plate that is continuous, orthotropic, and homogeneous. We apply the transverse pressure of 101 kPa on to the plate model and compare the maximum deflection in the *z* direction for the 2D model with the 3D model. A simply supported boundary condition is considered along the boundary of the plate. The plate edges are allowed to move in the horizontal plane. Due to symmetry only one-fourth of the panel is modeled. Initially, we used the classical laminate plate theory (Kirchhoff plate) in which we only input the *ABD* matrices and assume the transverse shear stiffness to be infinitely large. Then, we considered the transverse shear stiffness properties, A_{44} and A_{55}, and performed the analysis using shear-deformable elements (shear deformable plate theory) (Figure 2-19).

A pressure load of 101 kPa is applied on the TFS of the 3D ITPS model. The boundary conditions considered are used as mentioned before. The 3D TFS maximum deflection in the *z* direction (Figure 2-18) is compared with the plate deflection. The maximum deflection occurs at the center of the ITPS panel. When we use the classical laminate plate theory (Kirchhoff plate), the percentage difference from the 3D model was 55% as compared using shear-deformable elements where the difference was only 3.6%. The results are shown in Table 2-4 and thus it validates that our calculation of the various stiffnesses are correct. After validating the transverse shear stiffnesses, some parametric studies were also performed. In particular, we study the effect of web angle on A_{44}, A_{55} and maximum deflection as discussed in the next section.

Parametric Studies of the Transverse Shear Stiffness and the Maximum Deflection

The behavior of the transverse shear stiffness of the corrugated core sandwich panels is studied with the change in the angle of the web. Changes in A_{44} and A_{55} are important as it contributes to the panel deflection under pressure loading case. Consider the truss core sandwich panel of the following dimensions: p = 84.25 mm, d = 70 mm, t_{TF} = 1.2 mm, t_{BF} = 7.49 mm, t_w = 1.63 mm, a = 1.6845 m, b = 1.6845 m. The material used for the TFS and web is Titanium alloy, and Beryllium alloy for the BFS. The thickness of the web is described in such a way that the cross sectional area or the weight remains same for any given web angle. By doing this we can understand the variation of the stiffness to the change in angle only rather than changing the angle and thickness. The web angles are varied from 40^o, i.e. almost like triangular webs to, 90^o (rectangular webs). As seen from Figure 2-20, triangular webs have the maximum transverse shear stiffness, A_{44}. Triangular webs have the maximum length of the web for a given height of the sandwich panel and hence it has the maximum value of A_{44}. The variation of A_{44} from 90^o webs to triangular webs is almost two orders of magnitudes. However, the variation in the transverse shear stiffness, A_{55} with the change in web inclination is not as much as A_{44} but as expected the maximum value of A_{55}, is for 90^o web angle (Figure 2-21). Due to this variation of A_{44} and A_{55} with web angle, the maximum deflection will also change with the applied pressure.

Figure 2-22 shows the variation of the maximum deflection under the applied pressure with the change in web angle. As the web angle is increased to 90^o, it becomes less stiff and the maximum deflection increases, whereas with the decrease of the web angle, the plate becomes very stiff. The combination of A_{44} and A_{55} also plays

the role for the variation of the maximum deflection under the applied pressure. Therefore, the web angle should also be a parameter in design optimization. It is also noted that the web angle also controls the amount of heat transferring from the TFS to the BFS. Therefore, it's a very critical parameter from the heat transfer point also.

Next, we looked into the variation of the percentage difference in the maximum deflection with changes in A_{44} and A_{55}. For classical laminate plate theory, since we neglect the effect of transverse shear stiffness, the ratio of the exact value of A_{44} or A_{55} to its respective A_{44} or A_{55} value is 0 (Figure 2-23 and Figure 2-24). Whereas for the shear deformable plate theory, the ratio to the exact value of A_{44} or A_{55} to its respective A_{44} or A_{55} value is 1 (Figure 2-23 and Figure 2-24). Therefore, we varied this ratio from 0 to 1 and compared it with the percentage difference in the maximum deflection between the 2D and 3D value, in order to see the effects of A_{44} and A_{55} individually. When the effect of transverse shear A_{44} is neglected completely and keeping the exact value of A_{55}, the percentage error in the maximum deflection of the TFS between the 3D and 2D under transverse load is almost 54%.(Figure 2-23) However, when only the effect of transverse shear A_{55} is neglected completely and keeping the exact value of A_{44}, the percentage error in the maximum deflection of the TFS between 3D and 2D is only 5.6% (Figure 2-24). Therefore, these two graphs tell that even if there is not the correct estimate of A_{55} it does not matter. One can assume A_{55} as infinity and still get a good result of the maximum deflection from the 2D plate model under pressure load. Whereas the correct estimation of A_{44} is very important, otherwise there is going to be a large error in the maximum deflection prediction from the 2D model when compared with the corresponding 3D maximum deflection under pressure load.

Concluding Remarks

In this chapter, a finite element based homogenization procedure is developed for modeling corrugate sandwich panels as a 2D orthotropic plate. Corrugated sandwich panels are potential candidates for the integrated thermal protection systems for future aerospace vehicles. The periodic boundary conditions are derived in a formal way to obtain the bending, extensional, and coupling stiffness for an ITPS panel using finite element approach. The transverse shear stiffness properties are also derived using an FE approach. The biggest advantage of finite element based micromechanical analysis is that it is capable of handling any combination of material properties for face sheets and webs, and any geometry.

Effect of web angle on various stiffness properties of the ITPS was studied. For a given plate dimension and loading, maximum deflection occurs for web angle of 90-degrees whereas the minimum deflection occurred when the webs take a triangular configuration. Finally the results of various stiffnesses are validated by applying a transverse pressure on to the 2D plate model and 3D ITPS panel. Agreement between 2D and 3D results for transverse deflection was good.

Table 2-1. The six sets of periodic boundary conditions applied to the lateral surfaces of the unit cell to determine the *A, B* and *D* matrices of the equivalent orthotropic plate.

	u(a,y)-u(0,y)	*v(a,y)-v(0,y)*	*w(a,y)-w(0,y)*	*u(x,b)-u(x,0)*	*v(x,b)-v(x,0)*	*w(x,b)-w(x,0)*
$\varepsilon_{x0}^{M} = 1$	*a*	*0*	*0*	*0*	*0*	*0*
$\varepsilon_{y0}^{M} = 1$	*0*	*0*	*0*	*0*	*b*	*0*
$\gamma_{xy0}^{M} = 1$	*0*	*a/2*	*0*	*b/2*	*0*	*0*
$\kappa_{x}^{M} = 1$	*az*	*0*	$-a^2/2$	*0*	*0*	*0*
$\kappa_{y}^{M} = 1$	*0*	*0*	*0*	*0*	*bz*	$-b^2/2$
$\kappa_{xy}^{M} = 1$	*0*	*az/2*	*-ay/2*	*bz/2*	*0*	*-bx/2*

Note: Superscript M denotes macro scale deformations

Table 2-2. Additional periodic boundary conditions on rotations θ_x and θ_y when shell elements are used to model the unit cell.

	$\theta_x(a,y) - \theta_x(0,y)$	$\theta_y(a,y) - \theta_y(0,y)$	$\theta_x(x,b) - \theta_x(x,0)$	$\theta_y(x,b) - \theta_y(x,0)$
$\varepsilon_{x0}^{M} = 1$	*0*	*0*	*0*	*0*
$\varepsilon_{y0}^{M} = 1$	*0*	*0*	*0*	*0*
$\gamma_{xy0}^{M} = 1$	*0*	*0*	*0*	*0*
$\kappa_{x}^{M} = 1$	*0*	*a*	*0*	*0*
$\kappa_{y}^{M} = 1$	*0*	*0*	*-b*	*0*
$\kappa_{xy}^{M} = 1$	*-a/2*	*0*	*0*	*b/2*

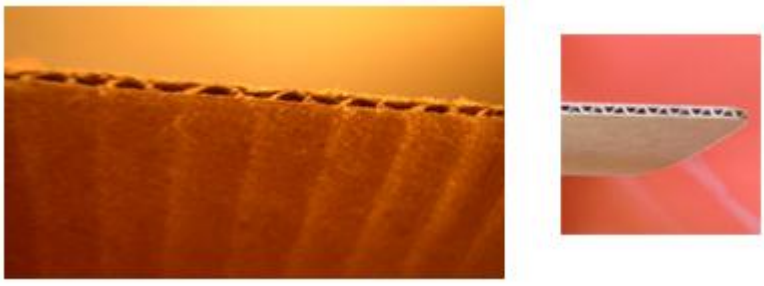

Figure 2-1. Corrugated cardboards.

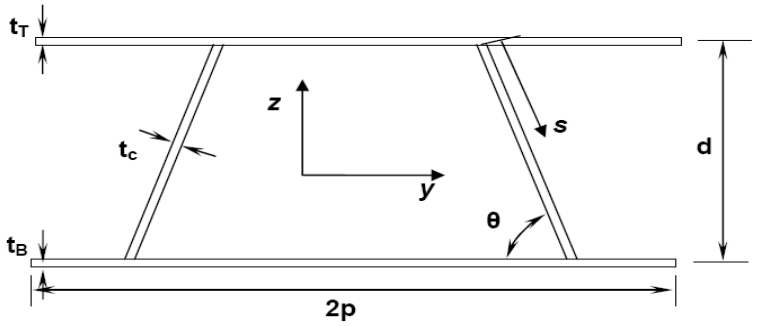

Figure 2-2. Unit-cell of the corrugated-core sandwich structure.

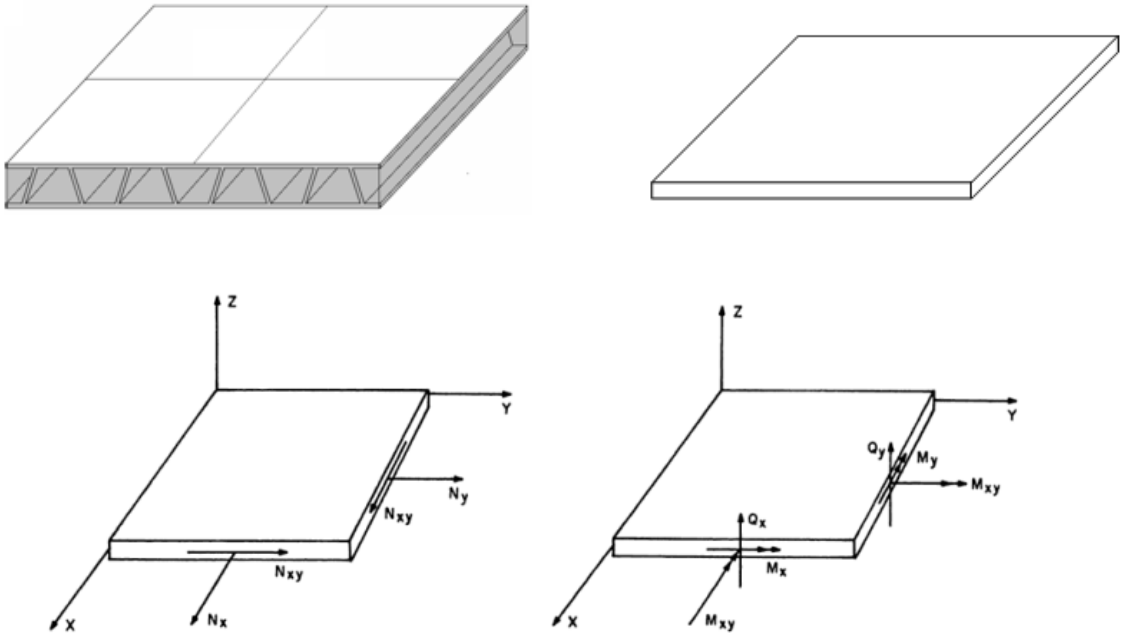

Figure 2-3. ITPS panel is modeled as a homogeneous orthotropic plate. For obtaining the Stiffness (ABD) matrices, it is subjected to uniform state of strain in macroscopic sense and hence subjected to uniform force and moment resultants (Whitney, M., Structural Analysis of Laminated Anisotropic Plates, Technomic, Lancaster, PA, 1987).

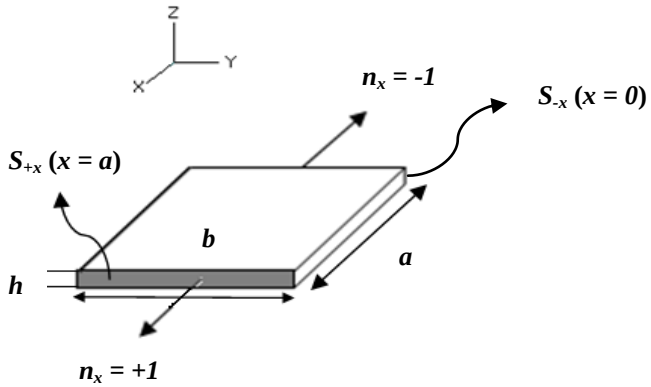

Figure 2-4. n_x is the outward unit normal, which has a value of +1 and -1 as shown and is equal to zero in the remaining faces.

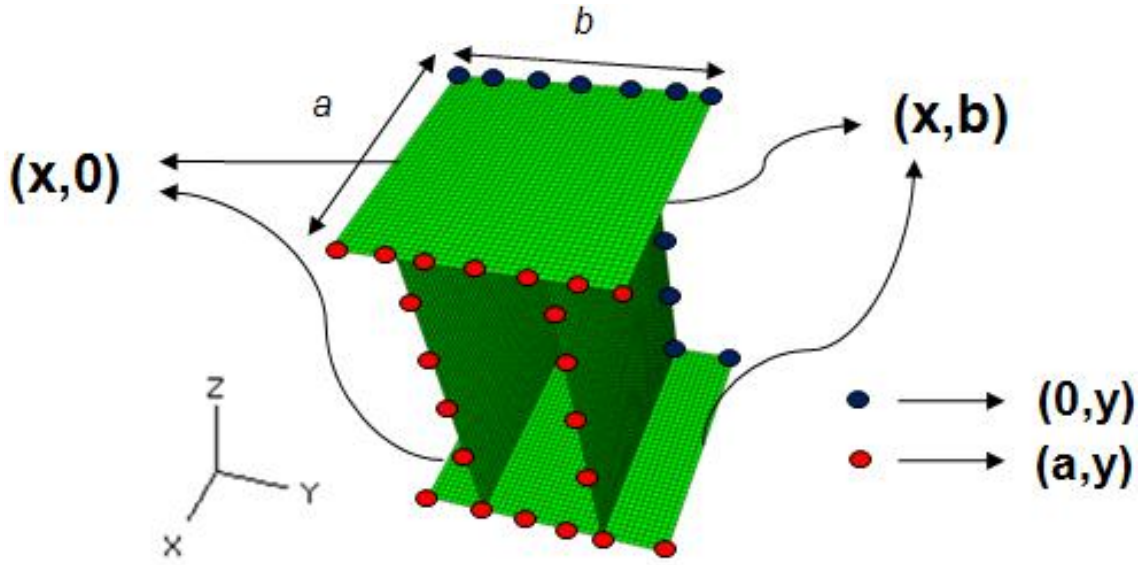

Figure 2-5. Finite element model of the unit cell.

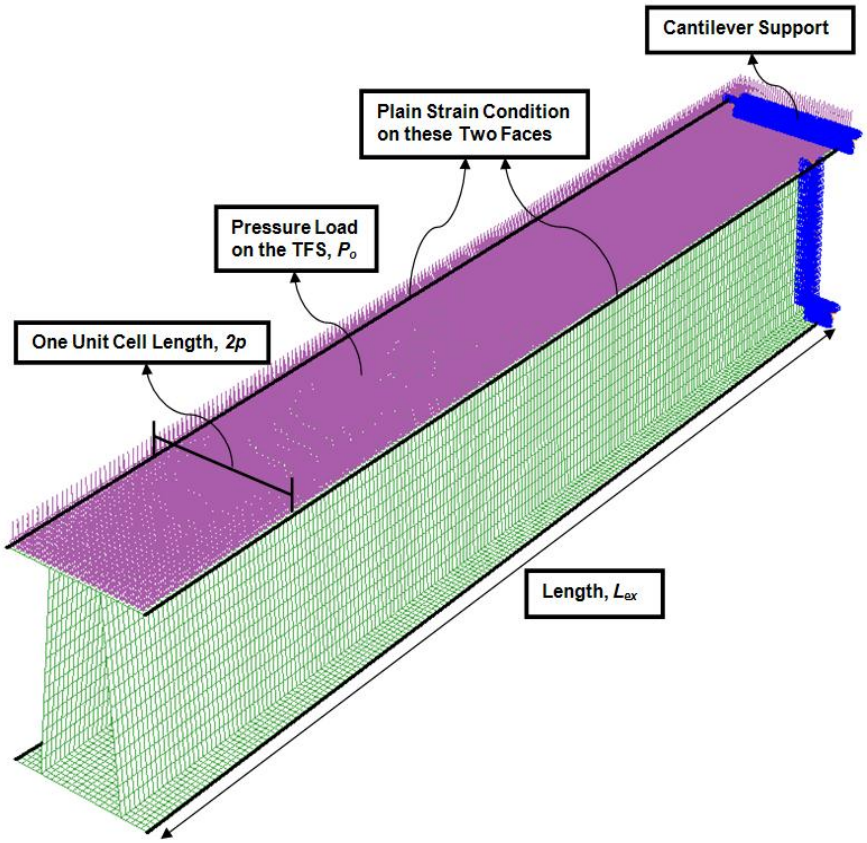

Figure 2-6. Typical mesh and finite element model for the estimation of transverse shear stiffness A_{55}.

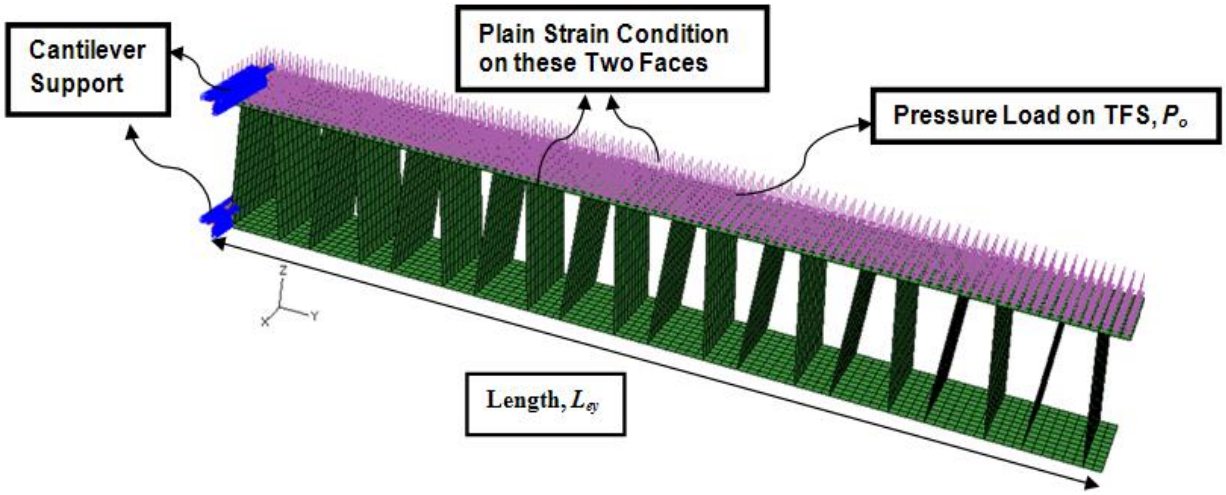

Figure 2-7. Typical mesh and finite element model for the estimation of transverse shear stiffness A_{44}.

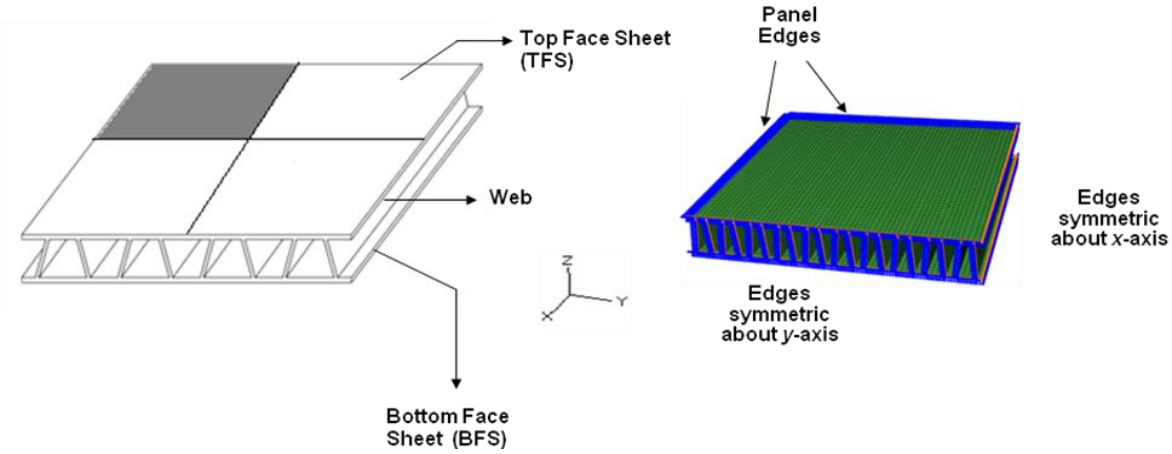

Figure 2-8. The ITPS panel and boundary conditions for the 3D finite element model of one fourth of the panel.

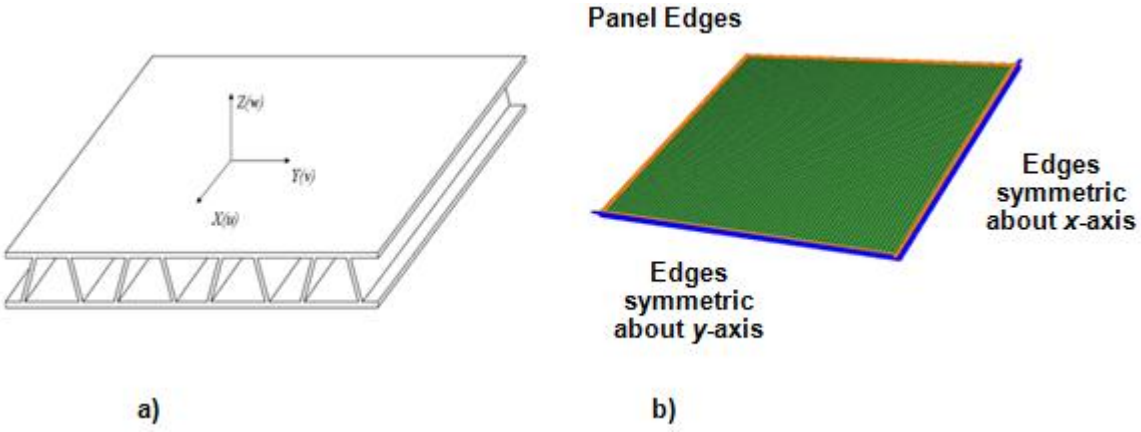

Figure 2-9. The ITPS panel is represented as a low fidelity two dimensional plate. a) One fourth of the ITPS panel, b) Typical mesh and boundary conditions for the low fidelity 2D finite element model.

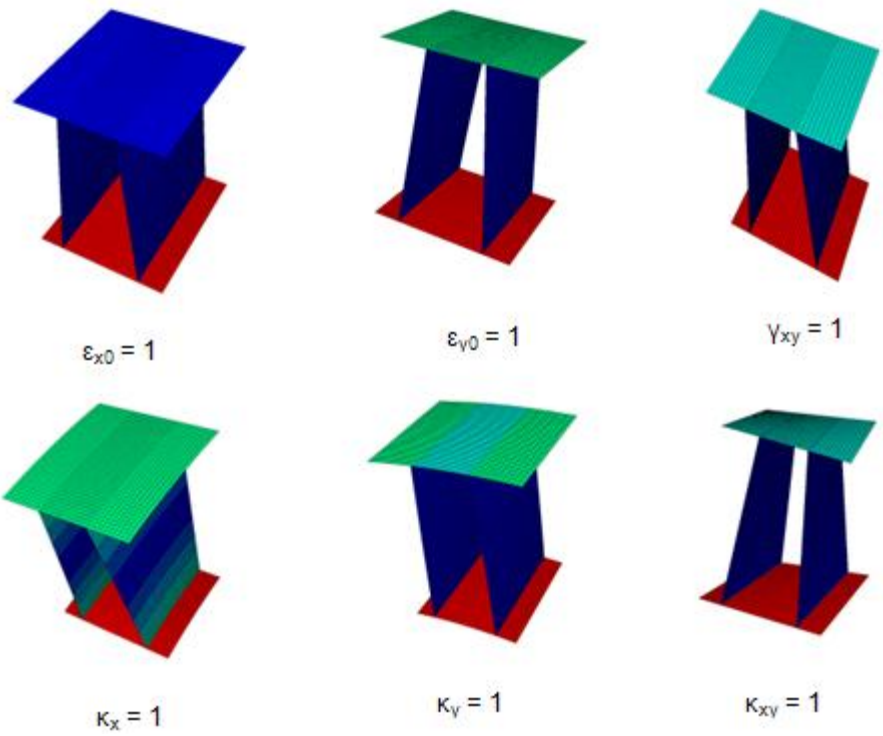

Figure 2-10. Unit cell deformations when periodic boundary conditions are imposed.

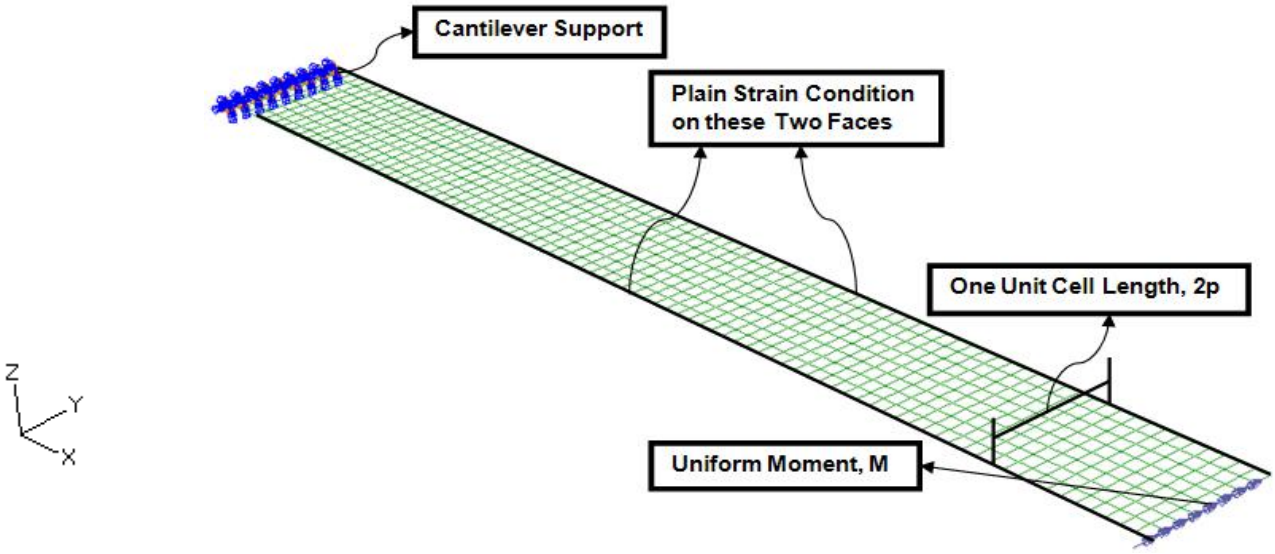

Figure 2-11. 2D plate model subjected to uniform moment in order to validate the ABD matrix in the direction where the webs are continuous.

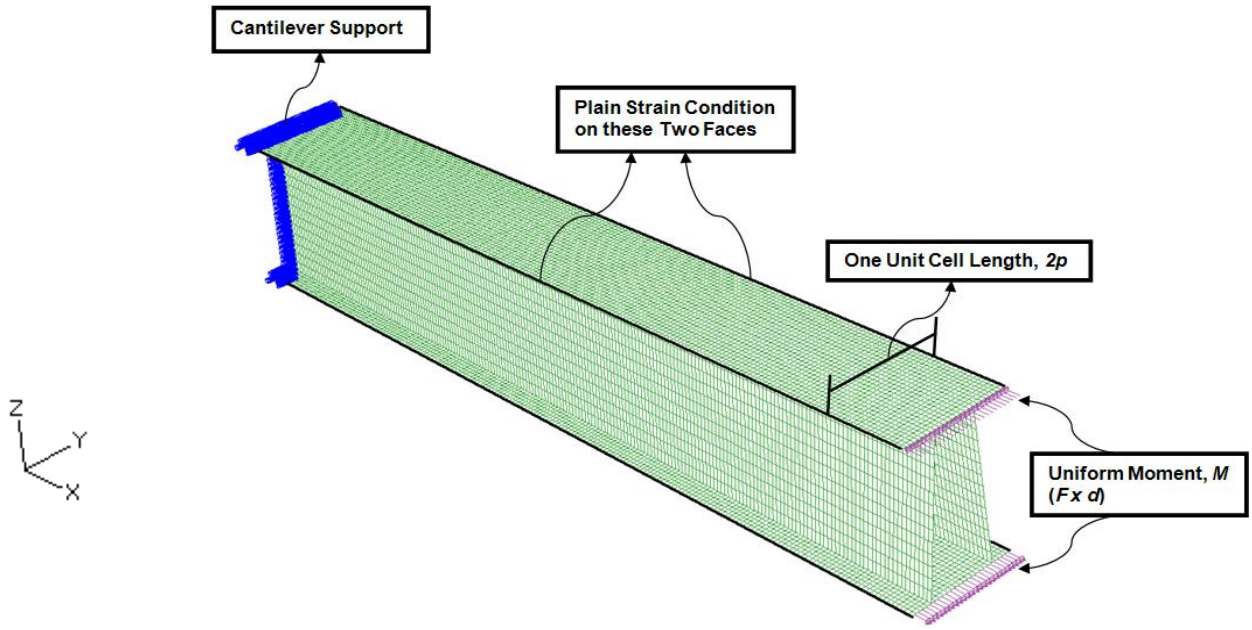

Figure 2-12. Exact 3D FE model subjected to uniform moment by applying an equal and opposite forces for the verification of the ABD stiffness matrix in the *x*-direction where the webs are continuous.

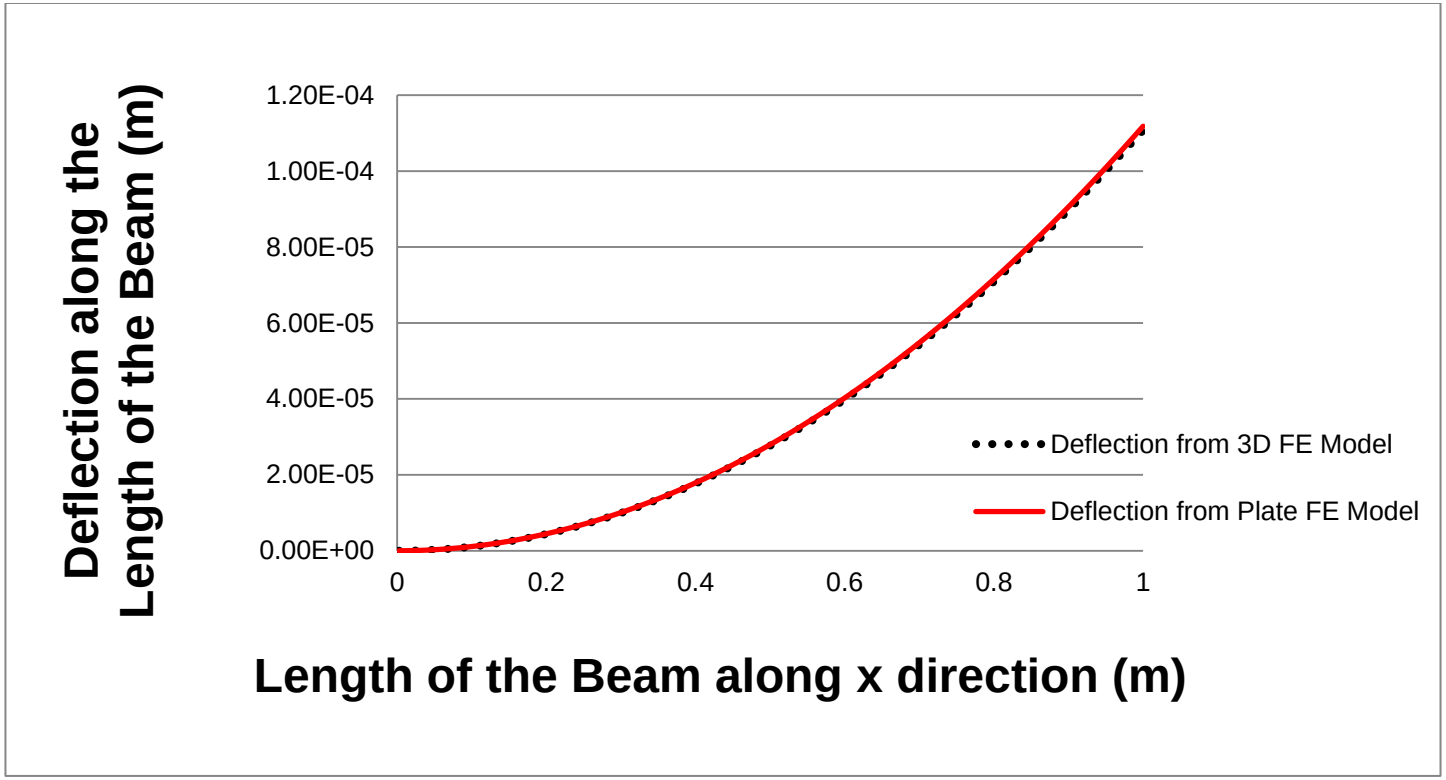

Figure 2-13. Comparison of the exact 3D FE deflection and the 2D FE plate deflection under uniform moment for the verification of the ABD stiffness matrix in the *x*- direction when the webs are continuous.

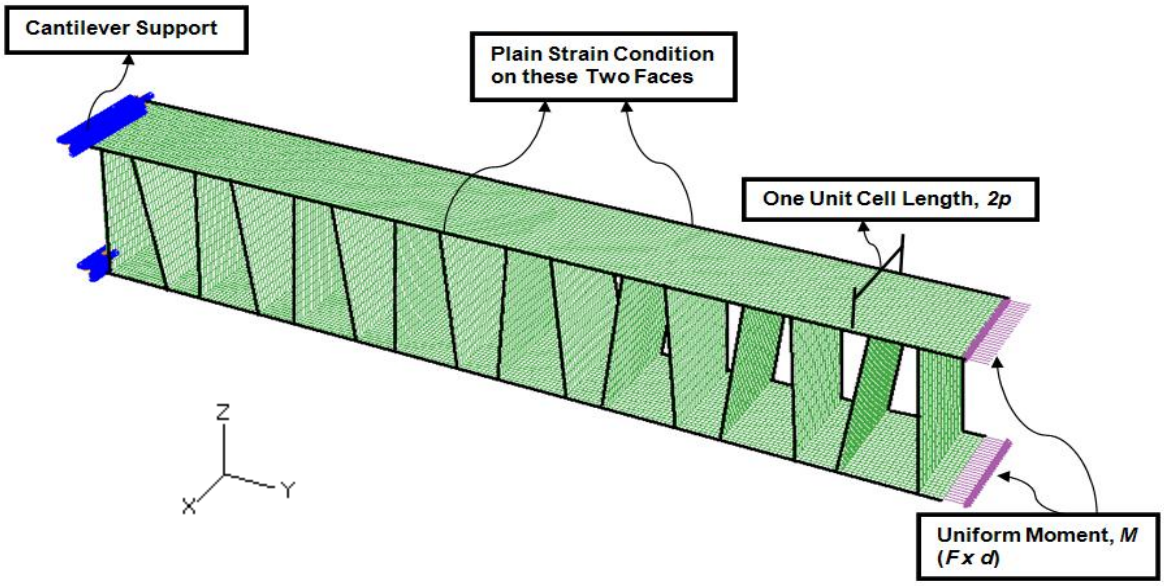

Figure 2-14. Exact 3D FE model subjected to uniform moment by applying an equal and opposite forces for the verification of the ABD stiffness matrix in the *y*-direction when the webs are not continuous.

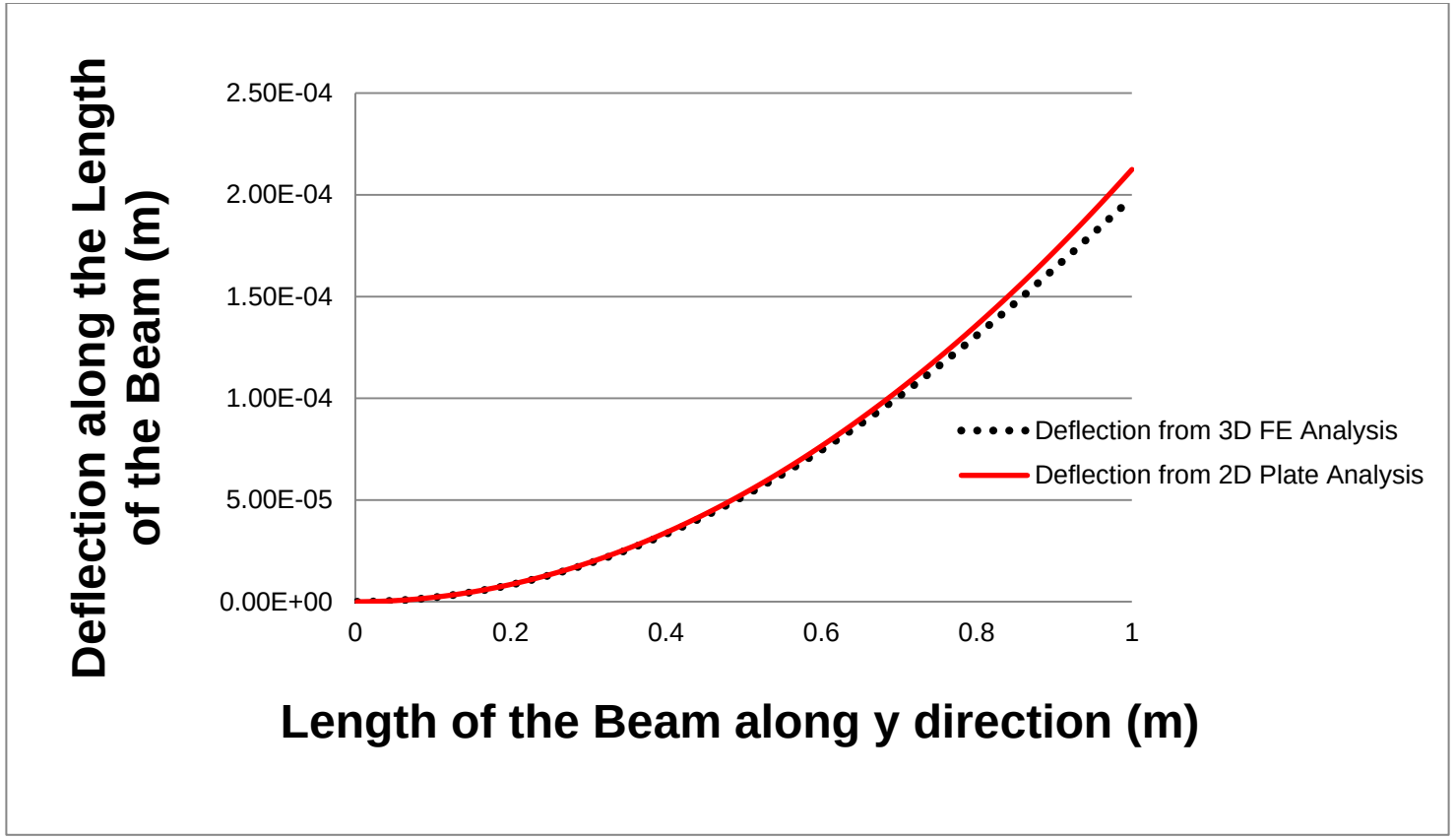

Figure 2-15. Comparison of the exact 3D FE deflection and the 2D FE plate deflection under uniform moment for the verification of the ABD stiffness matrix in the *y*- direction when the webs are not continuous.

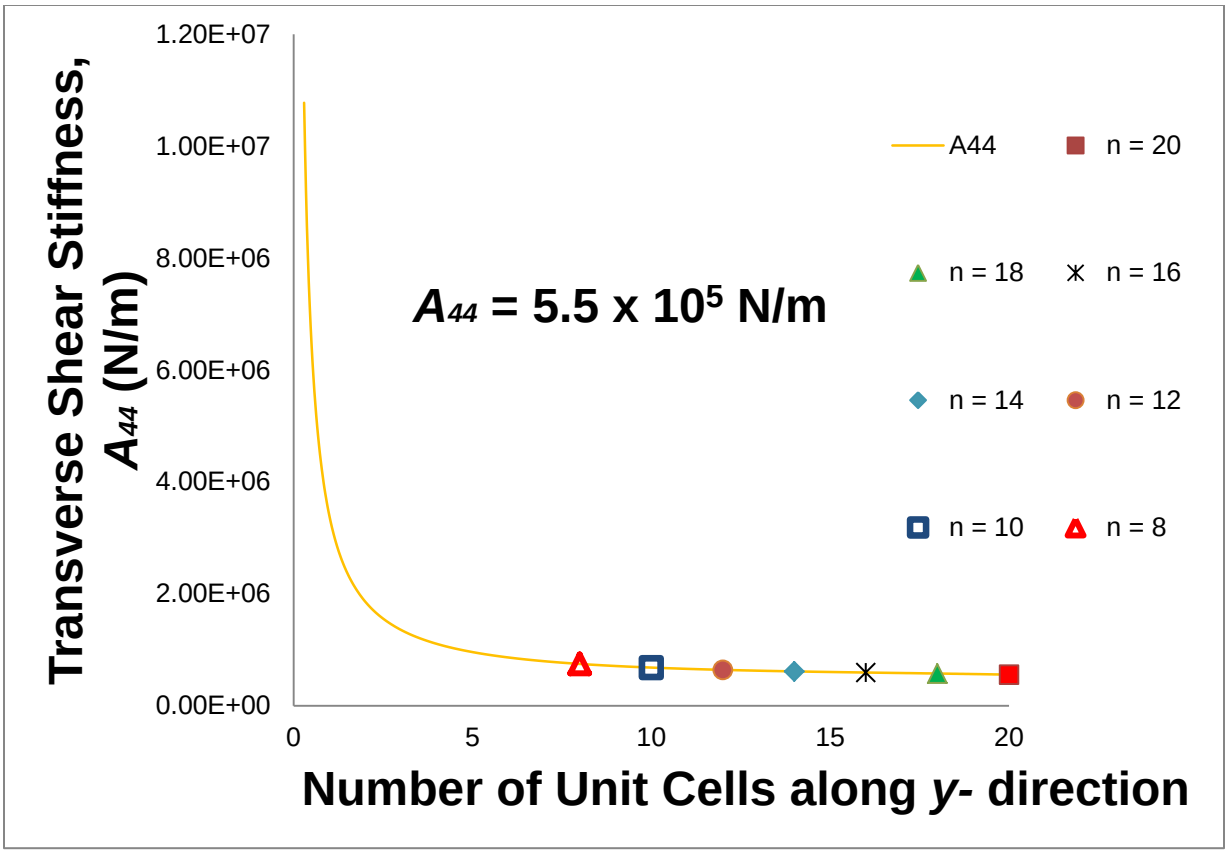

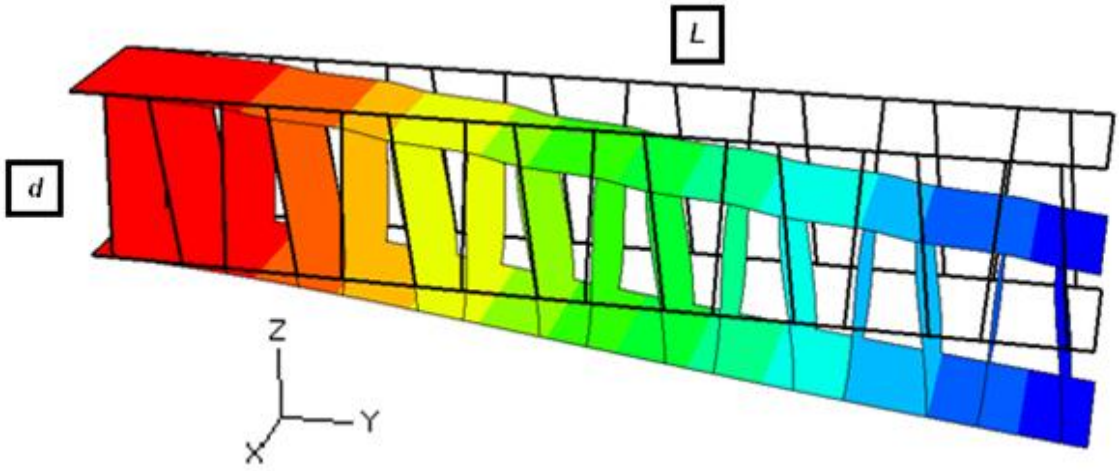

Figure 2-16. Top figure shows the prediction of transverse shear stiffness A_{44} as a function of the length of the beam and the bottom figure shows the deformed 3D FE model used for calculating A_{44} when subjected to pressure load.

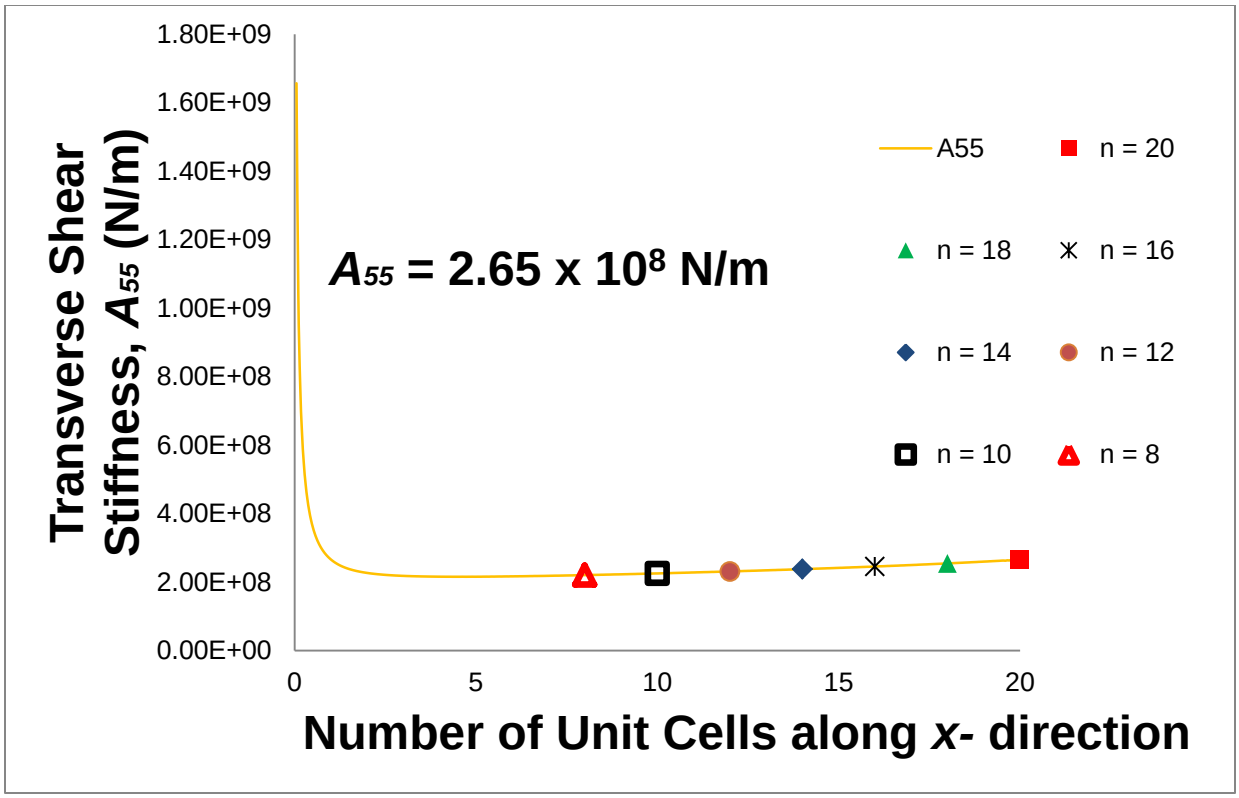

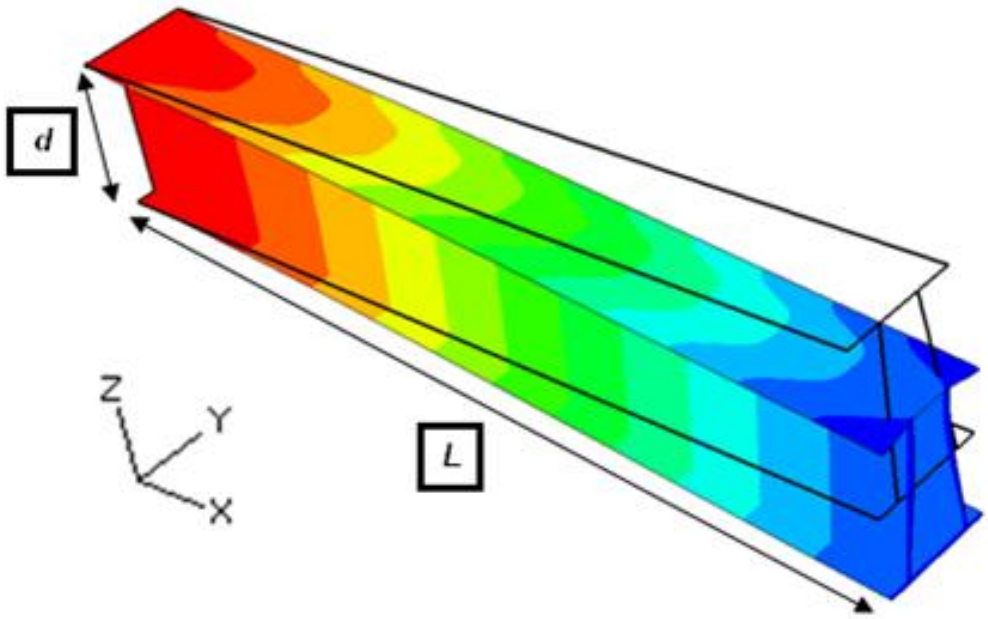

Figure 2-17. Top figure shows the prediction of transverse shear stiffness A_{55} as a function of the length of the beam and the bottom figure shows the deflected 3D FE model used for calculating A_{55} when subjected to pressure load.

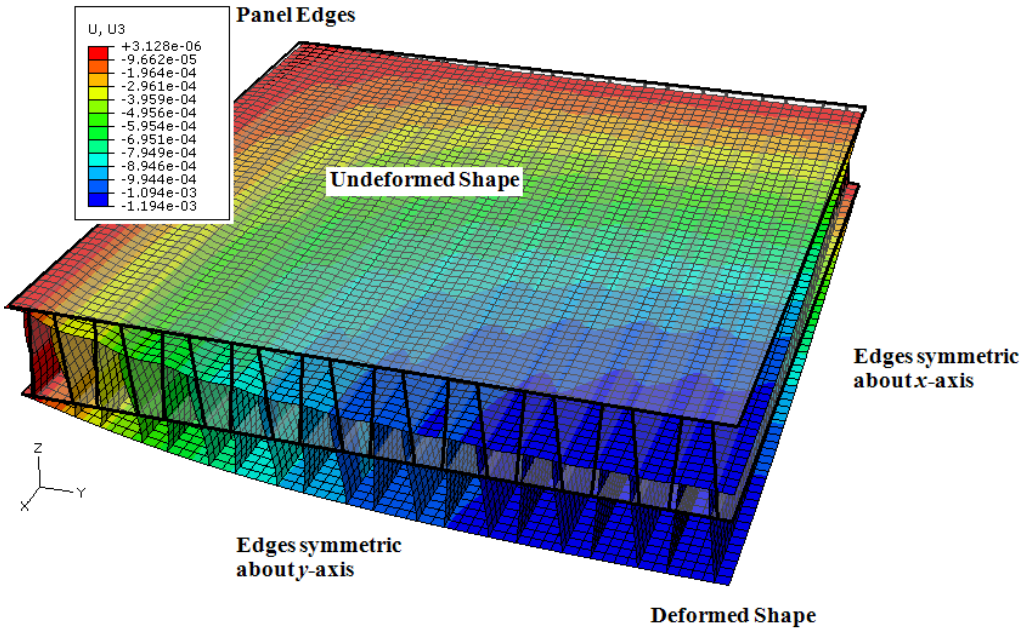

Figure 2-18. Undeformed and deformed shape of the 3D ITPS panel, when subjected to transverse pressure of 101 kPa.

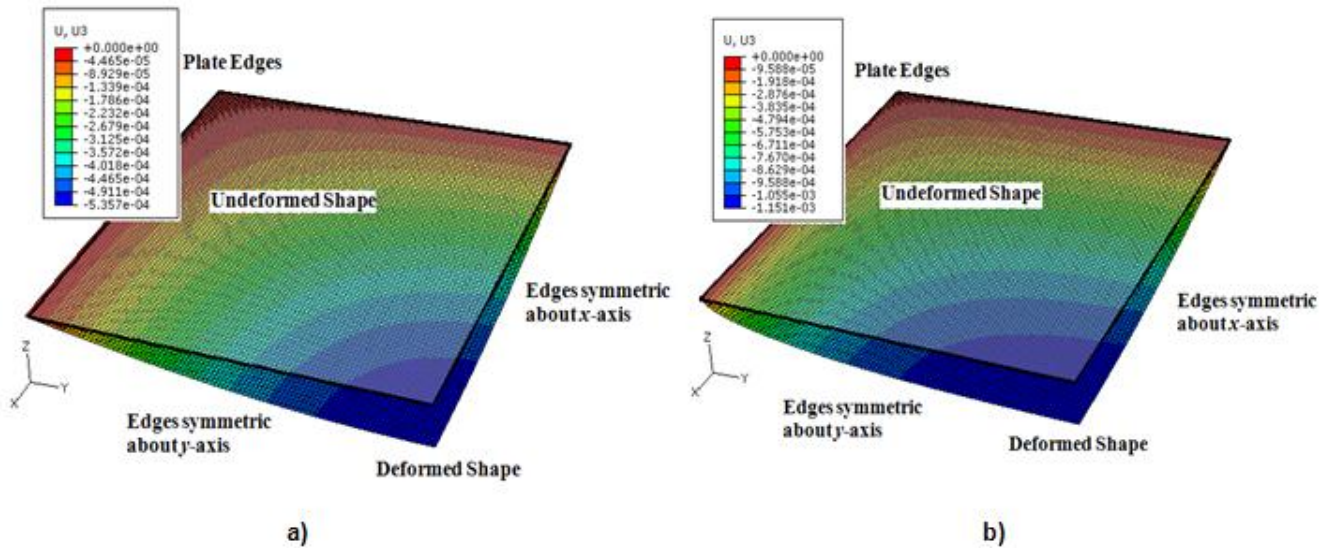

Figure 2-19. Undeformed and deformed shape of the 2D plate model, when subjected to transverse pressure of 101 kPa. (a) Modeled using classical laminate plate theory (Kirchoff plate) by assuming the transverse shear stiffness to be infinitely large (b) Modeled using shear-deformable elements by considering the transverse shear stiffness properties.

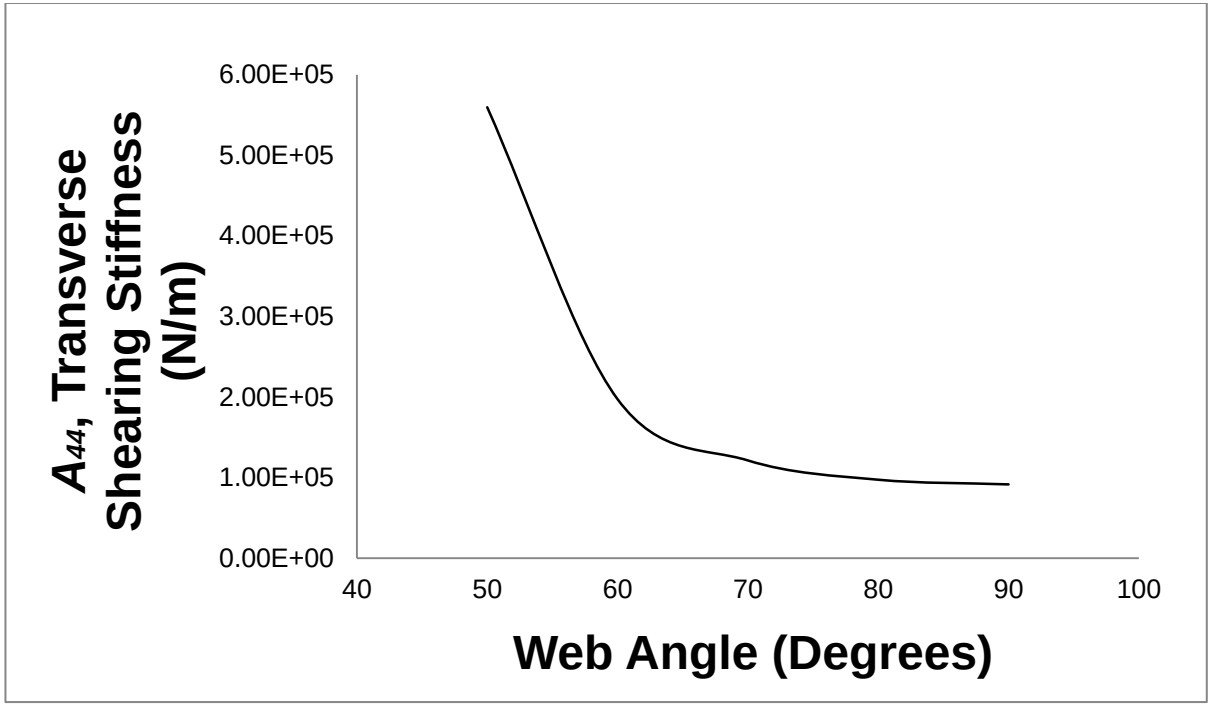

Triangular Webs (~40^{o}) have the maximum A_{44}, A_{44}= 4.89 x 10^{7} N/m

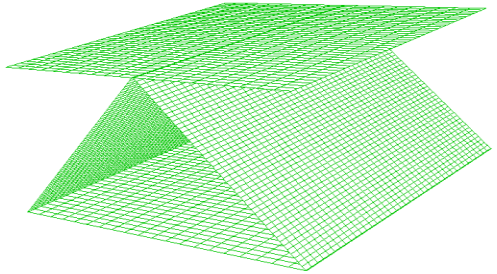

Figure 2-20. Variation for the transverse shear stiffness A_{44} with web angle.

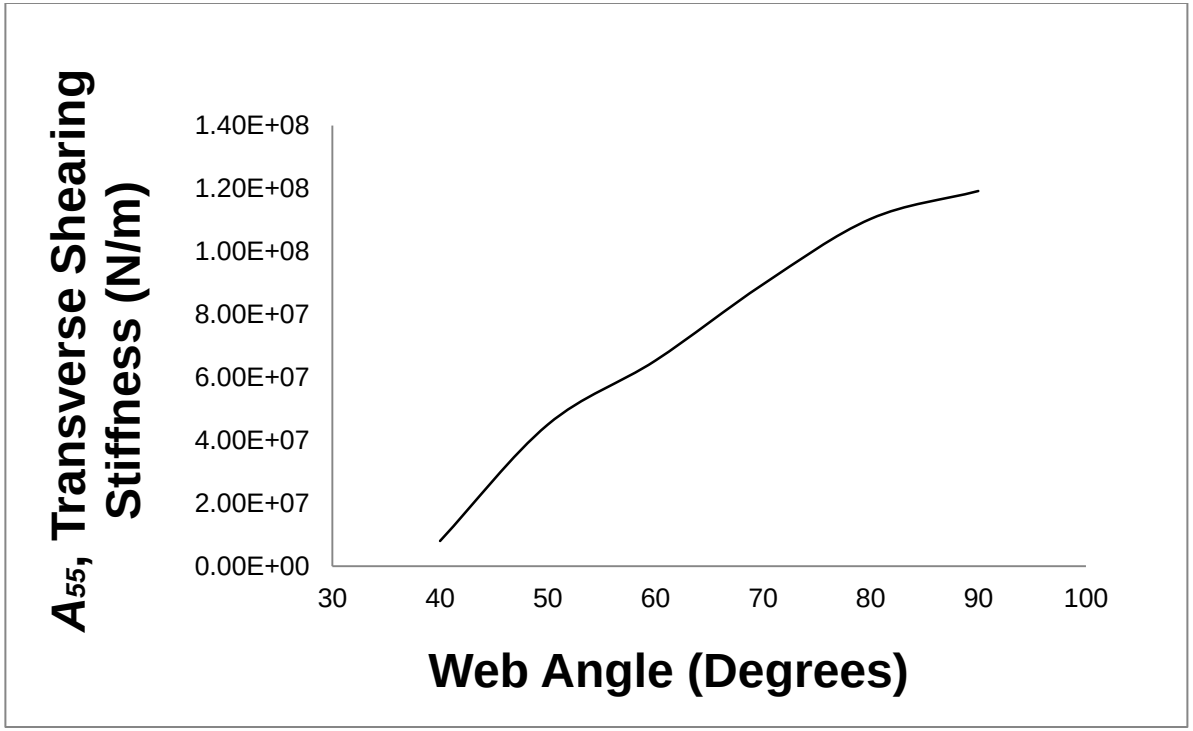

Rectangular Webs (90^{o}) have the maximum A_{55}, A_{55}= 1.2 x 10^{8} N/m

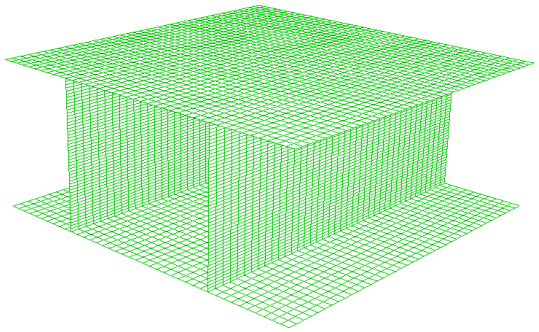

Figure 2-21. Variation for the transverse shear stiffness A_{55} with web angle.

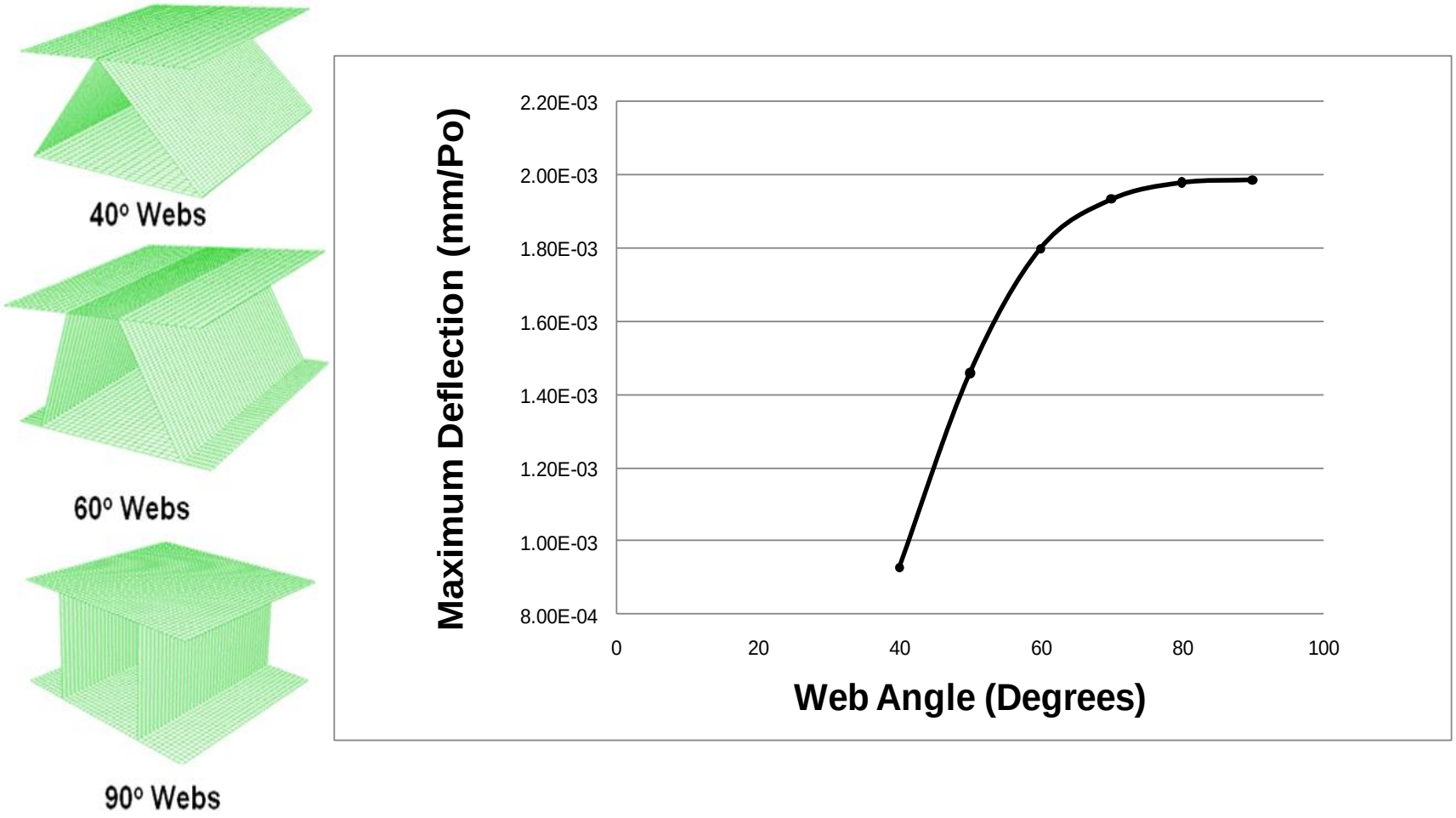

Figure 2-22. Variation of maximum deflection of TFS with web angle under transverse load.

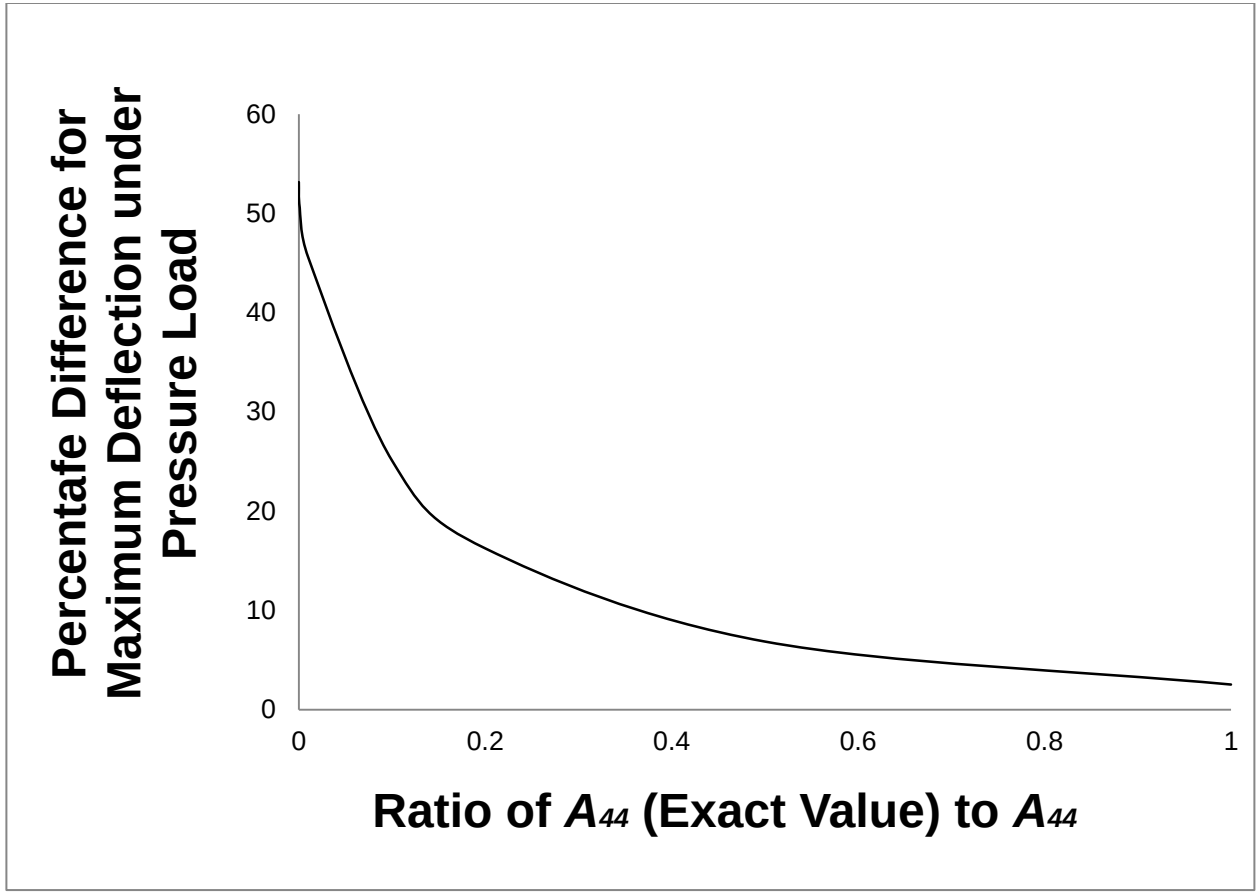

For Shear Deformable Plate Theory-A_{44} (Exact Value)/A_{44} = 1
For Classical Laminate Plate Theory-A_{44} (Exact Value)/A_{44} = 0

Figure 2-23. Percentage difference of maximum deflection of the TFS with the change in A_{44} under transverse load.

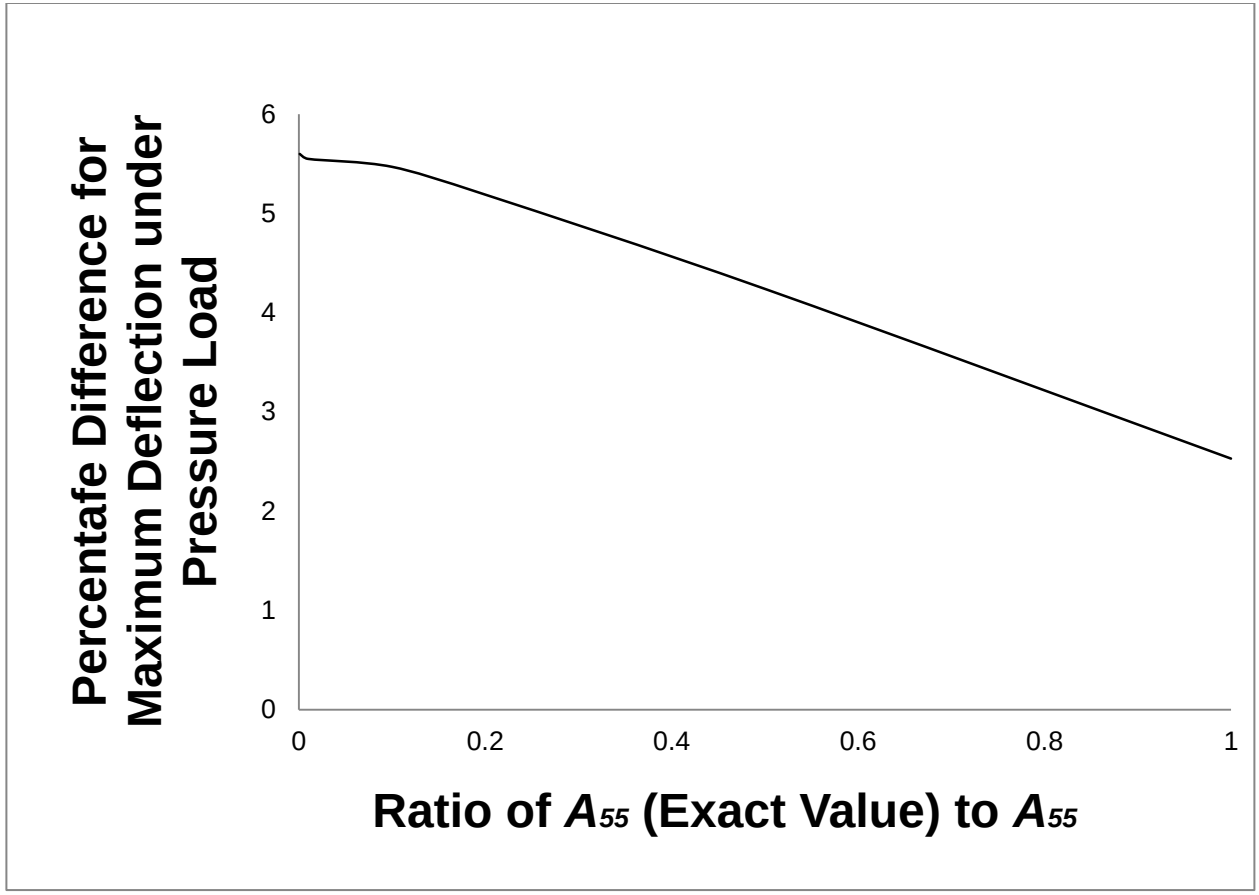

For Shear Deformable Plate Theory-A_{55} (Exact Value)/A_{55} = 1
For Classical Laminate Plate Theory-A_{55} (Exact Value)/A_{55} = 0

Figure 2-24. Percentage difference of maximum deflection of the TFS with the change in A_{55} under transverse load.

CHAPTER 3
STRESS AND BUCKLING ANALYSIS UNDER PRESSURE AND THERMAL LOADS ON AN INTEGRATED THERMAL PROTECTION SYSTEM PANEL

The ITPS is the outermost covering of the space vehicle. It is exposed to different types of environments during different phases of flight like ground debris strike, lightning strike, bird strike, rain/rain erosion, and on-orbit debris/micrometeoroid hypervelocity impact [10]. The ITPS should be able to withstand the aerodynamic heating loads to maintain the structure of the space vehicle within an acceptable temperature range. The hypersonic vehicle enters with a very high angle (40 degrees) of attack. It should be able to provide an acceptable aerodynamic surface to prevent premature transition to turbulence due to this surface heating and maintain acceptable performance. It is also exposed to pressure load from the transverse aerodynamic pressure or pressurized crew compartment, which tend to push the ITPS panel off the vehicle or into the vehicle, bending the outer surface and loading attachments and support hardware [9]. These pressures vary with time and location on the vehicle.

If three dimensional finite element methods were used to determine the response of a sandwich structure, the number of nodes and elements needed to properly model the structure can be excessive; as a result a full 3-D finite element analysis is not economical to conduct a preliminary analysis. Such panels may also be represented as a plate that is continuous, orthotropic, and homogenous, for which analytical [69] solutions are available. The analytical model resulted in a reasonably good estimate of stiffness properties - *A*, *B* and *D* matrices; however, the stresses in the web and face sheets differed significantly as the homogenized plate could not faithfully represent the local behavior of the ITPS. There was considerable difference between the analytical 2D and 3D models with widely varying geometries and material properties and hence it

was difficult to implement them in the design optimization environment. Hence, a finite element method based homogenization and reverse homogenization procedure is developed for calculating the deflections and stresses in the web and face sheets when subjected to pressure and thermal loads.

The extensional stiffness matrix [*A*], coupling stiffness matrix [*B*], bending stiffness [*D*], and the transverse shear stiffness terms A_{44} and A_{55} are calculated using finite element by using periodic boundary condition as mentioned in Chapter 2. These equivalent stiffness properties are then inputted to the plate finite element model for the two-dimensional homogenized plate analysis under pressure and thermal loads. After performing the plate analysis under pressure and thermal loading, the plate deformations (strains and curvatures) were then reapplied applied to the unit-cell by the process of reverse homogenization in order to obtain the detailed displacements and stresses in the face sheets and the web of the ITPS. The results were then compared with that from the 3D analysis of the ITPS. The entire homogenization and reverse homogenization are shown in the flowchart in Figure 3-2. The FE based homogenization and reverse was found to be more robust and could be performed with any commercially available FE programs. The FE based homogenization and analysis of the 2D plate is less expensive as compared to that of 3D.

As mentioned before, there are two important types of loads that need to be considered in the design optimization of an ITPS. Both occur during the reentry phase of the space vehicle. The two load cases are: (a) aerodynamic pressure acting on the top face sheet; and (b) thermal stresses due to severe temperature gradient across the thickness of the ITPS. These loads could cause the ITPS panel to fail by buckling,

and/or yielding. Knowing the panel behavior and failure modes when exposed to different loading environments is important in the design because excessive deflection of the panel leads to extremely high local aerodynamic heating or high stresses leads to undesirable yielding and critical buckling. Therefore, the analysis of these two load cases using the method of homogenization and reverse homogenization are described in the following sections:

Uniform Pressure Loading Analysis

Aerodynamic pressure load during reentry for a space shuttle-like design is shown in Figure 3-3. During reentry the pressure load on the outer surface of the vehicle is considered to be zero. But after landing, the external pressure becomes equal to the atmospheric pressure (Figure 3-3). TPS separates the crew compartment from the outer shell. The crew compartment is under pressure apposite to human comfort. The space between the crew compartment and the outer shell is assumed to be vented to the outer atmosphere. Just prior to reentry, this vented space would be at zero pressure. During reentry phase the pressure load on both sides of TPS is zero and hence there is no pressure load applied on the ITPS panels during reentry phase. After the vehicle lands, the outside pressure is equal to the atmospheric pressure. Even though the space between crew compartment and the TPS is vented to the atmosphere, there will be a certain lag time before the pressure on both sides of the TPS becomes equal. During this lag time, there is a pressure load on the outer surface. We will consider the worst case scenario, where the pressure load on the outer surface is considered equal to 1 atmosphere or 101,325 Pa. This pressure value is typical for the maximum pressure to which the ITPS could be subjected to [67].

The ITPS panel is subjected to a pressure loading of 101 kPa on its TFS in the 3D model (Figure 3-4). Similarly, a pressure of 101 kPa is applied to the homogenized plate (Figure 3-5). The deflection can be obtained from the 2D plate analysis. In order to recover the actual stresses in the TFS, BFS and the webs, reverse homogenization is performed as mentioned in the following section.

Stresses due to Pressure Load using Reverse Homogenization

The plate responses will be in terms of force and moment resultants. The uniform pressure that acts on the 2D plate results in curvatures and in-plane strains at a given (x, y) point on the 2D plate. An ITPS unit cell is assumed to be at each x and y location of the homogenized 2D plate. The FE analysis of the unit cell is performed by applying the corresponding curvatures and in-plane strains in order to obtain the stresses on the TFS, BFS and the webs. This reverse homogenization procedure (Figure 3-6) is repeated at various points on the plate and then the maximum von Mises stress is obtained for the TFS, BFS and the webs, respectively, and is compared to that obtained from 3D analysis (Figure 3-7).

Local Deflection and Stresses in the Top Face Sheet

When the ITPS panel is subjected to pressure loading, there is a local effect on the TFS in addition to the global response. The uniform pressure loading that acts on the thin top face sheet results in local deflections and local stresses which are not captured by the 2D plate model. A unit cell analysis is performed (Figure 3-8) wherein all deformations, ε_0 and κ, are constrained by applying appropriate periodic boundary conditions, and the pressure loading is applied on the top face sheet. The top face sheet stresses and deflections obtained in this step are added to the stresses due to the

plate deformations. This procedure is repeated at different points on the plate to determine the von Mises stresses and deflections in the TFS.

Thermal Loading Analysis

The ITPS panel is subjected to severe thermal environments. Therefore, a heat transfer analysis needs to be performed in order to determine the temperature distribution in the panel. Pressure, conduction, radiation, convection, and temperature variation all play important roles in the thermal performance of an ITPS [9]. Incident heat flux on the vehicle depends on the shape of the vehicle, and the trajectories of the ascent and reentry. In this study incident heat flux during reentry of a Space Shuttle-like vehicle is used (Figure 3-9).

One-dimensional (1-D) FE heat transfer analysis is performed using DC1D3 diffusive heat transfer 3-node link elements. The elements are oriented in the z-direction. Typically, simplified one-dimensional models (Dorsey and Poteet [10]) are used to predict the thermal performance of a thermal protection system. Such a simplified approach was earlier justified by comparing the results obtained from a 1-D and a 2-D heat transfer analyses by Bapanapalli [20,67]. The panel's core and webs were modeled as a thermally homogenous equivalent material with its properties being determined through the rule of mixtures [67]. Copenhaver et al [68] developed a 1-D conductive / radiative finite element model which describes heat transfer through the thickness of the honeycomb structure for the *Ti-6AI-4V* alloy interior with aluminum-boron composite face sheets. Based on this model, they estimated the thermal capacitance of the face sheet and the emissivity in the interior of the core.

Heat flux is incident on the top surface of the top face sheet. A large portion of this heat is radiated out to the ambient by the top surface. The remaining heat is conducted

into the ITPS. Also the bottom surface of the bottom face sheet is assumed to be perfectly insulated. This is the worst case scenario where the bottom face sheet temperature would rise to a maximum as it cannot dissipate the heat. It is also assumed that there is no lateral heat flow out of the unit cell; that is, the heat flux incident on a unit cell is completely absorbed by that unit cell only. Similar model and boundary conditions were chosen by Bapanapalli et al [20]. It was found that the stresses in the ITPS panel are maximum when the average temperature gradient through the panel thickness is at its severest and is the major driver of thermal stresses (Figure 3-10).

In Martinez et al [21, 69], a micromechanical method is developed analytically to calculate the equivalent thermal forces and moments for a given temperature distribution. The method was demonstrated by calculating stresses in a sandwich panel subjected to a temperature distribution described by a quartic polynomial in the thickness direction. The results for stresses are compared with that from a three-dimensional finite element analysis. As mentioned earlier, the analytical method has limitations and hence we chose the finite element based homogenization method in the present study.

Thermal force and moments are caused in the ITPS panel when there is through-the-thickness temperature gradient. The thermo-elastic laminate constitutive relations are given as,

$$\begin{Bmatrix} N \\ M \end{Bmatrix} = [K] \begin{Bmatrix} \varepsilon_o \\ \kappa \end{Bmatrix} - \begin{Bmatrix} N^T \\ M^T \end{Bmatrix} \tag{3-1}$$

In Equation 3-1, N^T and M^T are the unit cell's thermal force and moment resultants and moment due to temperature variation through the thickness of the ITPS. The thermal

force resultants and moments are equal to the negative of forces and moments that act on the unit cell when it is completely constrained at its lateral boundary surfaces.

The thermal analysis is broken into two parts. First, the unit cell is constrained to prevent lateral deformations using periodic boundary conditions and then the through the thickness temperature distribution is applied to the unit cell (Figure 3-11). The temperature distribution equation was determined by fitting a quartic polynomial to the actual temperature distribution. From the stresses in the unit cell the thermal forces (N^T) and thermal moments (M^T) are computed (Part i). The nodal forces of the boundary nodes were determined from the finite element analyses. The force and moment resultants acting on the unit cell were obtained from the nodal forces using Equation 3-2.

$$\begin{aligned}\left[N_x, M_x\right] &= \frac{1}{b}\sum_{m=1}^{tn}\left[1, z\right]F_x^{(m)}(a, y, z) \;\rightarrow\; \text{For the face } x = a \\ \left[N_y, M_y\right] &= \frac{1}{a}\sum_{m=1}^{tn}\left[1, z\right]F_y^{(m)}(x, b, z) \;\rightarrow\; \text{For the face } y = b\end{aligned} \tag{3-2}$$

where $F_x^{(m)}$ and $F_y^{(m)}$ are the nodal forces in the *x* and *y* directions at the m^{th} node and '*tn*' is the total number of nodes on the face. The resultants obtained are the forces needed to constrain the unit cell during a change in temperature, and they will be equal to the negative of the thermal forces of the ITPS as can be seen from the thermo-elastic laminate constitutive relation.

$$\begin{aligned}\begin{Bmatrix} N \\ M \end{Bmatrix} &= \left[K\right]\begin{Bmatrix} \varepsilon_o \\ \kappa \end{Bmatrix} - \begin{Bmatrix} N^T \\ M^T \end{Bmatrix} \\ \begin{Bmatrix} N^T \\ M^T \end{Bmatrix} &= -\begin{Bmatrix} N \\ M \end{Bmatrix}\end{aligned} \tag{3-3}$$

Next, the panel is modeled as an equivalent orthotropic plate with the stiffness properties given by the ABD matrices and transverse shear stiffness coefficients. The thermal force and moment from (Part i) are reversed and applied along the boundaries of the plate (Figure 3-12). The plate responses will be in terms of force and moment resultants. In order to recover the actual stresses, an ITPS unit cell is assumed to be at each *x* and *y* location of the homogenized 2D plate. The FE analysis of the unit cell is performed by applying the corresponding curvatures and in-plane strains in order to obtain the stresses on the TFS, BFS and the webs (Figure 3-13). This reverse homogenization procedure is repeated at various points on the plate and the stresses are obtained for the TFS, BFS and the webs, respectively (Part ii). The total stress at any given unit cell in the panel is obtained by adding the stresses obtained in (Part i) and (Part ii). From these stresses von Mises stress in the TFS, BFS and web are calculated. Comparison of the von Mises's stress from the 2D analysis is compared to that from the 3D analysis is presented in the results section, and the agreement seems to be reasonable.

Sub Structuring

Another approach to recover the actual stresses from the 2D plate analysis is by using the method of sub structuring. The 2D plate model gives results in terms of mid-plane displacements $u_0(x,y)$, $v_0(x,y)$ and $w_0(x,y)$, and rotations $\psi_x(x,y)$ and $\psi_y(x,y)$. The 3D displacements $(u(x,y,z), v(x,y,z)$ and $w(x,y,z))$ at various points on the ITPS can be obtained from the results of the 2D plate mid plane displacements and rotations. These 3D displacements can be applied to the unit cell at various points and by this process we can recover the actual stresses in the TFS, BFS and the web. While this process is

time consuming, doing sub structuring by applying displacements at all the nodes for the entire unit cells will take a lot more time than the reverse homogenization. The following equations are used to obtain the 3D displacements at any arbitrary point in the ITPS from the plate displacements.

$$\begin{aligned} u(x,y,z) &= u_0(x,y) + z\psi_x(x,y) \\ v(x,y,z) &= v_0(x,y) + z\psi_y(x,y) \\ w(x,y,z) &= w_0(x,y) \end{aligned} \tag{3-4}$$

The displacements obtained from the 2D plate analysis (Equation 3-4) are compared with the 3D ITPS displacements in the result section and it was found that it matches really well for the given material combination and loading conditions.

Buckling of an ITPS

The ITPS is made of thin face sheets and webs, making them susceptible to buckling when subjected to pressure and thermal loads. The thermal and pressure loads initiate compressive forces at each of the component on the ITPS. Decreasing the thickness of the webs helps to reduce the mass of the ITPS. The thermal protection requirements dictate that the webs are longer and thinner so that less heat is conducted to the BFS. However, this would weaken the structural link between top and bottom face sheets. Large transverse aerodynamic pressure loads on the top face sheet and severe temperature gradient through the panel thickness could cause the webs to buckle.

3D finite element is the preferred choice for buckling analysis where it is modeled as an eigenvalue buckling prediction. It was used to estimate the critical (bifurcation) load for the structure. Two types of buckling analysis were done, one for the temperature loads and one for the aerodynamic pressure loads.

For thermal buckling analysis, temperature loads were obtained in the form of through thickness temperature distributions from the heat transfer problem. The temperature distributions are cubic polynomials in *z*. Using these polynomials, temperature was imposed on each node of the 3-D buckling model. This implies that the top and bottom face sheet temperatures are uniform throughout the length and width of the panel. Several 3D thermal buckling analyses were attempted initially and it was found that every time the corner most webs near the panel edges buckles (Figure 3-14). Therefore, it was decided to apply sub structuring to the region near the corners using Equation 3-2. The 3D displacements along the panel boundary of one unit cell length are obtained from the plate displacements when the plate is subjected to thermal force and moment resultants. These displacements are applied on to the unit cell and the temperature distribution is applied on each node of the unit cell obtained from the heat transfer and a unit cell buckling analysis is done (Figure 3-15). The unit cell thermal buckling analysis is then compared with the entire 3D ITPS thermal buckling analysis results.

For pressure buckling analysis, aerodynamic pressure load is applied on the TFS. Again, several 3D pressure buckling analyses were carried out initially and it was found that every time a different web buckles as shown from Figure 3-16. Since sub structuring will not be used in such cases, it was decided to use full 3D eigen value buckling analysis.

Results

For verification of the effectiveness of the deflections and stress results under the action of uniform pressure loading and thermal loading for the FE based homogenization method, consider a corrugated-core sandwich panel unit cell with the

following dimensions: p = 25 mm, d = 70 mm, t_{TF} = 1.2 mm, t_{BF} = 7.49 mm, t_w = 1.63 mm, θ = 85^o. For the 3D FE analysis the 3D panel is assumed to consist of 20 unit cells. In the following example, the TFS and the web is modeled using Titanium alloy, Ti-6Al-4V (E_1 = 109 GPa and ν = 0.3) and the BFS is modeled using Beryllium alloy (E_1 = 290 GPa and and ν = 0.063) [20].

For the 3D panel, only one fourth of the ITPS panel containing half the total number of unit cells is modeled using the ABAQUS® finite element (FE) software (Figure 3-17). The model uses approximately a total of 140,000 eight-node shell elements (S8R). The boundary conditions considered are: fixed vertical displacements for the bottom face sheet (BFS) (w = 0) and fixed rotations for the top face sheet (TFS) ($\theta_x = \theta_y = 0$) on the edges of the panel. On the symmetric edges, symmetric boundary conditions are used. Similar boundary conditions and modeling procedures are also referred in Bapanapalli et al [20].

The plate is also modeled using shell elements in ABAQUS® finite element (FE) software. The model used a total of 33,000 eight-node shell elements (S8R). A simply supported boundary condition is considered along the boundary of the plate (w = 0) (Figure 3-18). The plate edges are allowed to move in the horizontal plane. Due to symmetry only one-fourth of the panel is modeled.

ITPS Out-of-Plane Displacement, Uniform Pressure Load

The 3D ITPS panel was subjected to a uniform pressure loading of 101,325 Pa on the top face sheet. Similarly, the pressure load is also applied to the homogenized plate model. Also, the corresponding ABD matrices and the transverse shear stiffness properties, A_{44} and A_{55}, is input into the homogenized plate model. The plate out-of-plane displacements compared well to the 3D BFS out-of-plane displacements.

However, the TFS undergoes local deflection which is not captured by the 2D plate model as mentioned before. The BFS will not undergo local deflections, as it is separated from the TFS by the web, hence the effect of pressure on the TFS will not be there. Therefore a unit cell analysis is performed along with the plate analysis in order to capture the wavy nature of the thin top face sheet deflections. The 3D FEM out of plane displacements of the ITPS at $x = a/2$ and $y = b/2$, were extracted and compared with the results obtained from the 2D plate model as mentioned before and they agree well (Figure 3-19 and Figure 3-20). There was greater percentage difference near the boundary of the ITPS because different boundary conditions were used for the 2D plate model and the 3D ITPS model. At the center of the ITPS plate the structure acted more like the homogenized 2D plate because it was farther away from the boundary. The superposition of the displacement results obtained from the 2D plate method and the unit cell analysis resulted in a less than 5% difference and an accurate representation of the top face sheet deflection response when subjected to a uniform pressure load. The bottom face sheet FE displacement results agreed well with the displacement results obtained from the homogenized plate model. The bottom face sheet deflection acted more like a 2D plate because of the absence of local effects from the uniform pressure loading (Figure 3-19 and Figure 3-20).

ITPS Local Stress due to Pressure Load

The stresses from the 3D ITPS are compared to the 2D plate homogenized and reverse homogenized model when it is subjected to a pressure load of 101,325 Pa. The FEM von Mises local stresses were extracted from the FEM output after analysis at $x = a/2$ and $y = b/2$. The top face sheet stresses were computed by superimposing the stress results from the plate deformations to the constrained unit cell analysis, as

explained in Section-Local Deflection and Stresses in the Top Face Sheet (Page 89). The bottom face sheet stresses are obtained only from the plate deformations. The comparison of the stresses obtained from the 2D plate model and the 3D model is shown in Figure 3-21 and Figure 3-22. The percentage difference was less than 2% for stress results near the center the ITPS plate. However, near the boundary the percentage difference was higher but this was the best that could be captured from the 2D plate model and the remaining difference could be recovered through an algebraic surrogate's correction which will be discussed in Chapter 4.

ITPS Local Stress due to Thermal Load

As mentioned before, the thermal load was obtained from the one-dimensional finite element heat transfer analysis. The heat transfer determines the maximum bottom face sheet temperature of the unit cell and the core temperature distribution at any particular re-entry time. The re-entry time that was considered for the thermal analysis corresponds to the time when the thermal gradient was maximum because it yielded the worst stress results. The stresses from the 3D ITPS are compared to the 2D plate model. The von Mises local stresses were extracted from the FEM output after analysis at $x = a/2$ and $x = b/2$. The procedures for obtaining thermal stresses from the 2D plate model are similar to that explained in Section-Thermal Loading Analysis (Page 90). The comparison of the stresses obtained from the 2D plate model and the 3D model is shown in Figure 3-23 and Figure 3-24. As seen from the graph, the difference was more near the boundaries. The results between the 3D finite element analysis and the 2D finite element for the constrained and unconstrained thermal problem were within 5% of each other for stress results near the center of the ITPS plate.

Displacements from Plate Deformations

Once the 2D plate analysis is done, the plate mid-plane displacements u_0 *(x,y)*, v_0*(x,y)* and w_0*(x,y)*, and rotations $\psi_x(x, y)$ and $\psi_y(x, y)$ can be used to obtain the 3D displacements *(u(x,y,z)*,*v(x,y,z)* and *w(x,y,z))* at various points on the ITPS. These displacements compares well with the corresponding 3D ITPS displacements. The comparison is shown in Figure 3-26 and Figure 3-27 for the pressure loading case and Figure 3-28 and Figure 3-29 for the thermal loading case.

Also we know that for the thermal buckling analysis, only webs adjacent to the panel edges always buckle (Figure 3-14). Therefore, we obtain displacements from the plate deformations for the corner most unit cell and apply these displacements on to the unit cell boundaries along with the temperature distribution on each node of the unit cell and perform unit cell buckling analysis (Figure 3-15). We compare the minimum eigen value obtained from the unit cell buckling analysis with the 3D ITPS buckling eigen value analysis. Various designs were compared between the unit cell buckling eigen value analysis and the 3D ITPS buckling eigen value analysis and the maximum percentage difference was approximately 6-10%. Table 3-1 shows the comparisons for three such designs. The unit cell buckling analysis takes 1-2 minutes to do the analysis whereas the 3D ITPS buckling analysis takes at least 1 hour 15 minutes. We gain a large improvement in time with slight reduction in the accuracy, which can be further improved by using corrections such as algebraic surrogates as discussed in Chapter 4.

Concluding Remarks

A plate solution using homogenization and reverse homogenization method was established for determining the out of plane displacements and von Mises stresses

under thermal and pressure loads. The plate out of plane displacement results are within 5% difference from the 3D FEM results for the pressure loading case. However, the percentage difference of the von Mises stress between the 3D analysis and the 2D analysis was higher and was greater at the boundary of the ITPS panel for both the pressure and thermal loading case. The majority of stresses at points away from the boundaries can be approximated well by the 2D plate analysis. Further for the pressure loading case, the BFS acts more like a 2D plate as there was no local effect of pressure load as it was being applied on the TFS. We also compared the buckling unit cell eigen value analysis with the 3D ITPS buckling analysis under thermal loads and the maximum percentage difference was found to be approximately between 6-10%. Unit cell buckling analysis is not possible for the case of pressure load because for different designs, different webs buckle.

Though there were differences between the 2D plate analysis and 3D ITPS analysis in the prediction of stresses and deflections, this difficulty will be resolved by fitting the low-fidelity 2D finite element model with high quality surrogate, which will then be corrected by the use of a small number of high fidelity 3D finite element analyses. This approach is known as multi-fidelity or variable-complexity modeling, allows the use of fewer analysis of the 3D high fidelity, for a given accuracy. This multi-fidelity response surface technique will be used in our design optimization and is explained in detail in Chapter 4.

Table 3-1. Percentage difference for buckling eigen value analysis under thermal load.

	3D	2D	Percentage Difference
Design 1	1.024	1.087	6
Design 2	2.17	2.0	8.5
Design 3	1.34	1.42	5.7

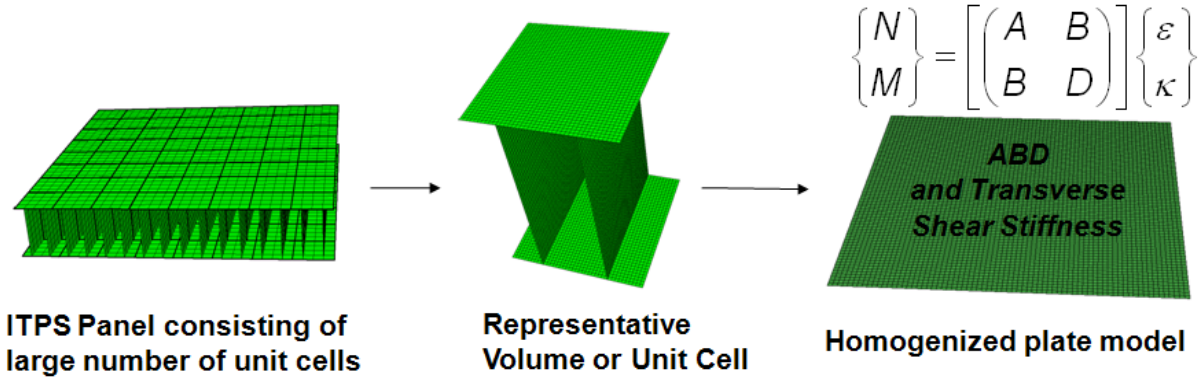

Figure 3-1. Representation of the ITPS panel as a homogenized plate with equivalent stiffness properties.

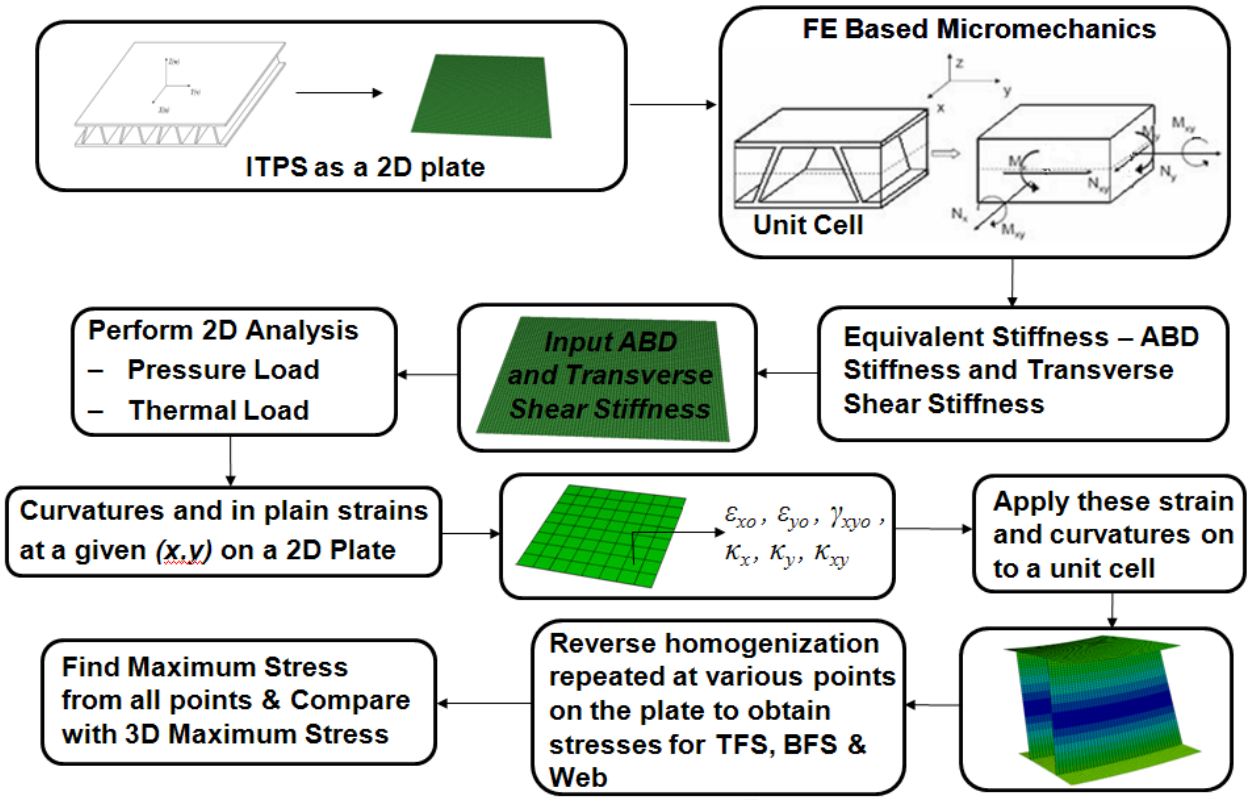

Figure 3-2. Flowchart describing the homogenization and reverse homogenization method.

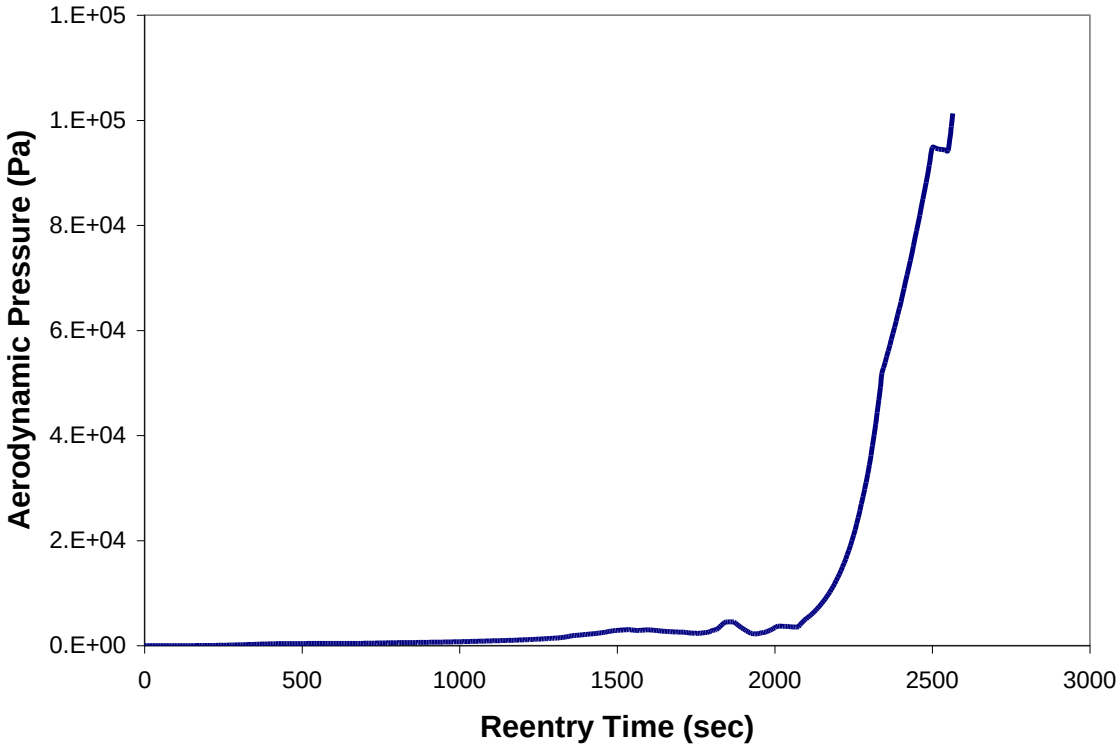

Figure 3-3. Aerodynamic pressure load on the TPS for a Space Shuttle-like design. During reentry, the pressure is approximately zero and after landing it becomes equal to the atmospheric pressure (Bapanapalli, S.K., Martinez, O., Gogu, C., Sankar, B.V., Haftka, R., "Analysis and Design of Corrugated-Core Sandwich Panels for Thermal Protection Systems of Space Vehicles", 47th AIAA/ASME/ASCE/AHS/ASC Structures, Structural Dynamics, and Materials Conference, Newport, RI, May 2006).

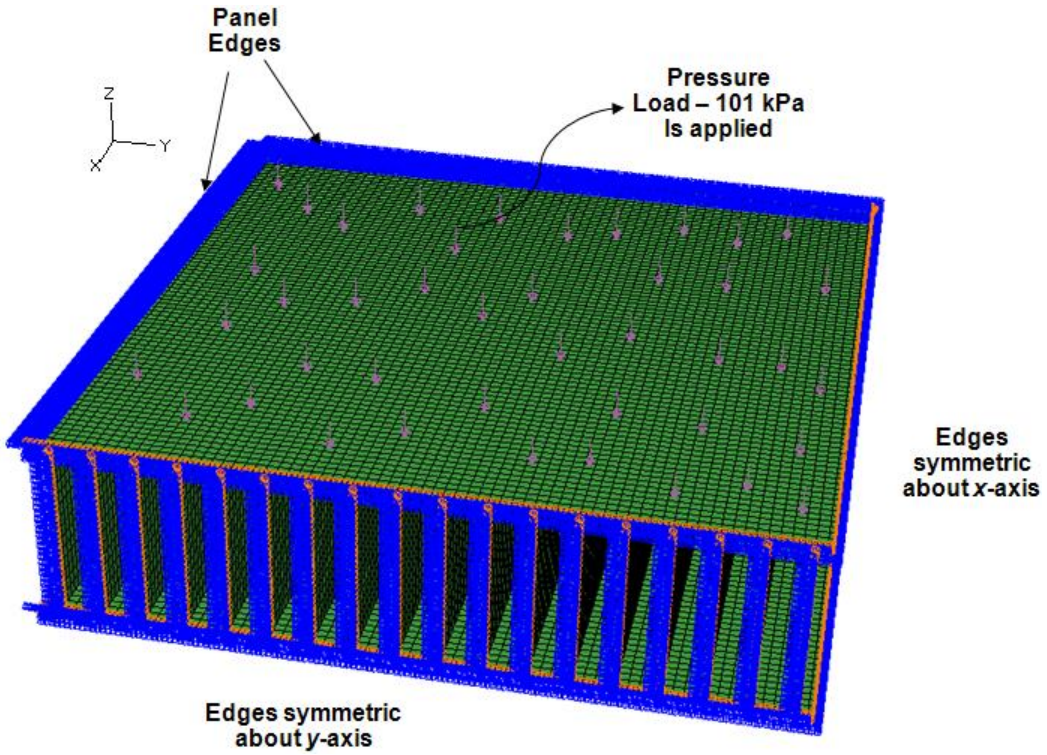

Figure 3-4. Typical mesh and boundary conditions for the high fidelity 3D finite element model of one fourth of the panel when subjected to pressure load of 101 kPa.

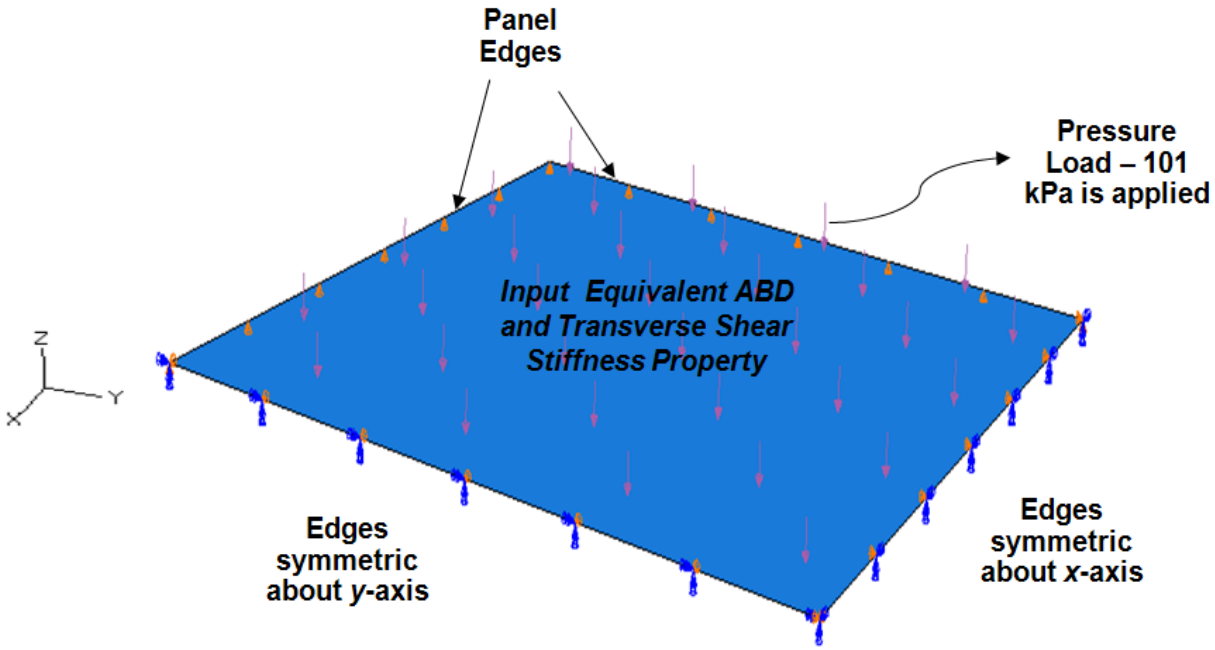

Figure 3-5. Typical boundary conditions for the low fidelity 2D plate model when subjected to pressure load of 101 kPa.

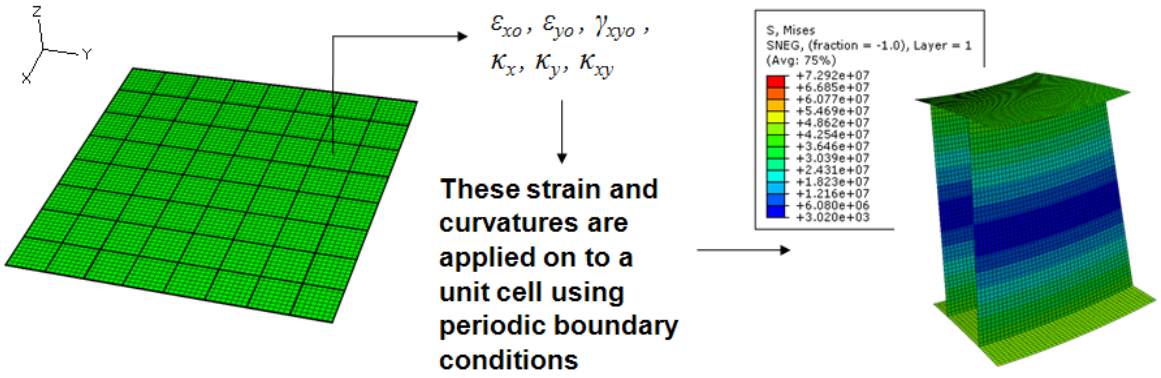

Figure 3-6. Reverse homogenization for a 2D plate.

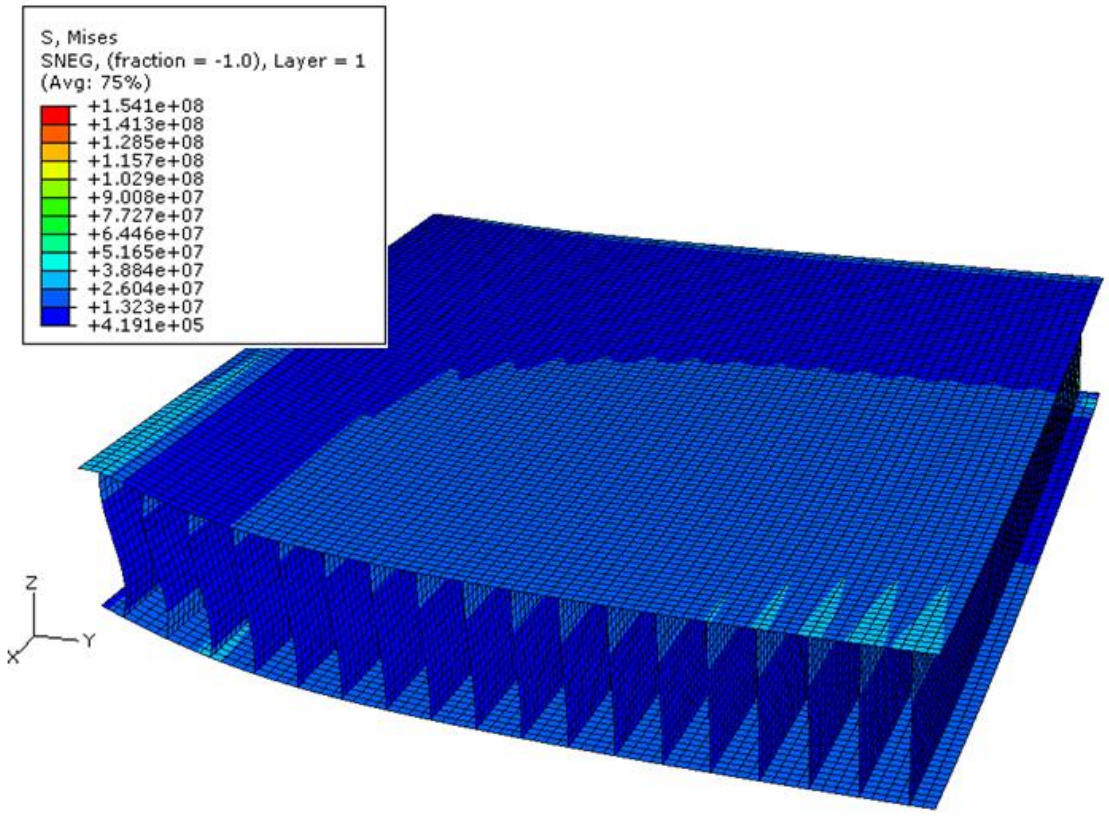

Figure 3-7. Contour of von Mises stresses in the ITPS due to pressure loading. The stresses are given in Pascal units.

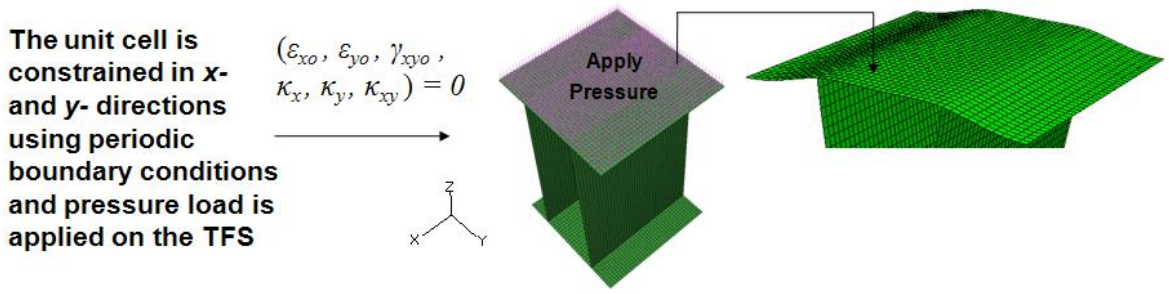

Figure 3-8. Local stresses and deflections of the TFS due to uniform pressure loading.

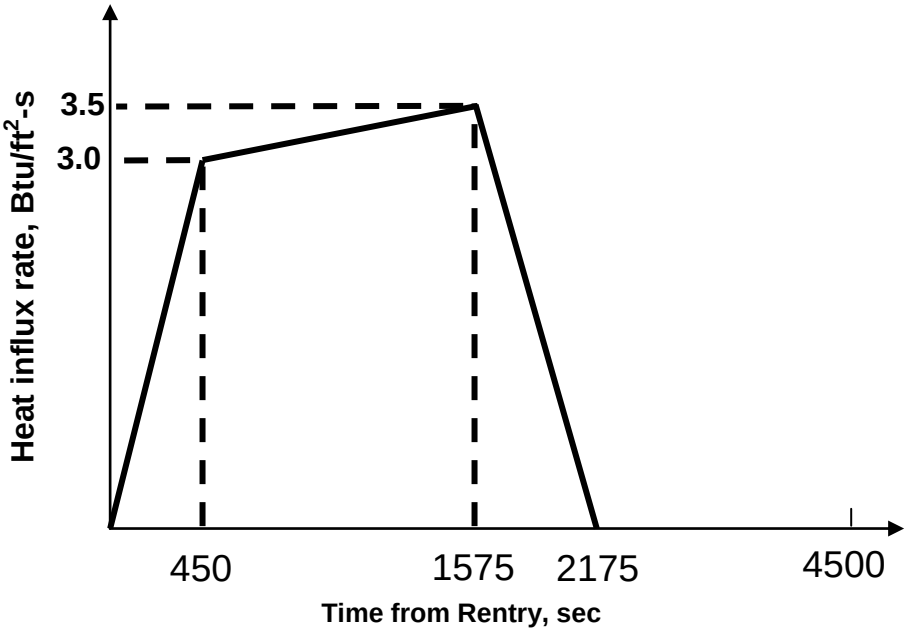

Figure 3.9. Approximate heating rate used for the analysis (Bapanapalli, S.K. (2007). Design of an integral thermal protection system for future space vehicles. Unpublished Ph.D. dissertation, University of Florida, Gainesville, FL).

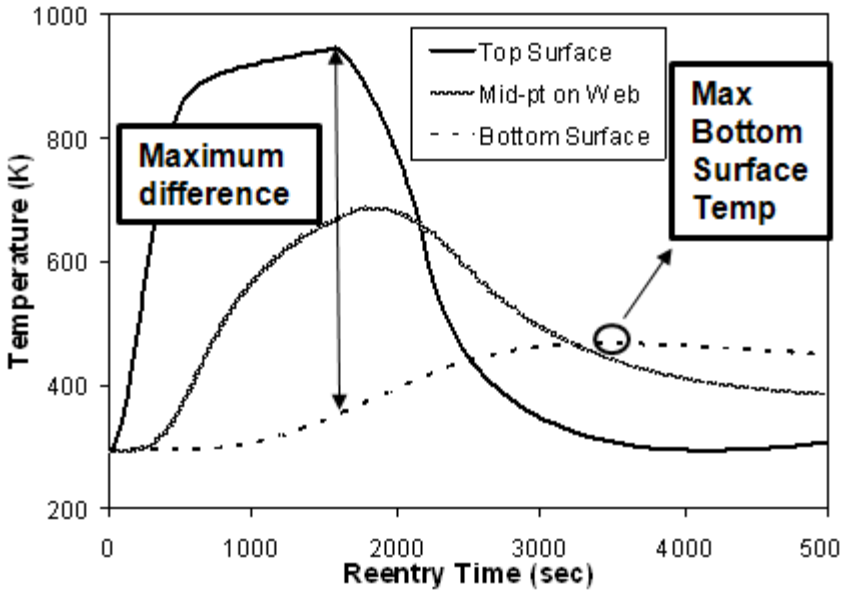

Figure 3-10. Variation of the temperature of the top face sheet, bottom face sheet and mid point in the web with respect to different reentry times (Bapanapalli, S.K. (2007). Design of an integral thermal protection system for future space vehicles. Unpublished Ph.D. dissertation, University of Florida, Gainesville, FL).

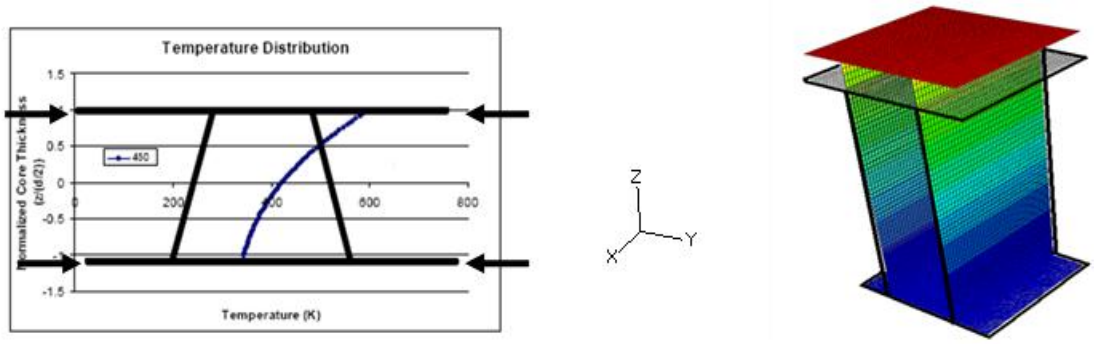

Figure 3-11. Constraining the unit cell to prevent displacements and strains in x and y directions using periodic boundary conditions.

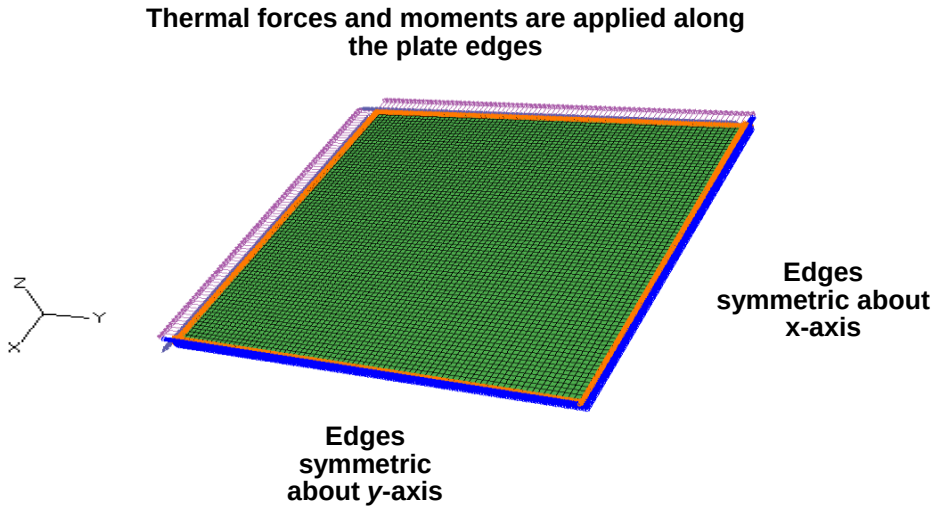

Figure 3-12. Thermal forces and moments resultants on to the 2D plate model.

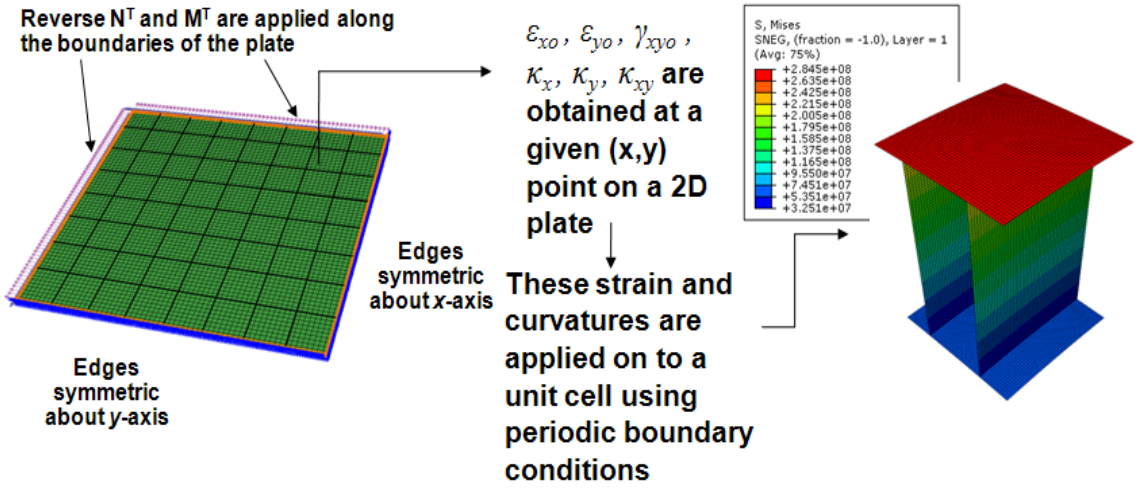

Figure 3-13. Reverse thermal forces and moments being applied to the 2D plate model in order to obtain the strain and curvatures. These plate deformations are applied to a unit cell.

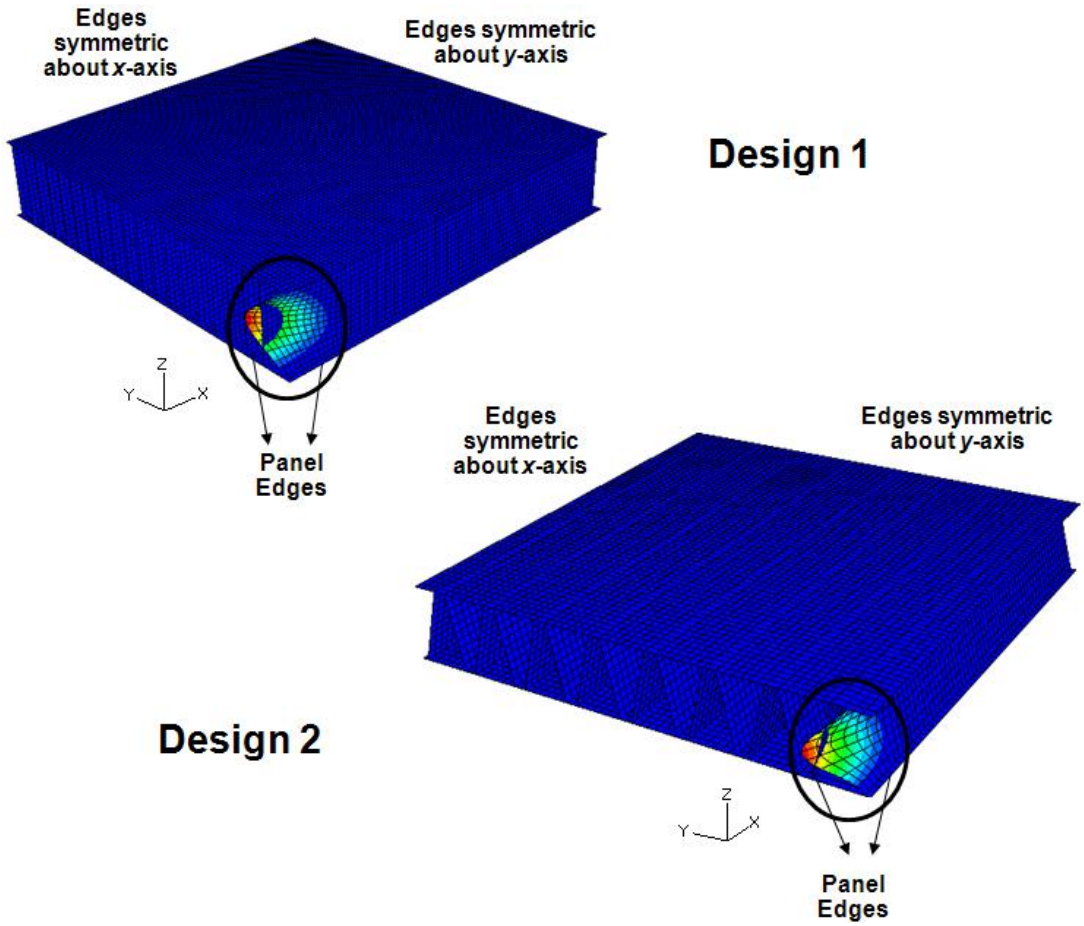

Figure 3-14. Typical web buckling modes of the ITPS panel under thermal loads. The corner most webs near the panel edges always buckles.

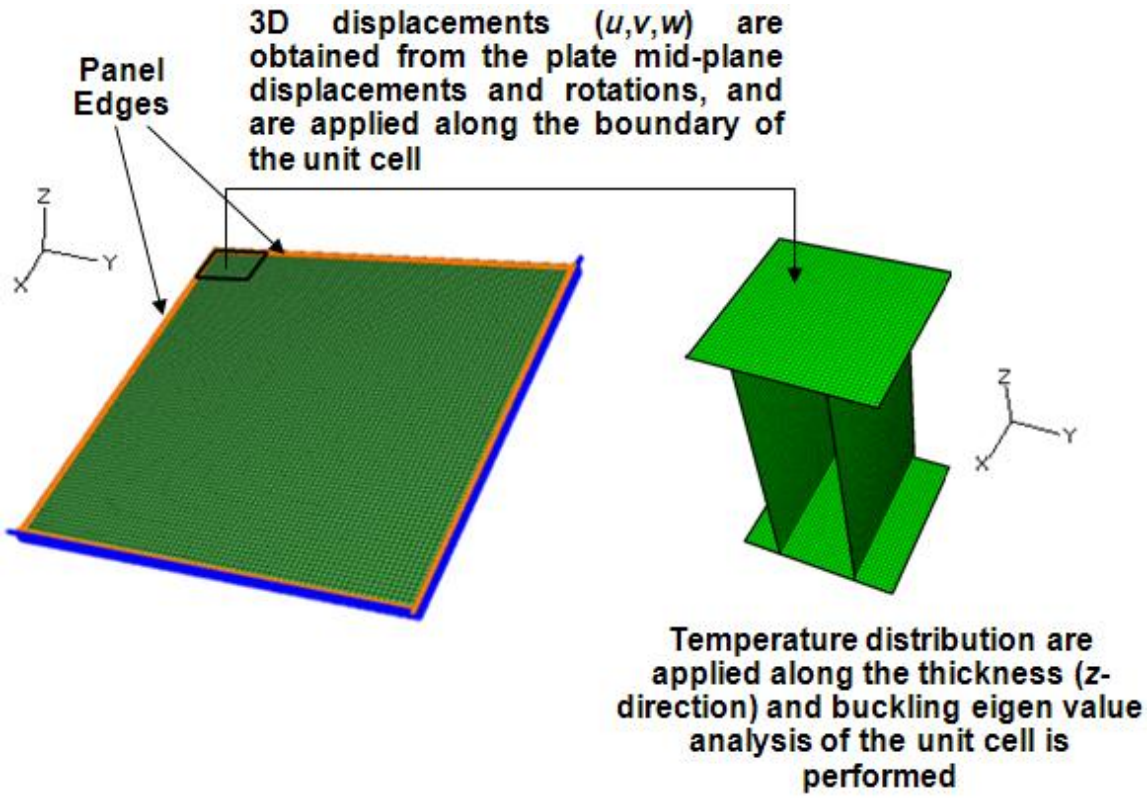

Figure 3-15. Thermal buckling analysis of the unit cell.

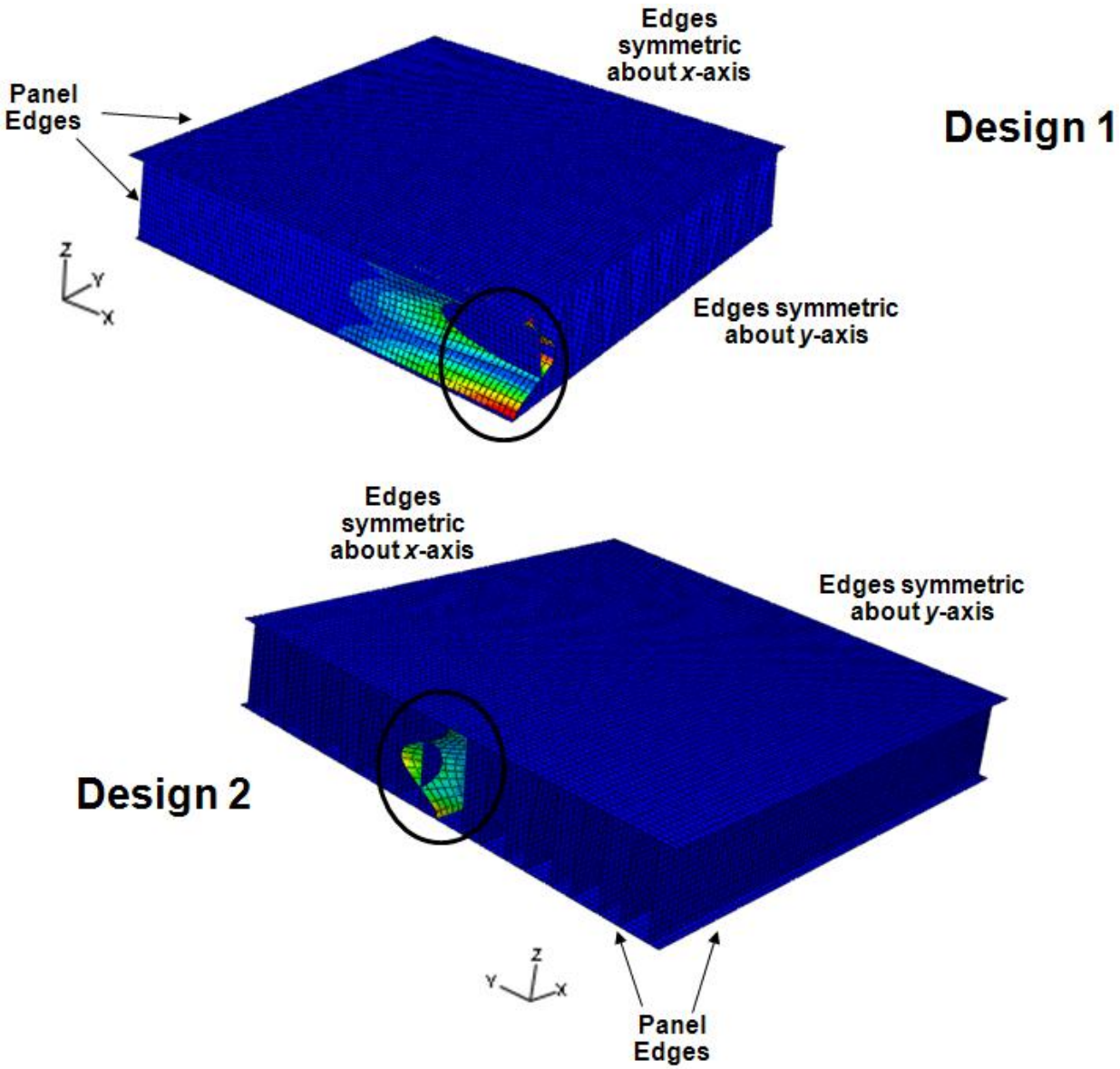

Figure 3-16. Typical web buckling modes of the ITPS panel under aerodynamic pressure loads.

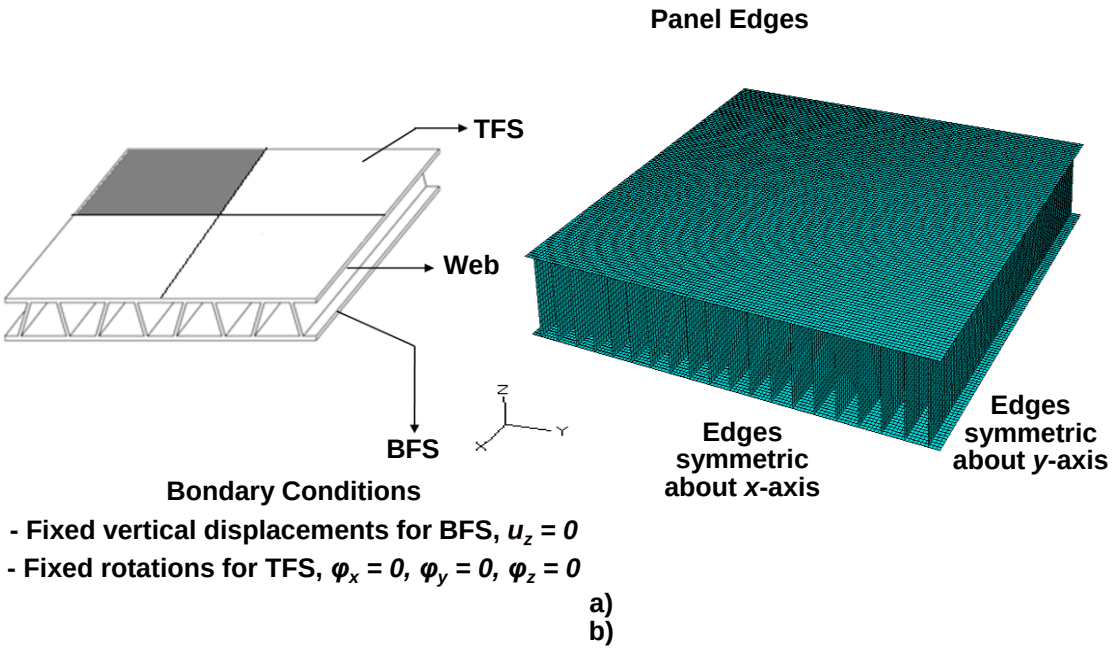

Figure 3-17. Three-dimensional model of the ITPS. a) The ITPS Panel with the boundary conditions, b) Typical mesh for the 3D finite element model of one fourth of the panel.

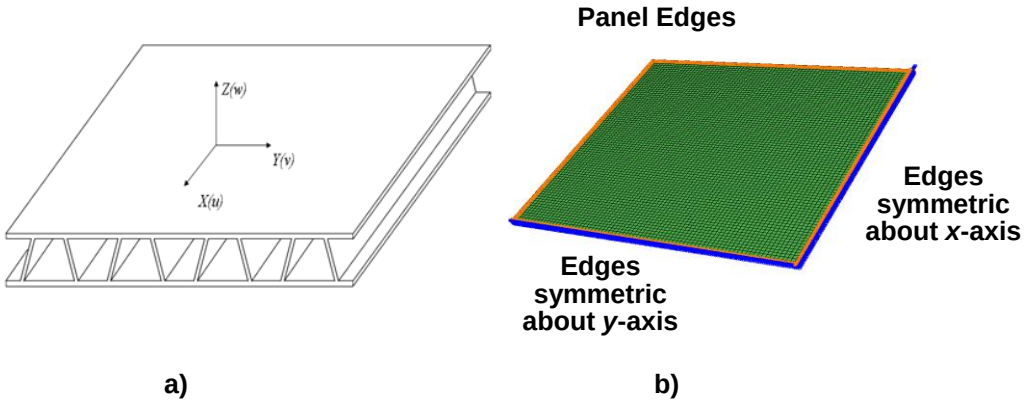

Figure 3-18.Two-dimensional model of the ITPS a) One fourth of the ITPS panel, b) Typical mesh and boundary conditions for the 2D finite element model.

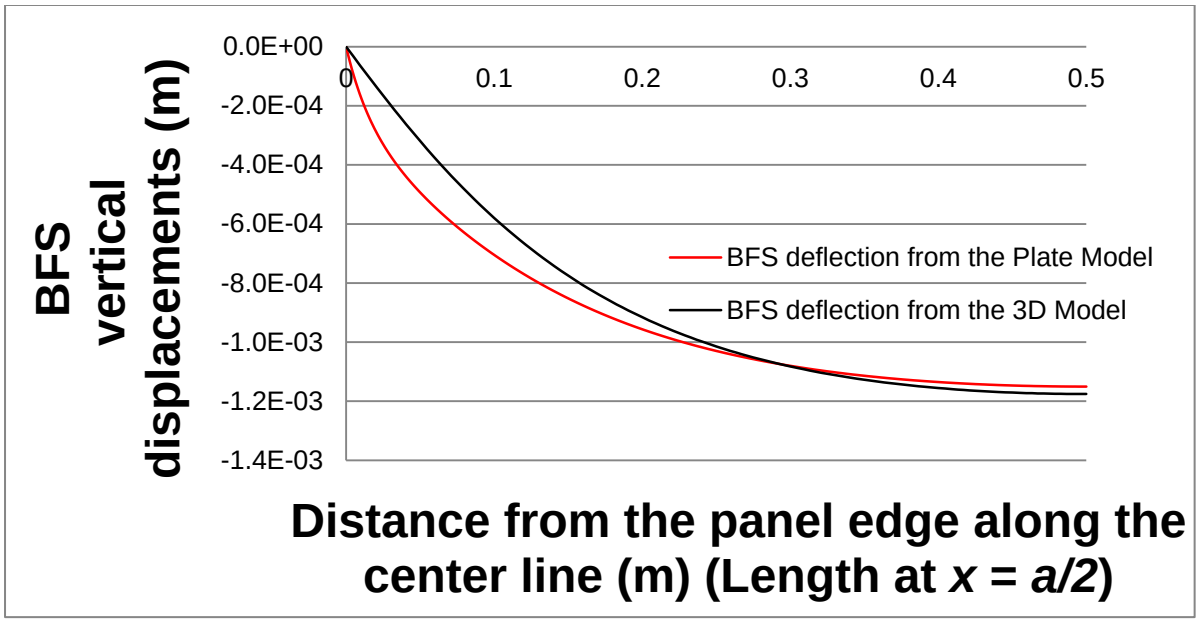

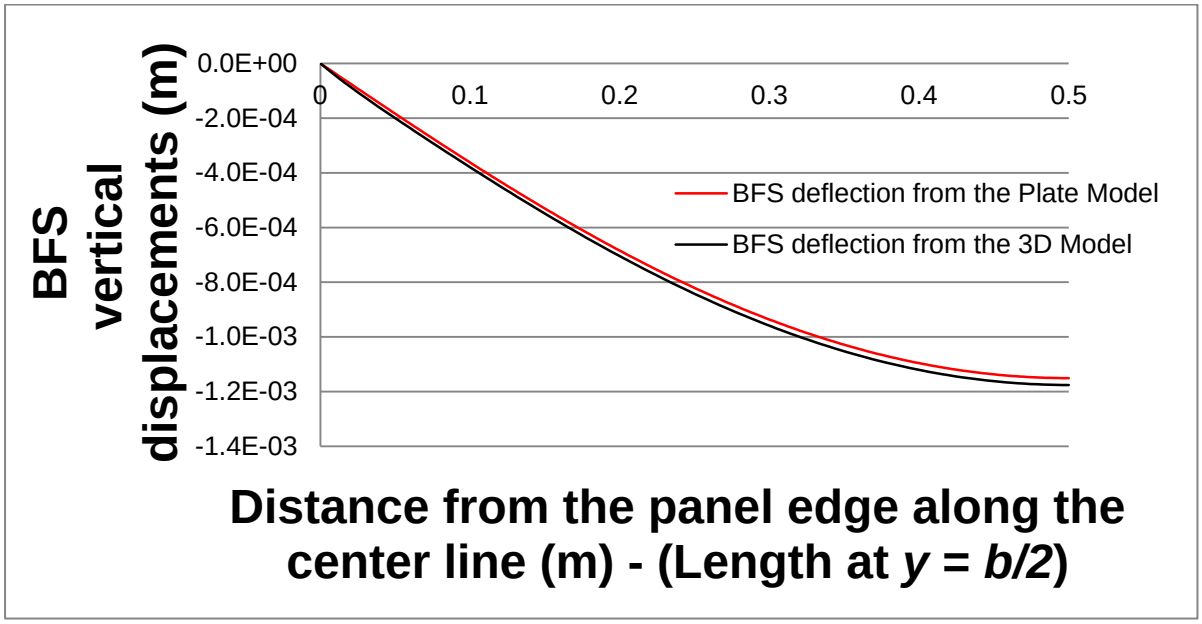

Figure 3-19. Vertical deflections of the plate along the center line parallel to the *y*- and *x*- axes. Deflections of the bottom face sheets from the 3-D model are shown for comparison.

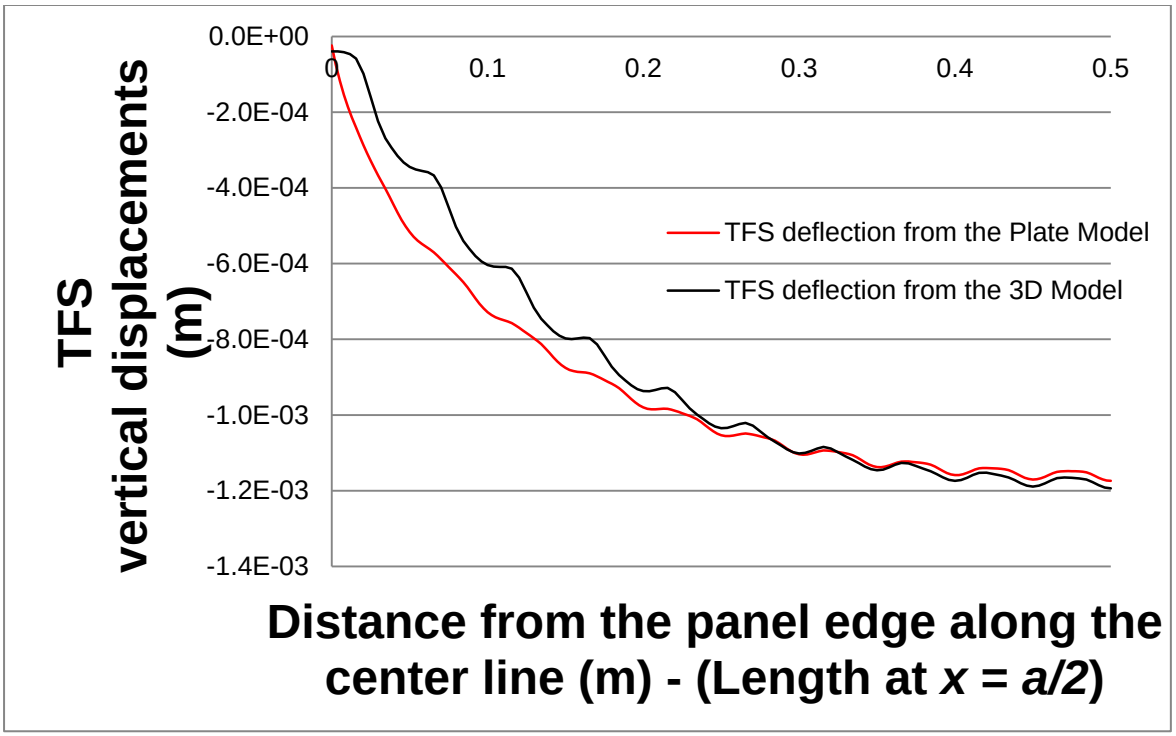

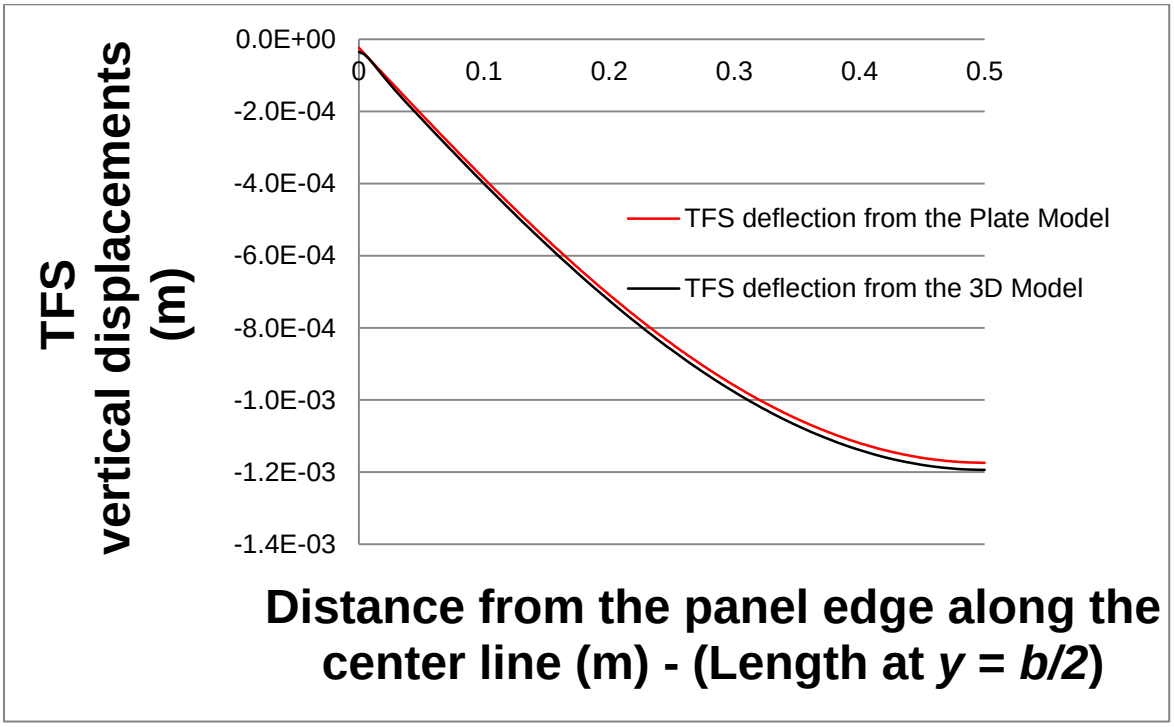

Figure 3-20. Vertical deflections of the plate along the center line parallel to the *y*- and *x*- axes. Deflections of the top face sheets from the 3-D model are shown for comparison.

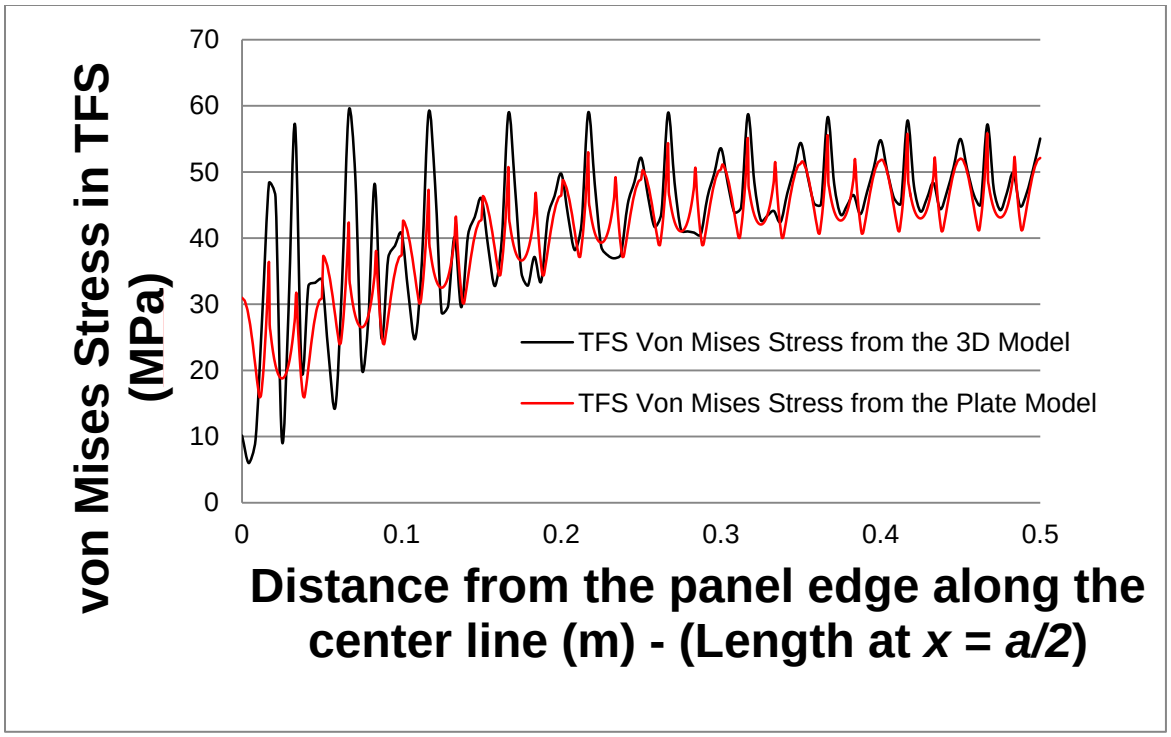

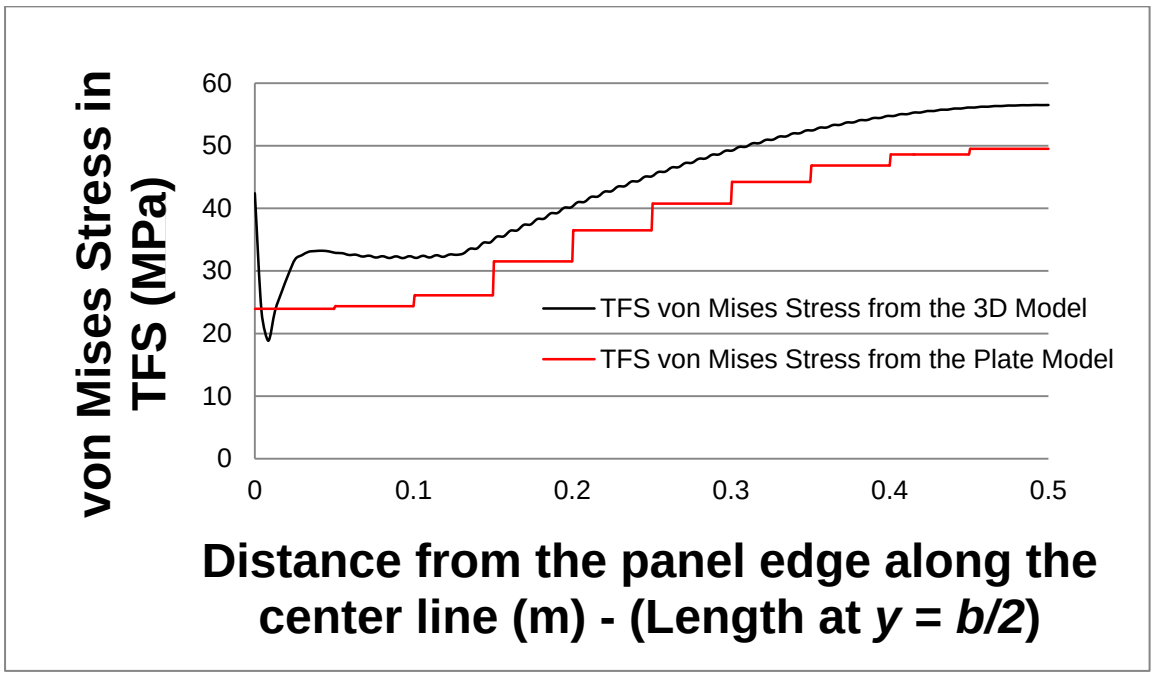

Figure 3-21. Top face sheets von Mises stresses obtained from the plate model along the center line parallel to the *y*- and *x*- axes. Stresses of the top face sheets from the 3-D model are shown for comparison for pressure loading.

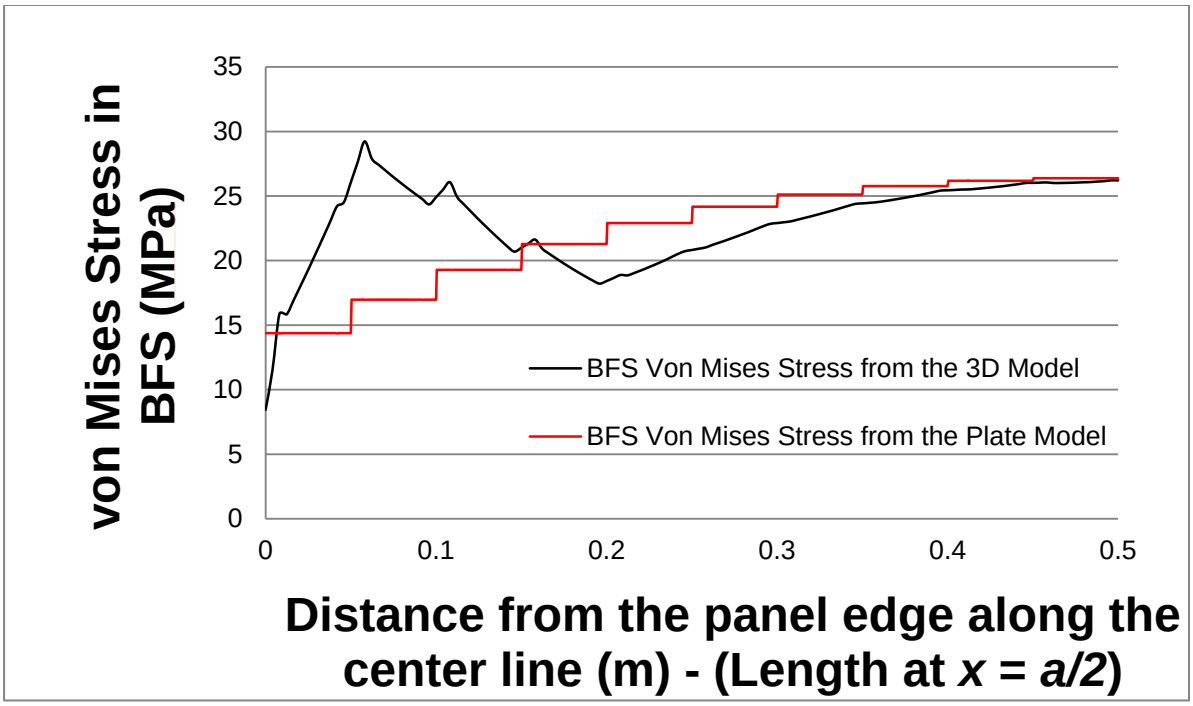

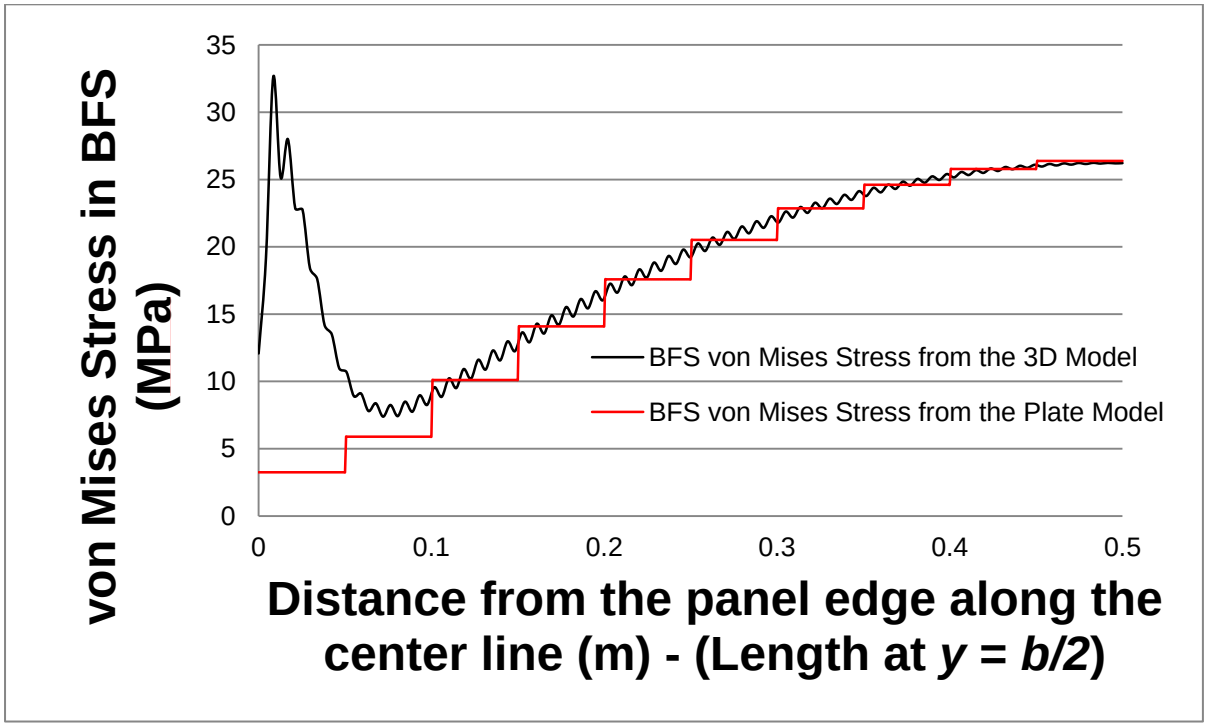

Figure 3-22. Bottom face sheets von Mises stresses obtained from the plate model along the center line parallel to the *y*- and *x*- axes. Stresses of the bottom face sheets from the 3-D model are shown for comparison for pressure loading.

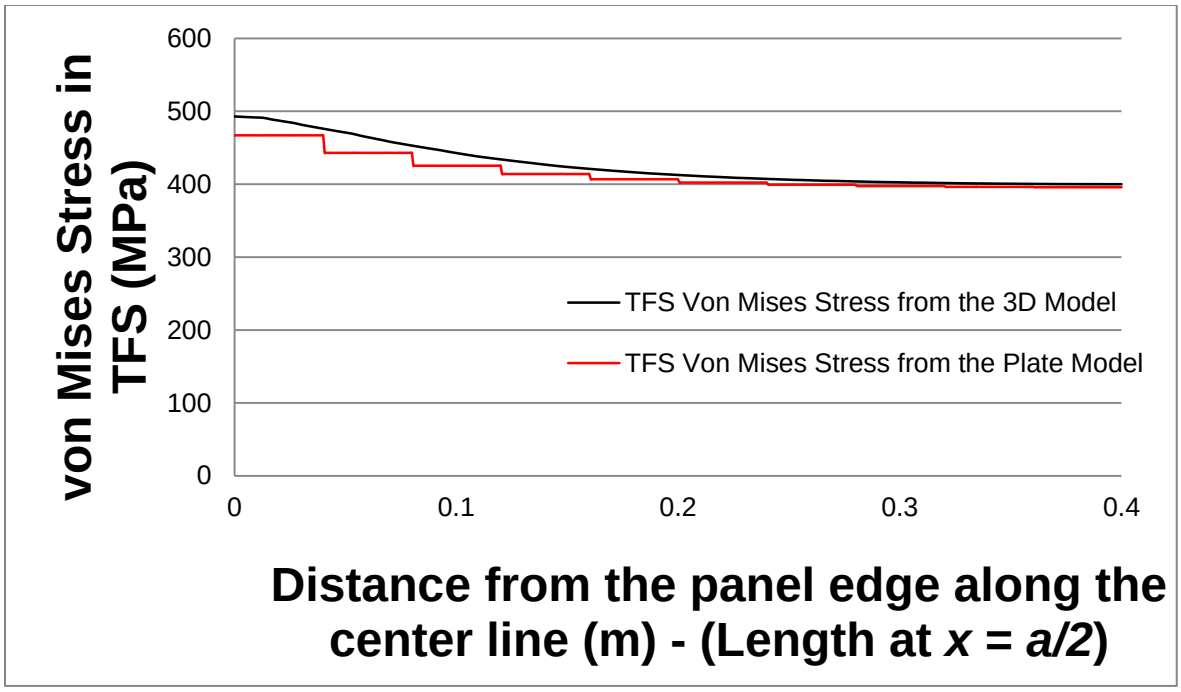

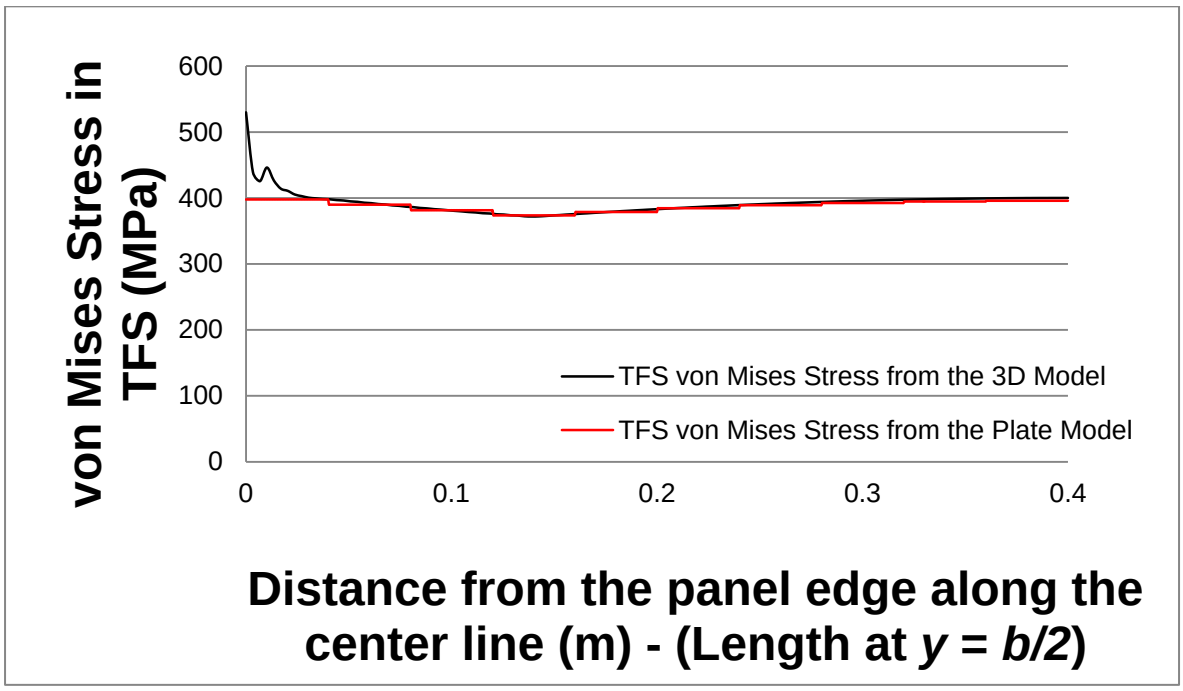

Figure 3-23. Top face sheets von Mises stresses obtained from the plate model along the center line parallel to the *y*- and *x*- axes. Stresses of the top face sheets from the 3-D model are shown for comparison for thermal loading.

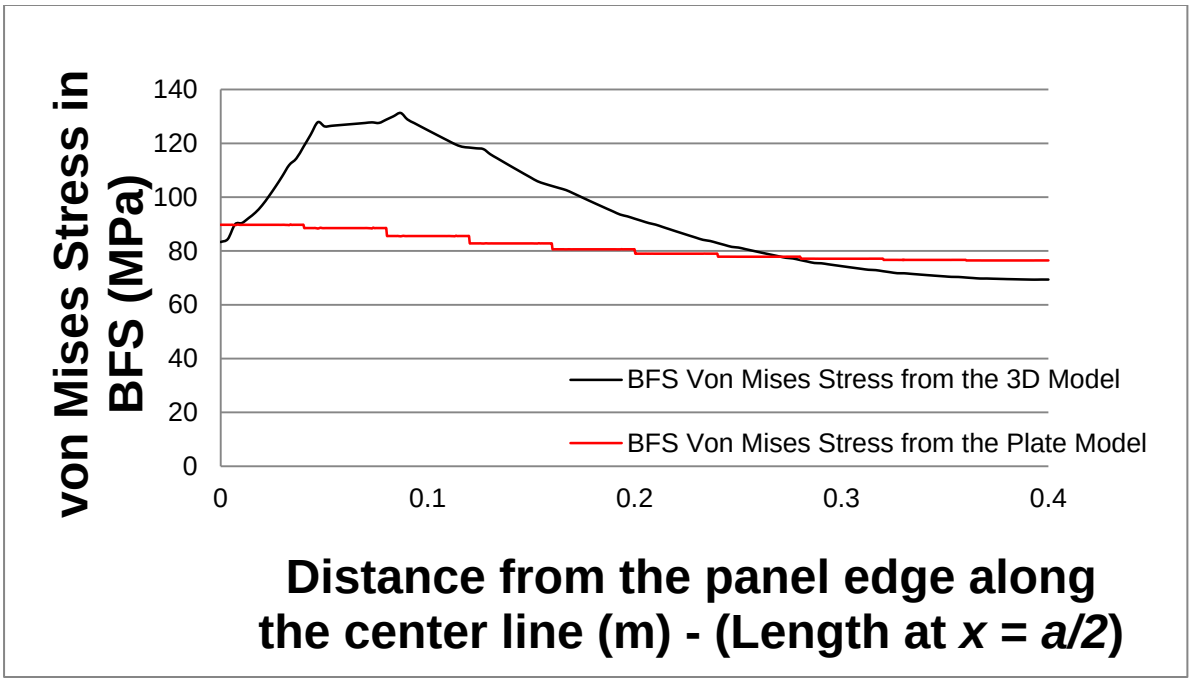

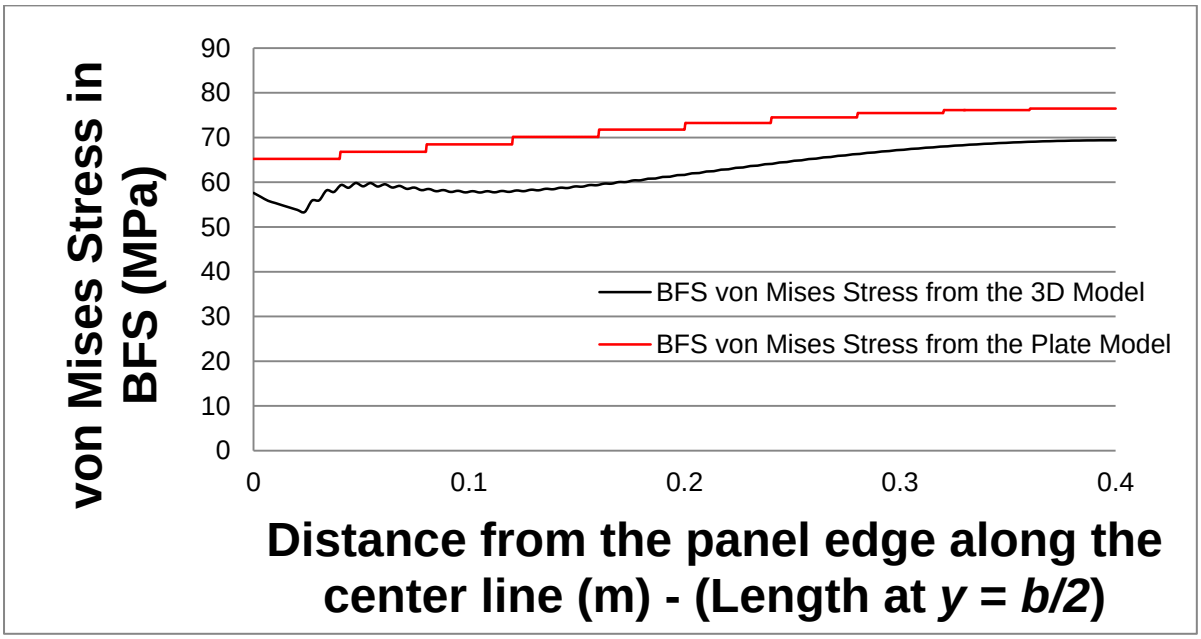

Figure 3-24. Bottom face sheets von Mises stresses obtained from the plate model along the center line parallel to the *y*- and *x*- axes. Stresses of the bottom face sheets from the 3-D model are shown for comparison for thermal loading.

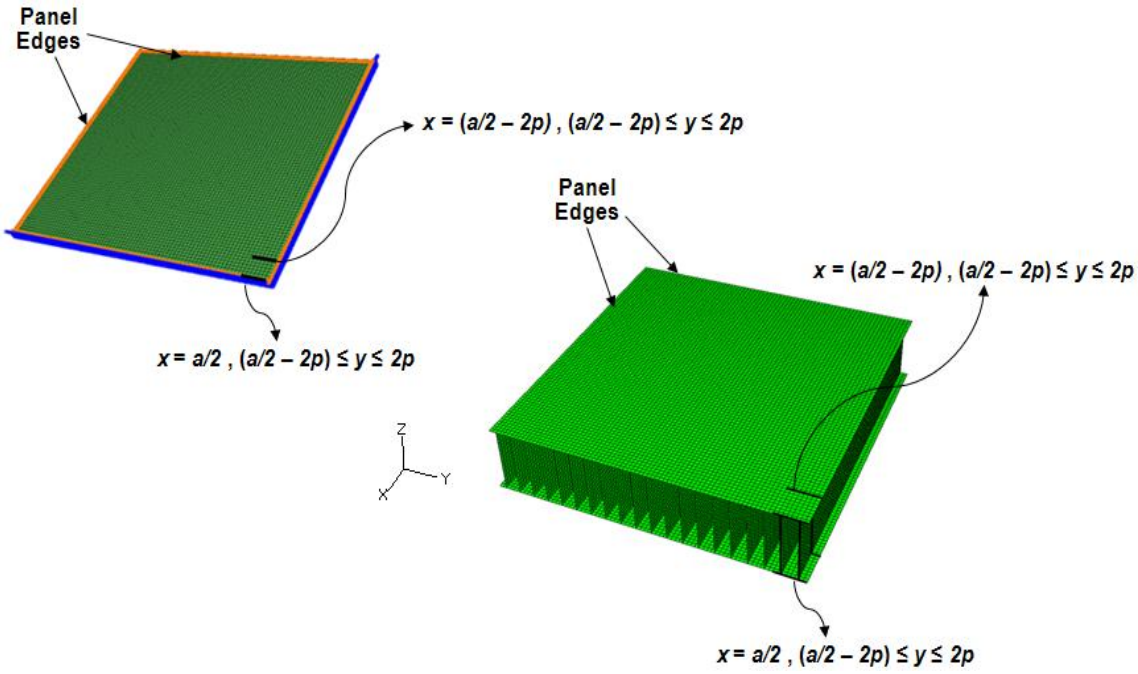

Figure 3-25. Computing *u*, *v* and *w* displacements along the *y*- direction at the center unit cell from the 2D plate displacements.

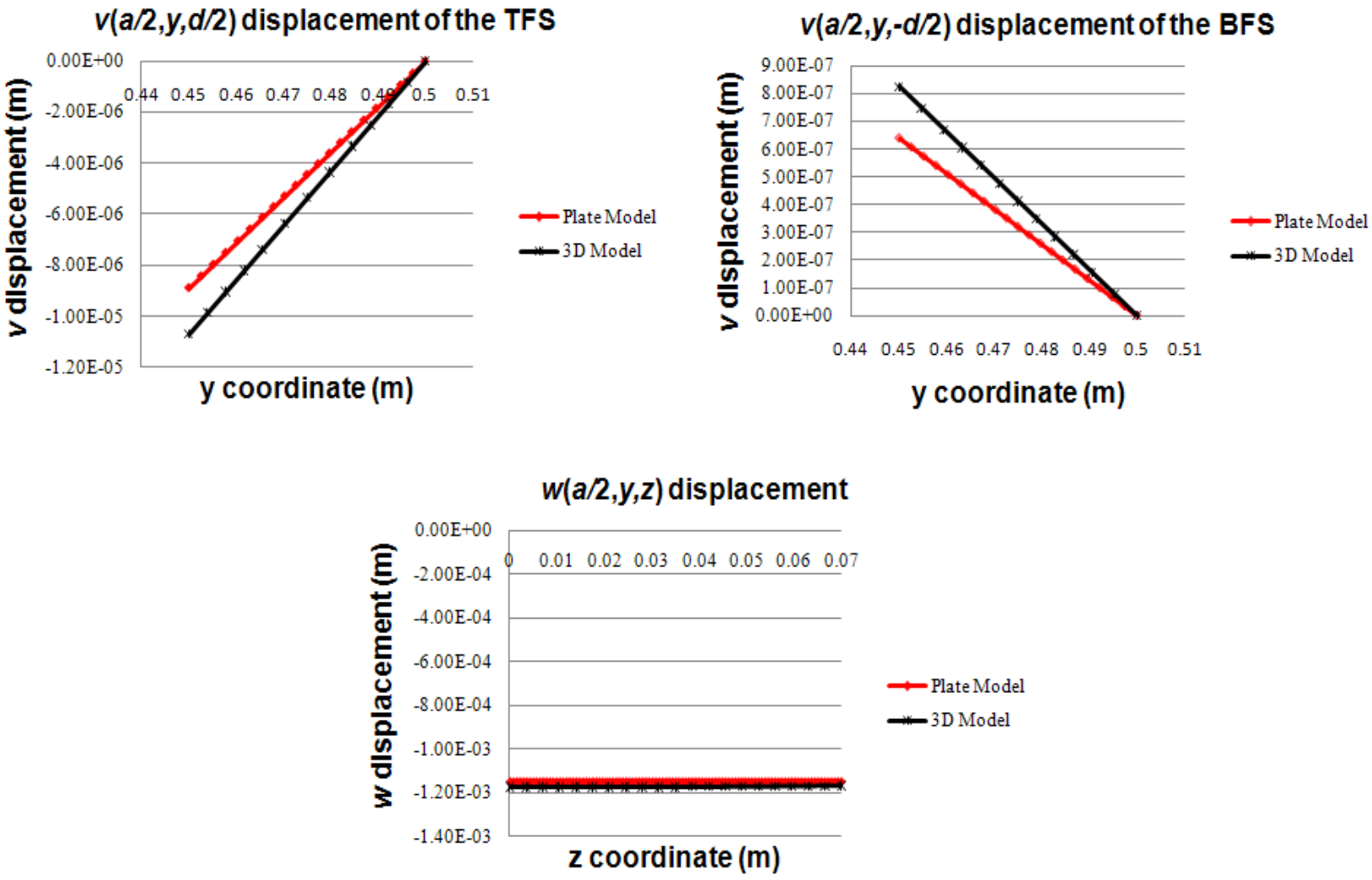

Figure 3-26. *v* and *w* displacements of the TFS, BFS and the web for (*a/2 – 2p*) < *y* < *a/2*. Here *z* varies from *0* to *d*. Here, *x* = *a/2*. (Pressure Loading Case).

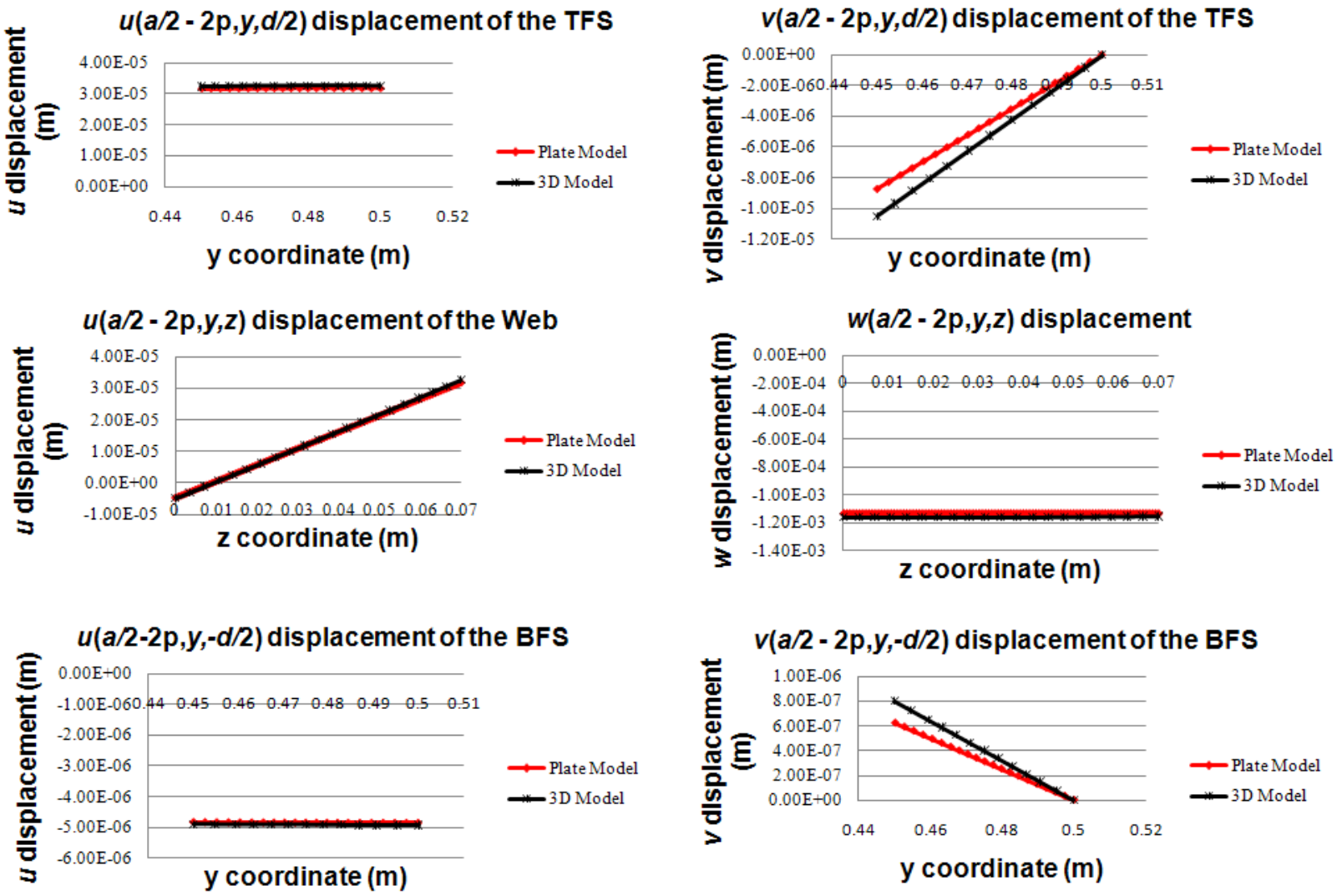

Figure 3-27. *u*, *v* and *w* displacements of the TFS, BFS and the web for (*a/2-2p*) < *y* < *a/2*. Here *z* varies from *0* to *d*. Here, *x* = *a/2-2p*. (Pressure Loading Case).

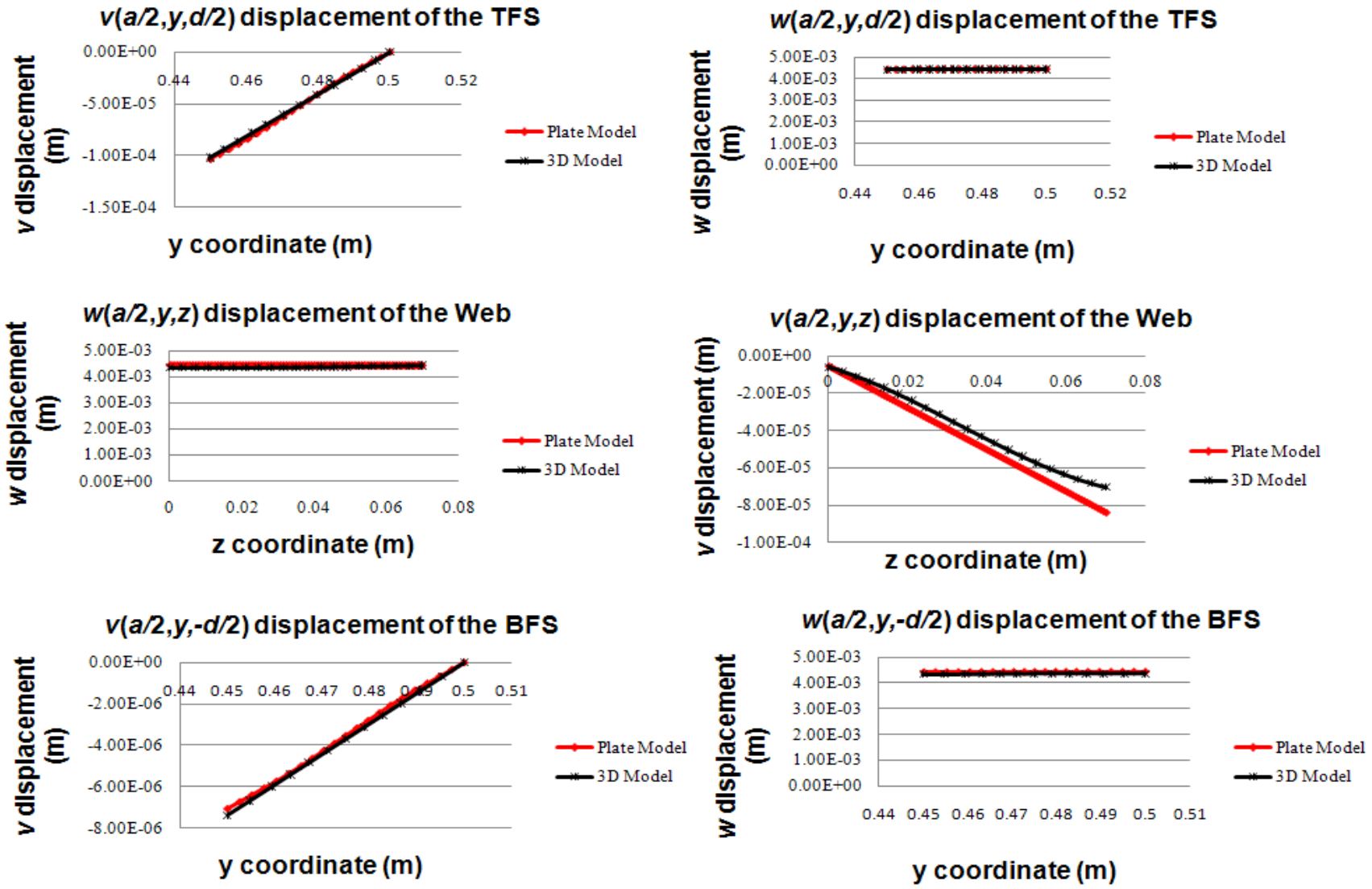

Figure 3-28. *v* and *w* displacements of the TFS, BFS and the web for (*a/2-2p*) < *y* < *a/2*. Here *z* varies from *0* to *d*. Here, *x* = *a/2*. (Thermal Loading Case).

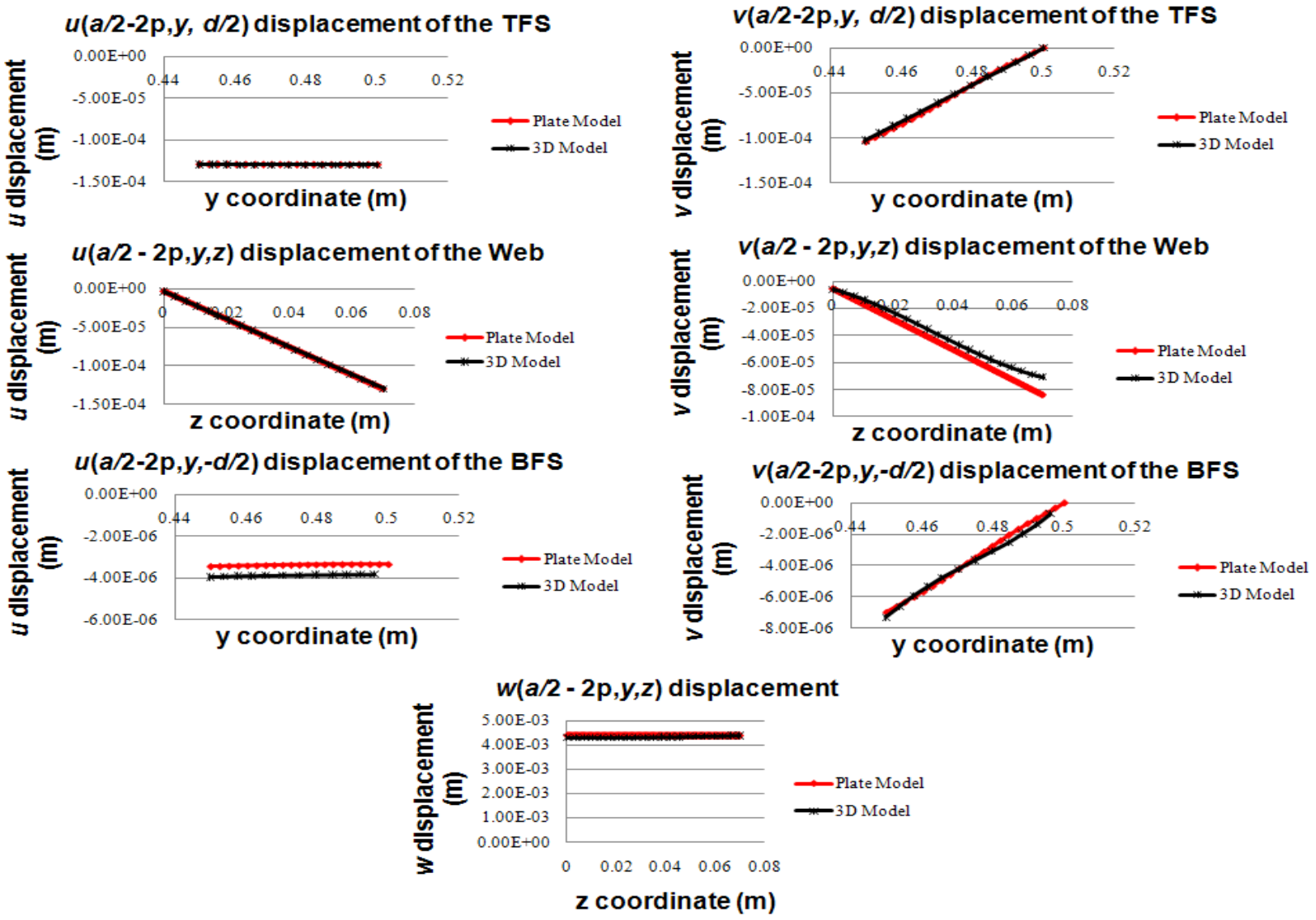

Figure 3-29. *u*, *v* and *w* displacements of the TFS, BFS and the web for (*a/2-2p*) < *y* < *a/2*. Here *z* varies from *0* to *d*. Here, *x* = *a/2-2p*. (Thermal Loading Case).

CHAPTER 4
MULTI-FIDELITY DESIGN AND OPTIMIZATION

ITPS is a key technology for reducing the cost of reusable launch vehicles, offering the combination of increased durability and competitive weights when compared to other systems. Accurate sizing of ITPS requires combined thermal and structural analysis [22]. The TPS and the underlying load bearing structure have various contradictory requirements, which need to be reconciled, in order to find a feasible solution. This is only possible by making the design process as an optimization problem. Further, ITPS will occupy a huge area on the vehicle exteriors and forms a major part of the launch weight. Therefore, material selection, geometric parameters and constraints all contribute to the total mass of the ITPS. The objective of the process is to make the structure as light as possible and at the same time it should fulfill all the functions required of the ITPS.

In [22, 10], the critical functions of an ITPS that have a potential influence on the design were taken into account. Since the main goal is to reduce the weight of the ITPS, the obvious choice for the objective would be mass per unit area of the ITPS panel, M. The optimization problem is stated as minimizing the mass per unit area of the panel while satisfying various constraints as given below.

- Maximum temperature of the bottom face-sheet: The temperature of the underlying structure must at all times be maintained below acceptable limits.
- Maximum global/local deflection of the top face-sheet: The maximum deflection should be within acceptable limits to maintain the aerodynamic shape of the spacecraft. The limits are imposed to prevent premature transition from laminar to turbulent flow, which could significantly increase surface heating. Global deflection refers to the deflection of the whole TPS panel while local deflection refers to dimples that can occur in the unsupported section of the top face sheet.
- Stresses in the panel: In order to maintain structural integrity the stresses in the panel should be within allowable limits. The loads on the TPS panel include

temperature loads that create bending stresses, pressure loads, and in-plane loads from the airframe. Von Mises criterion for yielding is used for metallic structures, while Tsai-Wu failure theory will be used for composite structures.

- Thermal/mechanical buckling: Buckling could be global or local. Global buckling is the event when the whole TPS panel buckles, while local buckling is the event when the thin face-sheets or web buckles locally under the loads.

The relation between the geometric parameters and the constraints can be obtained by using either the 2D FE procedures that were outlined in the previous chapters or using a complete 3D FE analysis. There is also a third approach where we can combine the inexpensive 2D FE approach (takes approximately 10 minutes) with the 3D FE expensive analysis (takes approximately 60-75 minutes) by generating the multi-fidelity surrogates of the constraints which usually allows use of significantly fewer 3D high fidelity analyses for a given accuracy. This multi-fidelity design approach is explained in detail in the next section. The optimization problem was performed by using the MATLAB® optimization function *fmincon*(), which is a built-in MATLAB® optimization function that optimizes an objective function through a Sequential Quadratic Programming algorithm (SQP) [83]. The optimization process was carried out 100 times with a different starting point at each optimization and the design with the lowest weight was chosen as the optimized design.

Multi-Fidelity Design

The problem of optimizing with high cost models is common to many engineering design problems. The design of an ITPS is a challenging task, because the requirement of a load bearing structure and a TPS are often conflicting. However, as the structure is subjected to complex loads like thermal and pressure, the computational time and effort for a 3D FE analysis increase substantially.

Bapanapalli et al [20] developed an optimization procedure to find the optimal design having minimum mass and satisfying all the constraints. The procedure used 3D FE analysis to construct response surface approximations (RSAs) for the critical constraints, including maximum bottom face sheet temperature, maximum deflection, maximum stresses and buckling loads. The RSAs obtained were of high fidelity; however they required large computational time. The cost of generating these response surfaces is high and it increases by an order of magnitude when uncertainties are taken into account and added as additional variables for obtaining a robust design.

Martinez et al [21] developed an analytical model of the ITPS based on homogenization of the panel for calculating displacements and stresses. This model, though relatively inexpensive, was not accurate enough for design optimization. Therefore in Sharma et al [70], these two models were combined into a multi-fidelity model, and maximum stresses and maximum deflection in the top face-sheet of the ITPS structure were calculated under pressure loads. The paper demonstrated that it is possible to construct the RSA for the various constraints that will be used in the optimization of ITPS at higher accuracy and low computational cost by combining low-fidelity models with more accurate but expensive high-fidelity models. For widely varying geometries and material properties, the analytical model had huge discrepancies in their results. Furthermore industries prefers finite element method based homogenization and reverse homogenization procedures, as it is more robust and could be performed with any commercially available FEA programs.

The entire multi-fidelity model could be described as follows. A three-dimensional finite element model of the ITPS is used as the high fidelity model. The low fidelity

model uses the equivalent orthotropic plate, which is analyzed using 2D plate finite elements. The high-fidelity model is used to analyze only a few designs in order to reduce the cost. The errors in the high-fidelity response surfaces were based only on high-fidelity results. To resolve this difficulty, the low fidelity 2D finite element model will be fitted with a high quality surrogate, which will then be corrected by the use of a small number of high fidelity 3D finite element analyses. Fitting the difference or the ratio between the high fidelity analyses and the low fidelity surrogate with a response surface approximation allows construction of the so-called correction response surface. The entire approach, known as multi-fidelity or variable-complexity modeling, usually allows use of significantly fewer high fidelity analyses for a given accuracy.

A common approach is to use the ratio or difference between the low-fidelity and high-fidelity models at one or several points in order to correct the low-fidelity model at other points [71]. Previous researchers, [72, 73, 74] had recommended the method of calculating the ratio and the derivative at one point in order to construct a linear approximation of the ratio at other points in the design space. Nevertheless, fitting the RSA of the difference or the ratio has the benefit over derivative based ratio approximations as it smoothens out numerical noise and can be used on a bigger area in design space [71]. Various researchers [75] have shown the advantages of using the multi-fidelity by combining the 2D FE model with a 3D high fidelity model. Kaufman et al [76] combined the low fidelity with a high fidelity model to optimize the take-off gross weight of the high speed civil transport. Vitali et al [77] combined a large number of inexpensive beam-analysis stress calculation with a small number of the more accurate STAGS FE analyses using RSA to predict stresses and buckling loads in a hat-stiffened

panel. Knill et al and various other researchers [78–80] also demonstrated the use of correction response surfaces and its benefit in improving the accuracy and achieving a lesser computational time for a given accuracy. Balabanov et al [81] optimized the weight of the wing bending material which is a function of the aircraft geometry, by combining the coarse (low fidelity) FE models with refined (high fidelity) FE models.

For the ITPS optimization problem various multi-fidelity response surfaces were compared with the 3D ITPS linear response surface and by looking at the various statistical errors, one can decide which one of the methods fits the best for the given constraints. The best may be one choice for one response and a different one for another response. This is only possible because the cost of the fit is trivial compared to the cost of the simulations.

Six design variables for the ITPS optimization problem were considered for generating the response surfaces as shown in Figure 4-1. The six design variables (DV) considered are: TFS thickness t_{TF}, BFS thickness t_{BF}, web thickness t_W, length of the panel L, height of the sandwich panel d and total number of unit cell in the panel n. The corrugated core ITPS panel is modeled using Ti-6Al-4V alloy for the TFS and webs, and Beryllium alloy for the BFS. The range of dimensions is given in Table 4-1. One of the advantages of ITPS is that larger panels could be used because of the high stiffness offered by sandwich construction. The L/d ratio considered here for generating the response surface is greater than 8 because for the 2D homogenization to work well there needs to be sufficient number of unit cells along the length of the panel for the stresses and deflection to be more accurate.

A Latin Hyper Square design of experiments (DOE) in the six design variables based on maximizing the minimum distance between points is used for both the high fidelity and low fidelity models. The finite element model is coupled to MATLAB® for automating the construction of the model for various input parameters. For each finite element simulation the maximum von Mises stress and the deflection can be extracted, both for the high fidelity and low fidelity models using MATLAB® and ABAQUS® result files.

Now for six design variables, one can afford a sufficient number of simulations for both low fidelity and high fidelity models. However, a lower number of simulations for the high-fidelity model will be used (14 simulations) and a linear polynomial response surface (PRS) will be fitted to the data. For the 2D plate model (low fidelity model), a 3rd degree PRS will be fitted as a function of six design variables in order to get a good fit. A cubic PRS with six design variables has 84 coefficients. The general wisdom to fit the data is that the number of experiments is twice the number of coefficients in order to get a good fit. Therefore for 2D PRS (low fidelity model), 168 simulations were done in order to get a good fit. One can use either the linear PRS based on 3D FE results or the 3rd degree PRS obtained using 2D plate analysis. Based on the accuracy of the fit one can choose which is the best fit for a given constraints.

After generating the 3D and 2D response surfaces, the multi-fidelity response surface is generated and compared. In multi-fidelity response surface, the 3rd degree PRS obtained for the low fidelity model is complemented by a linear correction response surface (CRS) of either the difference or the ratio between the 3D and 2D FE analyses as a function of six design variables. Note that the correction response surface (CRS) is

linear and fitted to 14 points that are common to both high-fidelity and low-fidelity simulations. Two CRSs are analyzed: one for the difference between the high fidelity and low-fidelity analyses and one for the ratio of the two. The final responses can be written as follows.

$$
\begin{aligned}
&S_{Multi-Fidelity} = S^{2D} + S^{Diff\_CRS} \quad or \quad S_{Multi-Fidelity} = S^{2D} \times S^{Ratio\_CRS} \\
&S^{Diff\_CRS} = S^{3D} - S^{2D} = D(x) = CRS\ based\ on the\ difference between\ 3D\ and\ 2D \\
&S^{Ratio\_CRS} = S^{3D} / S^{2D} = R(x) = CRS\ based\ on the\ ratio between\ 3D\ and\ 2D \\
&x\ is a vector of\ six design\ parameters
\end{aligned}
\tag{4-1}
$$

where $S_{Multi-Fidelity}$ is the multi-fidelity RSA, S^{2D} is the low-fidelity RSA and S^{Diff_CRS} or S^{Ratio_CRS} is a linear CRS that is constructed for the difference or ratio between the 3D FE analyses and the 2D Plate analysis.

One more type of multi-fidelity response surface is also analyzed as mentioned in [82]. First, the 2D plate model (low fidelity model) is fitted with a 3rd degree PRS as a function of six design variables using the results from 168 simulations in order to get a good fit. Then, the 3D value (high fidelity model) is fitted as a linear function of 2D plate values (low fidelity model) at 14 common points (Figure 4-3). Sometimes this multi-fidelity response surface works better than using the multi-fidelity response surface based on the difference or the ratio [82]. This multi-fidelity response surface can be written as.

$$
\begin{aligned}
&S_{Multi-Fidelity} = AS^{2D} + B = RS(S^{2D}) \\
&Here, \\
&S^{2D} = 2D\ stress\ or\ deflection\ value\ (low\ fidelity) \\
&A\ and\ B\ will\ be\ fitted\ to\ 2D/3D\ data - (Between\ 14\ simulations)
\end{aligned}
\tag{4-2}
$$

Theses alternative surrogates are used to generate the response of the maximum allowable stresses and deflections and based on the error of the fit; the best response is

chosen for design optimization. As mentioned before, there are two important types of loads that need to be considered in the design optimization of an ITPS. Both occur during the reentry phase of the space vehicle. The two load cases are: (a) thermal load due to severe temperature gradient across the thickness of the ITPS (b) aerodynamic pressure load of 101 kPa acting on the top face sheet. Therefore, the response of the stresses and deflections in the TFS, BFS and the web are generated for these loading conditions as explained in the following sections.

Thermal Analysis

For the thermal loading case, initially the response surface for the maximum von Mises stresses and the minimum buckling eigen value is generated as a function of six design variables. However, later it was realized that for the stresses, this was not an accurate way to represent the stress constraints with a single strength value, as the strength value changes significantly with variation in the temperature. Also since there is a temperature distribution across the thickness of the ITPS, the strength of the material also changes. Therefore, instead of considering the maximum von Mises stress value, the ratio of the maximum von Mises stress in each layer to the corresponding strength value is considered and then the maximum ratio is used to fit with the design variables. Temperature dependent strength values are obtained from [20] for both the Titanium alloy and Beryllium alloy and is accurately represented by a cubic polynomial response surface.

As mentioned before, 3D high-fidelity response and 2D low-fidelity response surfaces were generated. The PRESS and standard error measure the error of the fit, which in the case of the fit to the 3D results, is the only source of error. These errors are also shown in Table 4-2. After generating the 3D and 2D response surfaces, the multi-

fidelity response surface is generated and compared. Three different types of multi-fidelity response surfaces were tried. Again, results from different multi-fidelity response surfaces are compared for maximum stress ratio for the TFS, BFS, web and minimum buckling eigen value as shown in Tables 4-3, 4-4, 4-5 and 4-6, respectively.

Looking at Table 4-3 for the maximum stress ratio for the TFS, the multi-fidelity response surface, where the 3D value (high fidelity model) is fitted as a linear function of 2D plate values (low fidelity model), works best. This is confirmed by looking at the standard error (S.E.) of the fit, which is the unbiased estimate of the RMS error. It is given as the ratio of the sum of the squares of the errors at the design points used for fitting the response surface by the difference between the number of data points and the number of the coefficients used in generating the response surface. Mathematically, S.E. can be written as,

$$
\begin{aligned}
& e = y_{response} - y_{exact} \\
& Sum\,of\ squares\,of\ errors = e^T e \\
& S.E. = \sqrt{\frac{Sum\,of\ squares\,of\ errors}{n_y - n_\beta}} \\
& n_y \rightarrow No.of\ data\ pts.used\ \ for\ generating\,the\,PRS \\
& n_\beta \rightarrow No.of\ coefficients\,used\,in\,the\,PRS
\end{aligned}
\tag{4-3}
$$

Similarly by looking at errors of the fit for the web stress ratio, the multi-fidelity, with 2D low fidelity model complemented by the linear CRS of the ratio, works best among all the other responses (Table 4-4).

Further looking at the responses at the BFS stress ratio (Table 4-5) and buckling eigen value (Table 4-6), the errors of the fit shows that there is not a substantial improvement when one even uses the multi-fidelity response surface as compared to using only the 3D response surface. In order to further improve the quality of the

response surface, a sensitivity analysis is performed [84] using the 3D response surfaces. Sensitivity can be defined as a measure of the contribution of an independent variable to the total variance of the dependent data. By doing this, the more important design variables can be found, which can be used to regenerate the responses in order to get a better fit for the same number of experiments. Now looking at the sensitivity bar graph for BFS stress ratio (Figure 4-4), the more important design variables are the TFS thickness t_{TF}, BFS thickness t_{BF}, and height of the sandwich panel d. For a quadratic PRS based on three design variables, the number of coefficients is 10. Hence, in order to generate the quadratic response surface for the 3D PRS and the CRS PRS, the numbers of simulation results were increased from 14 to 20 3D simulations. Looking at the errors of the fit from the Table 4-7 for the maximum stress ratio for the BFS, it can be seen that the multi-fidelity CRS ratio works the best. Again, looking at the sensitivity bar graph for buckling eigen value (Figure 4-5), the more important design variables are the BFS thickness t_{BF}, web thickness t_W, and height of the sandwich panel d. Initially, PRS was tried for the 3D response surface and the multi-fidelity response surface. Since the PRS did not give a good fit, support vector regression (SVR) was tried. Looking at the errors of the various fit from Table 4-8, the multi-fidelity, with 2D low fidelity model complemented by the CRS of the ratio, works best among all the other responses. The kernel function for both the 2D and CRS ratio that was used for generating the multi-fidelity response is 'Linear Spline' with ε - insensitive (Figure 4-2) value for the 2D and CRS ratio as 0.0155 and 0.02, respectively. Now in order to validate that various option of each responses selected based on the errors of the fit is indeed the best option, it has been validated by calculating the errors at test points.

These test points were not used to fit the data and the errors at the test points also confirms the choice as seen from the Tables 4-3, 4-4, 4-5 and 4-6.

Pressure Analysis

For the pressure loading case, the response surfaces for the maximum von Mises stresses, maximum deflection and the minimum buckling eigen value are generated as a function of six design variables. For the pressure case, only the 3D response surface was generated. As compared to thermal load case, the stresses under the pressure load were very small and much lesser than the yield strength values of the material used. Therefore, the complex 2D and the multi-fidelity approach were not used to further improve the accuracy of the response surface. The R^2 and standard error measure the error of the fit, which in the case of the fit to the 3D results, is the only source of error. These errors are also shown in Table 4-9.

After generating these 3D response surfaces, a sensitivity analysis is done in order to check if there is any further improvement in the quality of the 3D response surfaces. The responses are regenerated using only the important design variables in order to get a better fit for the same number of experiments. Finally, the results for different 3D response surfaces are compared for the maximum von Mises stresses in the TFS, BFS and web, maximum TFS deflection and minimum buckling eigen value as shown in Tables 4-10, 4-11, 4-12, 4-13 and 4-14, respectively.

Now looking at the sensitivity bar graph for TFS maximum von Mises stress (Figure 4-6), the more important design variables are the TFS thickness $t_{TF,}$ BFS thickness $t_{BF,}$ height of the sandwich panel d and length of the panel, L. Now for these four design variables, generating a quadratic PRS involves 15 coefficients. Hence, in order to generate the quadratic response surface for the 3D PRS, the numbers of

simulation results were increased from 14 to 30 3D-simulations. Comparing Table 4-9 and Table 4-10 from the error of the fit for the maximum von Mises stress in the TFS, it can be seen that the 3D SVR (generated using 4 DV) works the best. Since the PRS did not give a good fit, support vector regression (SVR) was tried. The kernel function used for the 3D SVR is 'Polynomial-Degree 2' with the ε - insensitive value as 0.5 MPa.

Looking at the sensitivity bar graph for maximum von Mises stresses in the web (Figure 4-7), the most important design variables are the BFS thickness t_{BF}, web thickness t_W, length of the panel L and number of unit cells in the panel n. Comparing Table 4-9 and Table 4-11 based on the error of the fit for maximum von Mises stresses in the web, quadratic 3D response surface generated using 4 DV gives the best result. Similarly, it can be seen from the sensitivity bar graph for BFS maximum von Mises stress (Figure 4-8), the more important design variables are the BFS thickness t_{BF}, length of the panel L and number of unit cells in the panel n. The quadratic 3D response surface generated using 3 DV works the best as seen from the error of the fit (Table 4-9 and Table 4-12).

Also, looking at the sensitivity bar graph for the TFS maximum deflection (Figure 4-9), the more important design variables are the TFS thickness t_{TF}, BFS thickness t_{BF}, height of the sandwich panel d and length of the panel L. In this case, the quadratic 3D response surface generated using 4 DV works best as witnessed from the error of the fit, by comparing Table 4-9 and Table 4-13. Finally, looking into the sensitivity bar graph for the minimum buckling eigen value (Figure 4-10), the more important design variables are the BFS thickness t_{BF}, web thickness t_W, height of the sandwich panel d and length of the panel L. From Table 4-14 it can be seen that the 3D SVR works the

best for the minimum buckling eigen value. The kernel function used for the 3D SVR is 'GaussianRBF' with the ε - insensitive value as 0.25 and sigma as 2.8. Again the various responses selected based on the error of the fit is actually the best fit, has been validated by calculating the errors at test points, which was not used to fit the data as seen from the Tables 4-9, 4-10, 4-11, 4-12, 4-13 and 4-14. These responses are then used for the optimization problem.

ITPS Optimization

The ITPS structural optimization problem is formulated as a mathematical optimization problem in a specific mathematical form. The problem is to minimize an objective function *f* of *n* variables, x_i. For ITPS optimization problem, *f* is the ITPS mass per unit area and $x_i = [t_{TF}, t_{BF}, t_W, d, L, n]^T$ are the six design variables. The objective function is a function of the design variables. The response surfaces generated in the previous section will be used as the constraints of the optimization function, which are dependent on the design variables. The ranges of the design variables are given in Table 4-1. The objective function for the ITPS optimization problem can be written as,

$$\begin{aligned} &Mass/Area = \rho_{TF} \times t_{TF} + \rho_{BF} \times t_{BF} + \rho_{Web} \times \left[\frac{2dt_w}{(L/n)} \right] \\ &\rho_{TF} - Density\ of\ TFS\ material \\ &\rho_{Web} - Density\ of\ Web\ material \\ &\rho_{BF} - Density\ of\ BFS\ material \end{aligned} \tag{4-4}$$

The following constraints are imposed on the optimization problem.

- Peak bottom face sheet temperature ≤ 260 °C
- Buckling eigen value under pressure and thermal loads ≥ 1.2
- Stress ratio for the thermal loads ≤ 0.85
- Maximum von Mises Stress under pressure loads ≤ $\frac{\sigma_{yield}}{1.2}$
- Top face sheet deflection ≤ 6 mm

The optimization function *fmincon*() first requests an initial guess of the design variables. With that initial guess, the program runs several function evaluations for different design variables that are within the predetermined lower and upper bounds. The program terminates once it has found a minimum value of the objective function in the feasible domain. Feasible domain is the range of design variables where the optimization function is capable of being optimized.

For the optimization, the corrugated-core sandwich structures is modeled using Titanium alloy Ti-6Al-4V (E_1 = 109 GPa and ν = 0.3) for the TFS and the web, and Beryllium alloy (E_1 = 290 GPa and and ν = 0.063) for the BFS. 100 initial guesses were tried and the optimization problem was performed by using the MATLAB® optimization function *fmincon*(). Of all the feasible deisigns, the one with the minimum mass was considered as the optimized mass. The optimized mass was found to be 49.41 kg/m^2. The optimized design is given in Table 4-15. The value of all the constraints is given in Table 4-16. Of all the constraints, the TFS stress ratio and the web stress ratio under thermal load were active.

Concluding Remarks

An optimization procedure was discussed and implemented to obtain the minimum mass per unit area of an ITPS panel. The ITPS panel was optimized under four constraints (deflection, temperature, buckling, and yield). Different types of multi-fidelity response surfaces were tried for the thermal loading case and it was shown that one could select the best of the three alternatives based on the standard errors in the fit for doing the optimization. For the pressure loading case, only the 3D response surfaces were used. Finally, the optimization scheme was done through a built-in sequential quadratic programming algorithm in MATLAB®, and the design variables that were

considered are ITPS width, thickness, number of unit cells, and thickness of each component.

Table 4-1. Ranges of various parameters of the ITPS panel.

Parameter	t_{TF} (mm)	t_{BF} (mm)	t_W (mm)	d (mm)	L (mm)	n (Number of unit cells)
Value	2-5	2-8	1-2	70-90	800-1000	16-20

Table 4-2. Errors in TFS, Web and BFS maximum stress ratio and minimum buckling eigen value for thermal loading in the low fidelity 2D PRS (cubic) and 3D PRS (linear) based on 3D FE analyses of the panel at 50 test points. These test points are not used in generating the response surfaces. The R^2, PRESS and standard error measures the error of the fit. Response surface generated using 6 design variables (DV).

	TFS Stress Ratio		WEB Stress Ratio		BFS Stress Ratio		Buckling Eigen Value	
Mean of 3D corresponding values at 50 test points	0.882		1.01		1.31		1.193	
Polynomial Response Surface	3D FE (linear)	2D plate (cubic)	3D FE (linear)	2D plate (cubic)	3D FE (linear)	2D plate (cubic)	3D FE (linear)	2D plate (cubic)
R^2	0.241	0.74	0.85	0.81	0.68	0.964	0.97	0.997
PRESS RMS	0.127	0.178	0.134	0.0166	0.67	0.084	0.142	0.0075
Standard Error	0.11	0.096	0.1	0.01	0.5	0.04	0.096	0.045

Table 4-3. Comparison of the 3D, 2D and multi-fidelity response surfaces for the maximum stress ratio in the TFS for thermal loading based on exact values of the 3D FE analyses at 50 design points. The standard error measures the error of the fit. Response surface generated using 6 design variables (DV).

ITPS component	Mean of 3D stresses ratio at 50 test points	Different types of Response Surface	Maximum Error	Maximum Error Percentage	RMS Error	Standard Error
TFS	0.882	3D Linear PRS	0.277	28.9	0.09	0.11
		2D Cubic PRS (Cubic)	0.515	64	0.194	0.096
		Multi-fidelity PRS (Cubic 2D + Linear CRS Difference)	0.497	61.7	0.157	0.087
		Multi-fidelity PRS (Cubic 2D X Linear CRS Ratio)	0.457	50.5	0.137	0.066
		Multi-fidelity PRS (3D value fitted linearly to 2D plate values)	0.0845	8.71	0.039	0.037

Table 4-4. Comparison of the 3D, 2D and multi-fidelity response surfaces for the maximum stress ratio in the Web for thermal loading based on exact values of the 3D FE analyses at 50 design points. The standard error measures the error of the fit. Response surface generated using 6 design variables (DV).

ITPS component	Mean of 3D stresses ratio at 50 test points	Different types of Response Surface	Maximum Error	Maximum Error Percentage	RMS Error	Standard Error
Web	1.01	3D Linear PRS	0.26	21.9	0.082	0.1
		2D Cubic PRS (Cubic)	0.303	24	0.135	0.01
		Multi-fidelity PRS (Cubic 2D + Linear CRS Difference)	0.107	12.4	0.04	0.059
		Multi-fidelity PRS (Cubic 2D X Linear CRS Ratio)	0.113	13	0.042	0.06
		Multi-fidelity PRS (3D value fitted linearly to 2D plate values)	0.246	19.5	0.12	0.15
		Multi-fidelity PRS (Linear 2D + Linear CRS Diff)	0.0837	7.05	0.037	0.051
		Multi-fidelity PRS (Linear 2D X Linear CRS Ratio)	0.082	6.9	0.036	0.05

Table 4-5. Comparison of the 3D, 2D and multi-fidelity response surfaces for the maximum stress ratio in the BFS for thermal loading based on exact values of the 3D FE analyses at 50 design points. The standard error measures the error of the fit. Response surface generated using 6 design variables (DV).

ITPS component	Mean of 3D stresses ratio at 50 test points	Different types of Response Surface	Maximum Error	Maximum Error Percentage	RMS Error	Standard Error
BFS	1.31	3D Linear PRS	1.049	33.7	0.35	0.5
		2D Cubic PRS (Cubic)	2.07	66.7	0.88	0.04
		Multi-fidelity PRS (Cubic 2D + Linear CRS Difference)	0.775	24.9	0.32	0.47
		Multi-fidelity PRS (Cubic 2D X Linear CRS Ratio)	0.695	27.8	0.29	0.41
		Multi-fidelity PRS (3D value fitted linearly to 2D plate values)	1.06	47	0.5	0.8

Table 4-6. Comparison of the 3D, 2D and multi-fidelity response surfaces for the minimum buckling eigen value for thermal loading based on exact values of the 3D FE analyses at 50 design points. The standard error measures the error of the fit. Response surface generated using 6 design variables (DV).

	Mean of 3D buckling eigen value at 50 test points	Different types of Response Surface	Maximum Error	Maximum Error Percentage	RMS Error	Standard Error
Minimum Buckling Eigen Value	1.193	3D Linear PRS	0.442	19.8	0.151	0.0965
		2D Cubic PRS (Cubic)	0.74	79.7	0.263	0.045
		Multi-fidelity PRS (Cubic 2D + Linear CRS Difference)	0.32	33.9	0.127	0.102
		Multi-fidelity PRS (Cubic 2D X Linear CRS Ratio)	0.4	16.3	0.12	0.074
		Multi-fidelity PRS (3D value fitted linearly to 2D plate values)	0.56	59.7	0.19	0.25

Table 4-7. Comparison of the 3D, 2D and multi-fidelity response surfaces for the maximum stress ratio in the BFS for thermal loading based on exact values of the 3D FE analyses at 64 design points. The standard error measures the error of the fit. Response surface generated using 3 design variables (DV)-t_{TF}, t_{BF}, d.

ITPS component	Mean of 3D stresses ratio at 50 test points	Different types of Response Surface	Maximum Error	Maximum Error Percentage	RMS Error	Standard Error
BFS	1.857	3D Linear PRS (generated using 6 DV)	1.049	33.7	0.35	0.5
		3D Quadratic PRS (generated using 3 DV)	0.565	21.8	0.24	0.18
		2D Cubic PRS (Cubic) (generated using 3DV)	2.39	77	0.895	0.12
		Multi-fidelity PRS (Cubic 2D + Quadratic CRS Difference) (generated using 3 DV)	0.394	21.3	0.188	0.195
		Multi-fidelity PRS (Cubic 2D X Quadratic CRS Ratio) (generated using 3 DV)	0.328	12.6	0.16	0.19

Table 4-8. Comparison of the 3D, 2D and multi-fidelity response surfaces for the maximum for the minimum buckling eigen value for thermal loading based on exact values of the 3D FE analyses at 50 design points. Response surface generated using 3 design variables (DV)-t_{BF}, t_W, d.

	Mean of 3D buckling eigen value at 50 test points	Different types of Response Surface	Maximum Error	Maximum Error Percentage	RMS Error
Minimum Buckling Eigen Value	1.193	3D Linear PRS (generated using 6 DV)	0.442	19.8	0.151
		3D SVR (generated using 3 DV)	0.378	15	0.117
		2D Quadratic PRS (Cubic) (generated using 3 DV)	0.454	51.6	0.2
		Multi-fidelity SVR (2D X CRS Ratio) (generated using 3 DV)	0.24	11.2	0.0823

Table 4-9. Errors in TFS, Web and BFS maximum von Mises stress, maximum TFS deflection and minimum buckling eigen value for pressure loading in the 3D PRS (linear) based on 3D FE analyses of the panel at 50 test points. These test points are not used in generating the response surfaces. The R^2 and standard error measures the error of the fit. Response surface generated using 6 design variables (DV).

	TFS von Mises Stress	WEB von Mises Stress	BFS von Mises Stress	TFS Deflection	Buckling Eigen Value
Mean of 3D corresponding values at 50 test points	55.25 MPa	214 MPa	75.81 MPa	4.35×10^{-4} m	9
Polynomial Response Surface	3D FE (linear)	3D FE (linear)	3D FE (linear)	3D FE (linear)	3D FE (linear)
Maximum Error	25.84 MPa	21.4 MPa	93.93 MPa	1.475×10^{-4} m	5.098
Maximum error percentage	23.78	100.8	38.3	18.3	26.2
RMS Error	6.9 MPa	25.87 MPa	23 MPa	4×10^{-5} m	1.5
R^2	0.965	0.943	0.838	0.948	0.974
Standard Error	4 MPa	27.413 MPa	25.98 MPa	5×10^{-5} m	1

Table 4-10. Comparison of the various 3D response surfaces for the maximum von Mises stress in the TFS for pressure loading based on exact values of the 3D FE analyses at 34 design points. Response surface generated using 4 design variables (DV)-t_{TF}, t_{BF}, d, L.

ITPS component	Mean of 3D von Mises stress at 34 test points (MPa)	Different types of Response Surface	Maximum Error (MPa)	Maximum Error Percentage	RMS Error (MPa)	PRESSRMS (MPa)
TFS	56	3D Quadratic PRS (generated using 4 DV)	23.98	22.1	6.9	7
		3D SVR (generated using 4 DV)	23.72	21.8	6.87	6.7

Table 4-11. Comparison of the various 3D response surfaces for the maximum von Mises stress in the Web for pressure loading based on exact values of the 3D FE analyses at 34 design points. Response surface generated using 4 design variables (DV)-t_{BF}, t_W, L, n. The standard error measures the error of the fit.

ITPS component	Mean of 3D von Mises stress at 34 test points (MPa)	Different types of Response Surface	Maximum Error (MPa)	Maximum Error Percentage	RMS Error (MPa)	Standard Error (MPa)
Web	224	3D Quadratic PRS (generated using 4 DV)	41.28	8.7	10	7

Table 4-12. Comparison of the various 3D response surfaces for the maximum von Mises stress in the BFS for pressure loading based on exact values of the 3D FE analyses at 44 design points. Response surface generated using 3 design variables (DV)-t_{BF}, L, n.

ITPS component	Mean of 3D von Mises stress at 44 test points (MPa)	Different types of Response Surface	Maximum Error (MPa)	Maximum Error Percentage	RMS Error (MPa)	Standard Error (MPa)
BFS	77.5	3D Quadratic PRS (generated using 3 DV)	34.55	14	8.42	4

Table 4-13. Comparison of the various 3D response surfaces for the maximum TFS deflection for pressure loading based on exact values of the 3D FE analyses at 34 design points. Response surface generated using 4 design variables (DV)-t_{TF}, t_{BF}, d, L. The standard error measures the error of the fit.

ITPS component	Mean of 3D TFS deflection at 34 test points (m)	Different types of Response Surface	Maximum Error (m)	Maximum Error Percentage	RMS Error (m)	Standard Error (m)
TFS	4.37×10^{-4}	3D Quadratic PRS (generated using 4 DV)	1.41×10^{-4}	17.5	4×10^{-5}	3×10^{-5}

Table 4-14. Comparison of the various 3D response surfaces for the minimum buckling eigen value for pressure loading based on exact values of the 3D FE analyses at design points. Response surface generated using 4 design variables (DV)-t_{BF}, t_W, d, L.

	Mean of 3D buckling eigen value at 50 test points	Different types of Response Surface	Maximum Error	Maximum Error Percentage	RMS Error	PRESSRMS
Minimum Buckling Eigen Value	9	3D Linear PRS (generated using 6 DV)	5.098	26.2	1.55	1.578
		3D SVR (generated using 4 DV)	2.6	12.4	0.83	0.61

Table 4-15. Optimized design.

t_{TF} (mm)	t_{BF} (mm)	t_W (mm)	d (mm)	L (mm)	n (Number of unit cells)
2	7.32	1.68	87.14	891.95	20

Table 4-16. Constraints value at the optimum.

Constraint	Description	Value at Optimum
1	BFS Stress (Pressure)	29.88 MPa
2	BFS Stress Ratio (Thermal)	0.81
3	Buckling EV (Pressure)	11.91
4	Buckling EV (Thermal)	1.25
5	TFS deflection (pressure)	3.56×10^{-4} m
6	TFS Stress (Pressure)	45.17 MPa
7	TFS Stress Ratio (Thermal)	0.85
8	Web Stress (Pressure)	120.67 MPa
9	Web Stress Ratio (Thermal)	0.85
10	Max BFS Temp	523.29 K

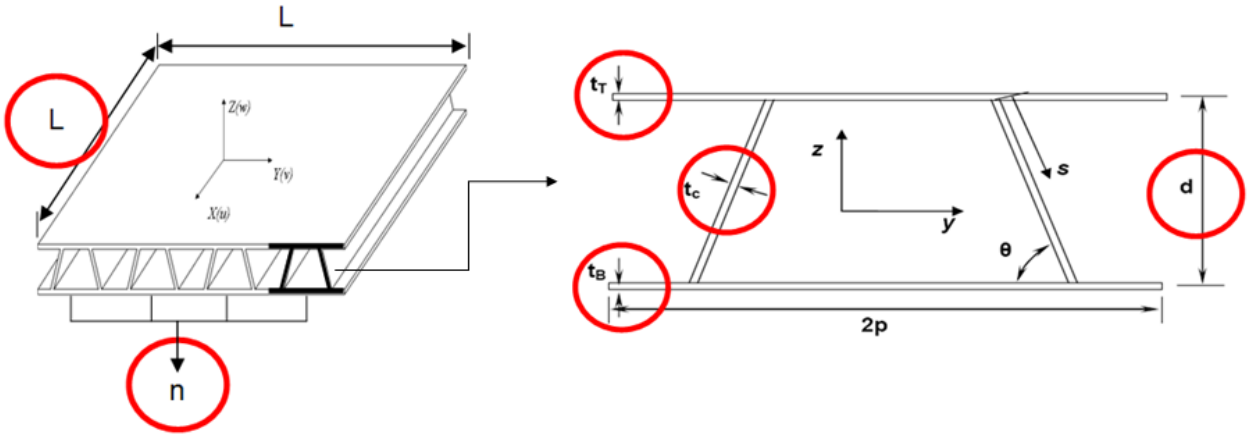

Figure 4-1. 3D ITPS panel and the unit-cell of the corrugated-core sandwich structure with all the six design variables used for generating the response surface.

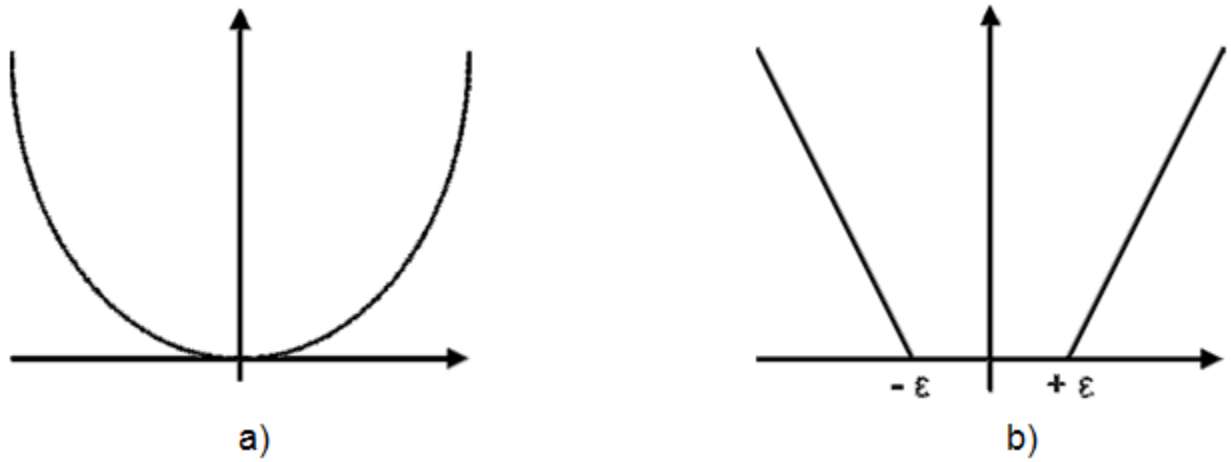

Figure 4-2. Loss function used in the SVR fitting process. a) Quadratic, b) ε-insensitive.

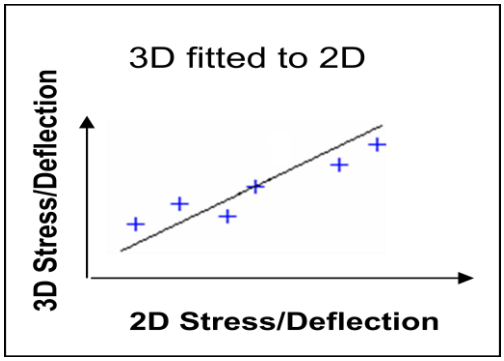

Figure 4-3. 3D value is fitted as a linear function of a 2D Plate values.

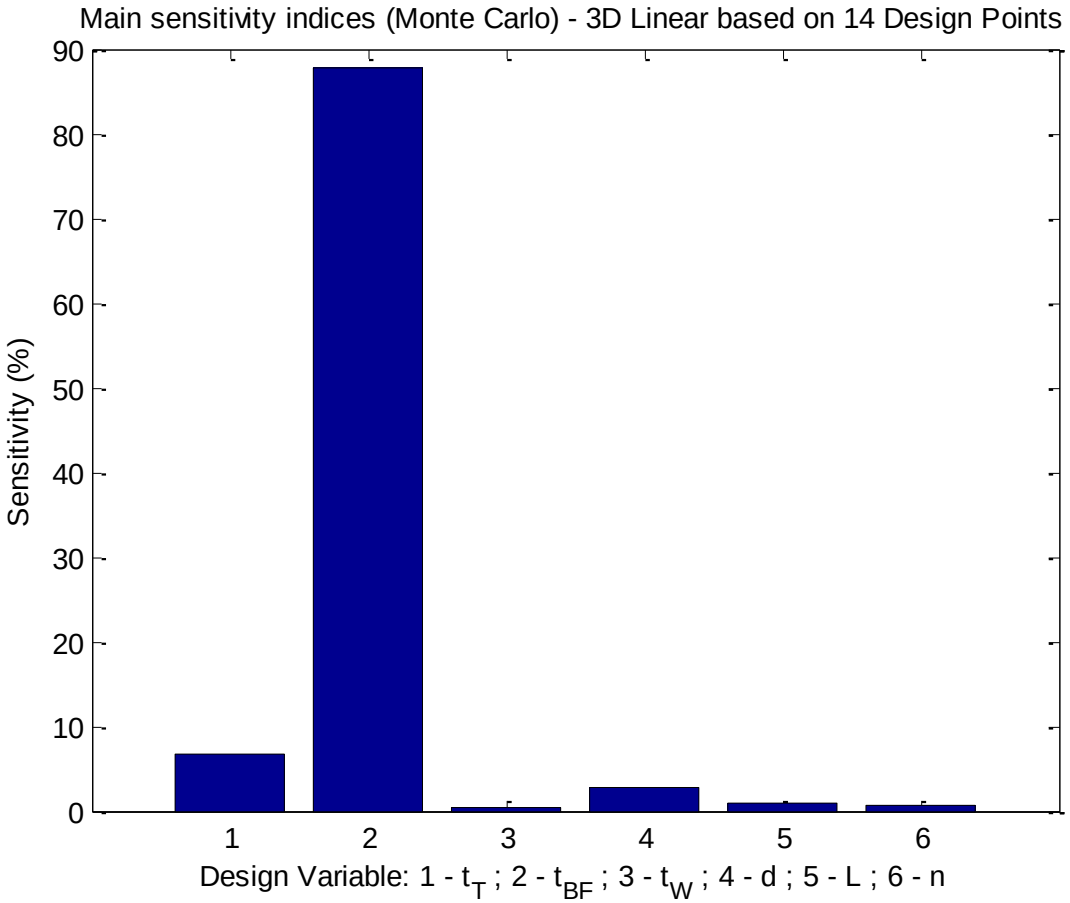

Figure 4-4. Sensitivity indices for the maximum BFS stress ratio under thermal loading.

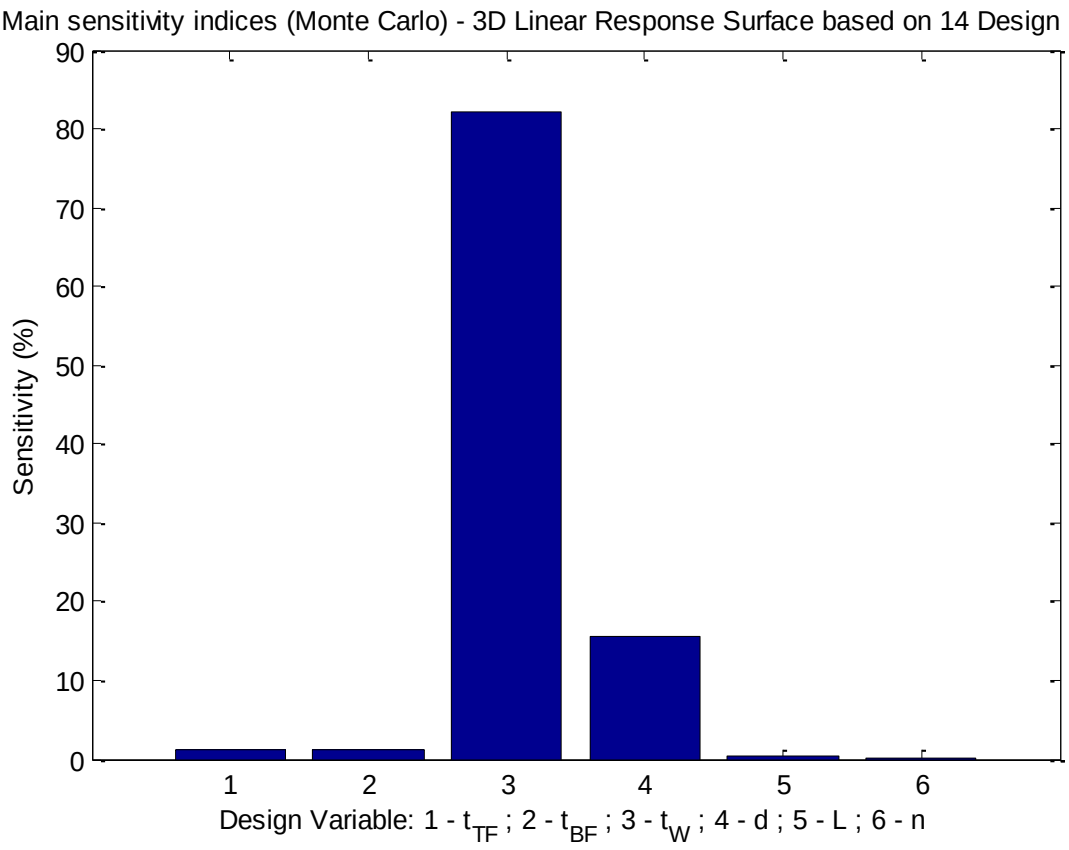

Figure 4-5. Sensitivity indices for the minimum buckling eigen value under thermal loading.

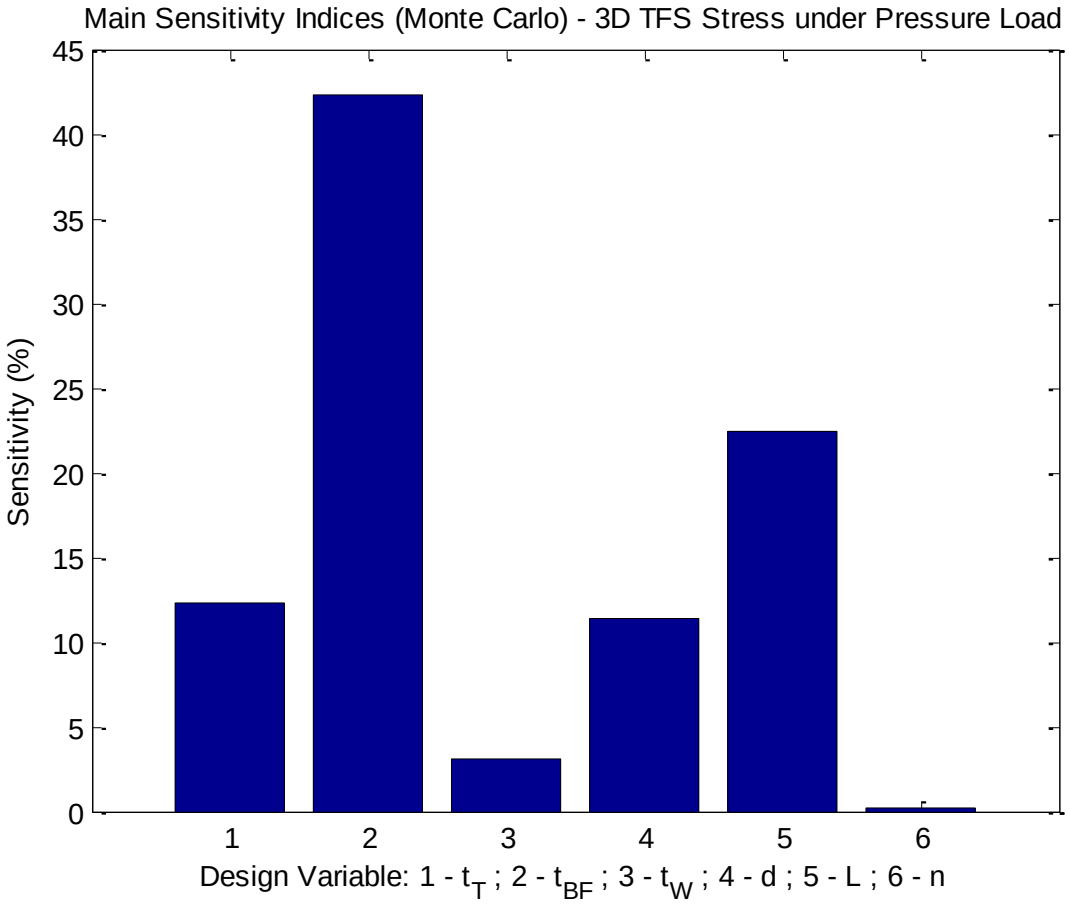

Figure 4-6. Sensitivity indices for the maximum von Mises TFS stress under pressure loading.

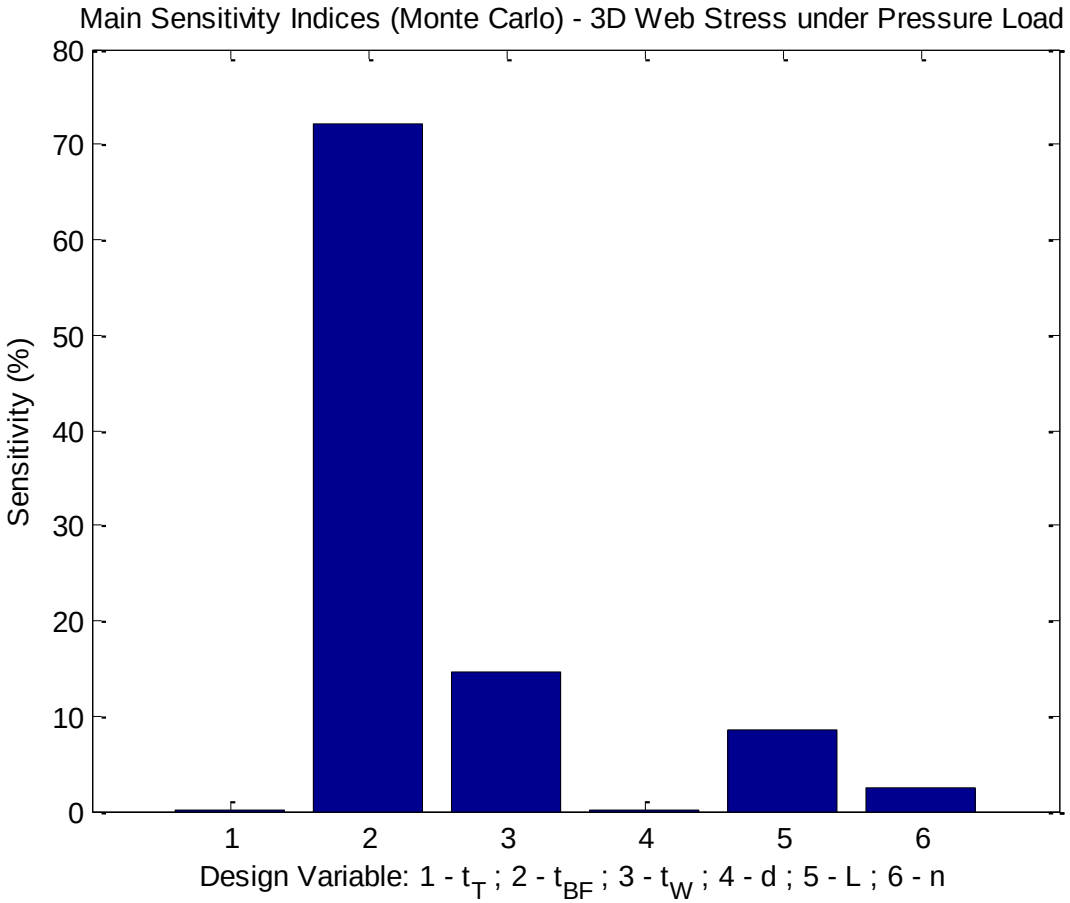

Figure 4-7. Sensitivity indices for the maximum von Mises Web stress under pressure loading.

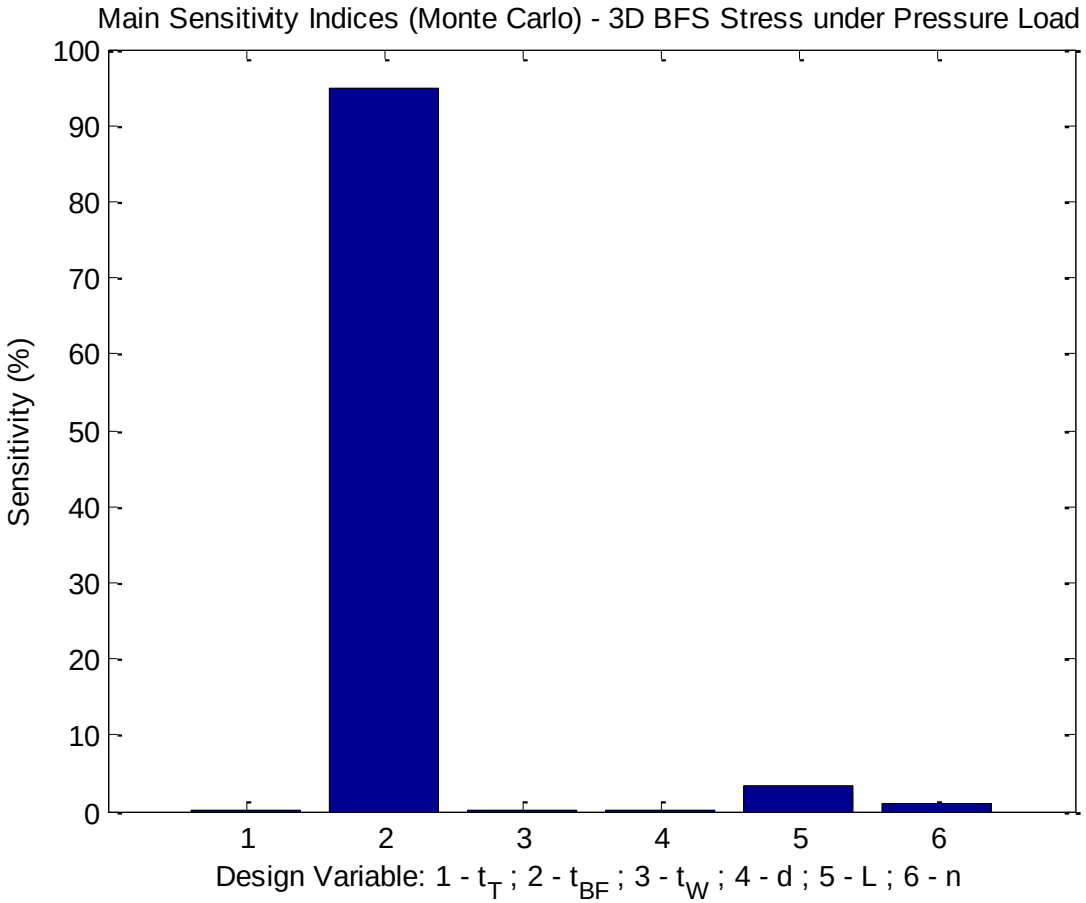

Figure 4-8. Sensitivity indices for the maximum von Mises BFS stress under pressure loading.

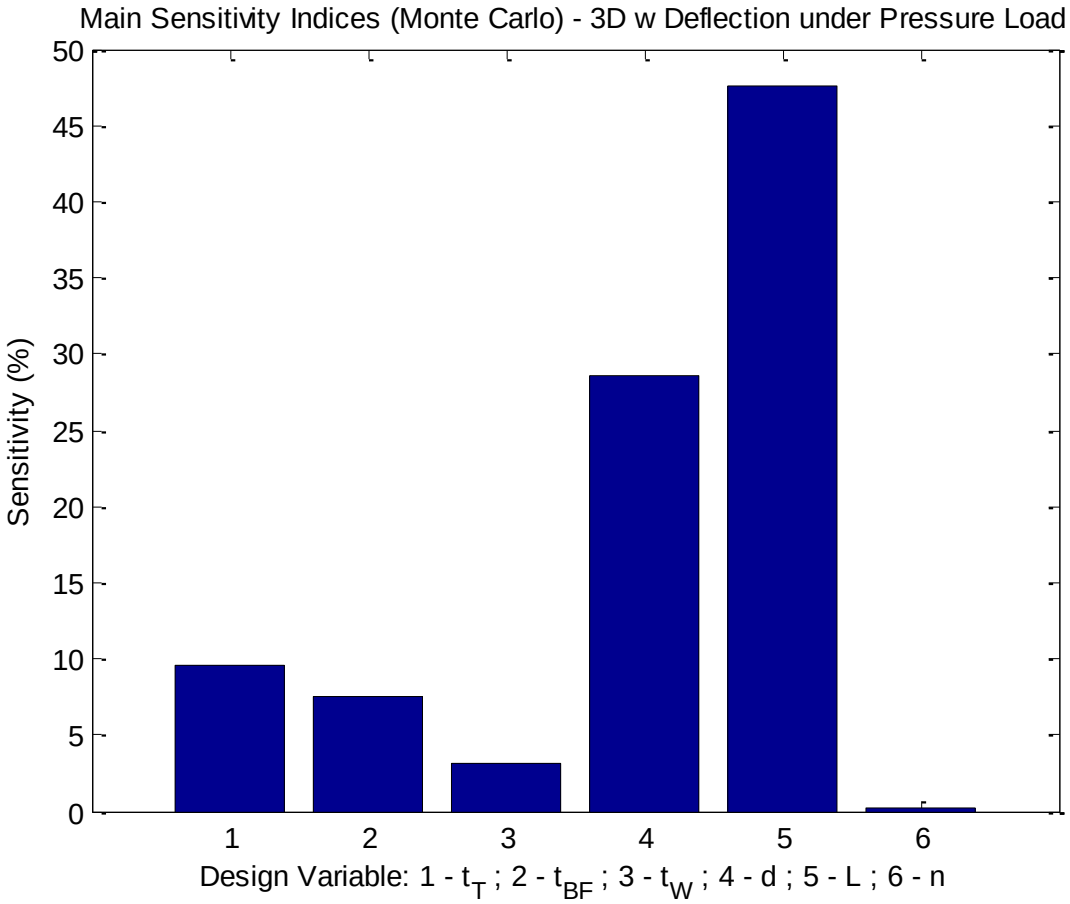

Figure 4-9. Sensitivity indices for the maximum TFS deflection under pressure loading.

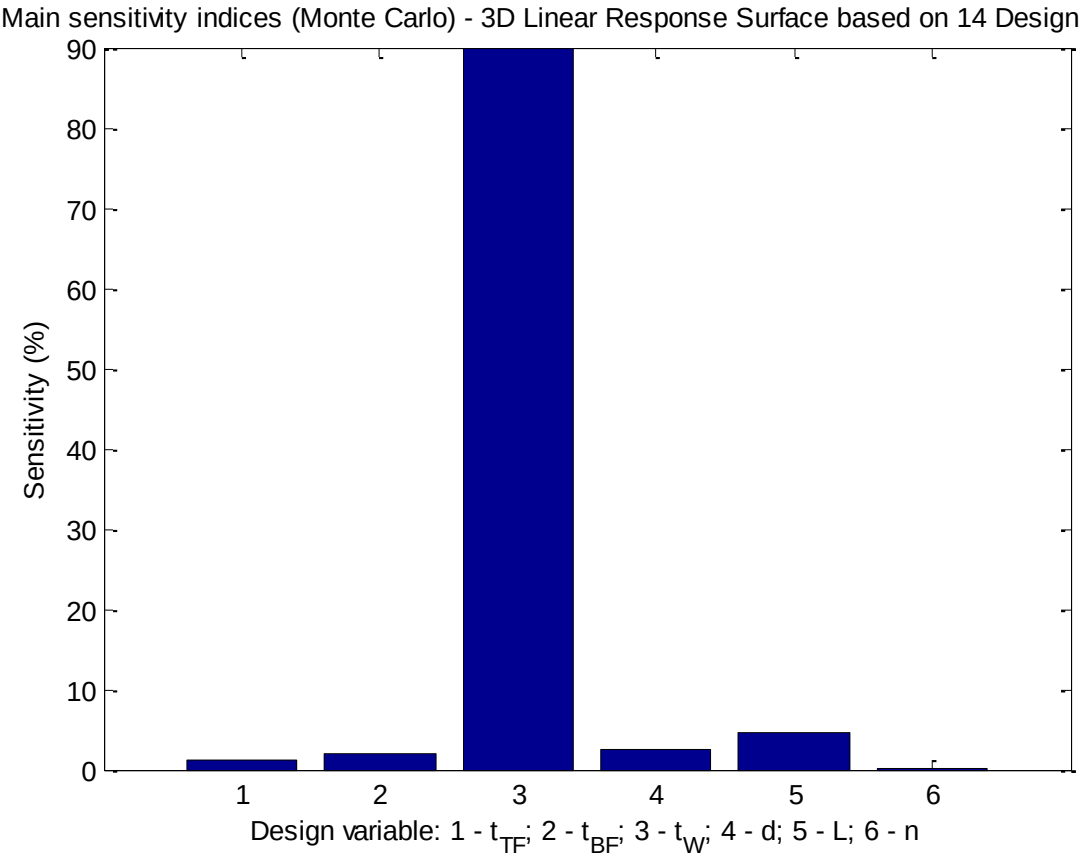

Figure 4-10. Sensitivity indices for the minimum buckling eigen value under pressure loading.

CHAPTER 5
CONCLUSIONS

Summary

A brief overview of this research and findings are presented in this chapter. The summary of the studies is mentioned with appropriate conclusions. Finally, recommendations for further studies are presented. For any hypersonic re-entry vehicle, thermal protection system (TPS) is one of the most critical structures. It protects the vehicle from extreme re-entry temperatures. Future vehicles will require an efficient, reusable, and advanced TPS technology that will provide the hypersonic vehicle with the necessary protection from the extreme reentry environments as well as the cost and maintenance is low. Chapter 1 discusses various prerequisites of the TPS and the approaches which have been undertaken in the past. A variety of TPS concepts have been reviewed and summarized. One such concept is the ITPS, which is the subject of this dissertation. Knowing the underlying challenges of this ITPS development, the specific objectives and purpose of the dissertation were laid out, which was to develop FE based micro-mechanics methods and reverse homogenization method to predict the behavior of any sandwich structure. This 2D FE based method has some limitation and hence the accuracy of the method was improved further using the multi-fidelity approach.

Chapter 2 contains the FE based homogenization procedure that is implemented to determine the equivalent stiffness of the ITPS. This includes the extensional, bending, coupling and shear stiffnesses of the sandwich structure. The result of different stiffnesses is validated by comparing the maximum deflection under a transverse pressure load between the 2D homogenized model and the 3D ITPS panel.

Chapter 3 discusses the detailed FE based reverse homogenization procedure to predict the out of plane displacements and von Mises stresses under thermal and pressure load from the 2D plate model. However, the plate model cannot capture the local stresses and deflection in the TFS due to the transverse pressure load acting on it. Therefore, a unit cell analysis approach is done in order to capture the local effects of the pressure. Also, using the method of sub structuring, a unit cell buckling eigen value analysis is done and compared with the corresponding 3D buckling eigen value analysis.

Chapter 4 describes the various types of multi-fidelity approaches undertaken to improve the accuracy of the 2D method. It was also seen that one could select the best of the various alternative response surfaces, just based on the standard errors in the fit. Using these response surfaces, the ITPS is optimized for minimum mass design. The optimum design variables are obtained by minimizing the ITPS mass by satisfying all the thermal protection systems requirements and limitation in the form of mathematical constraints.

Concluding Remarks

A number of conclusions were explained at the end of each chapter. Some general conclusions drawn from this research work are listed below.

- The FE based homogenization and reverse homogenization is very robust and could be performed with any commercially available FE program. One can choose any material and dimension to implement on any sandwich structure (e.g., Z-cores, C-cores, and truss cores) and still be able to predict an accurate stiffness of the given structure.
- Generally, the transverse shear stiffness is constant for a given cross-section. Unique transverse shear stiffness could not be found. Instead if one wants to select constant transverse shear stiffness, the best one will depend on the number of unit cells.

- Difference between maximum deflection prediction from the 3D and 2D was less than 6%, indicating that the transverse shear stiffness prediction A_{44} and A_{55} is accurate.
- 2D approach can only work for *L/h* ratio greater than 8. Shorter *L/h* ratio could not effectively predict the stiffnesses as the boundary effects comes into play.
- For a given transverse pressure load, maximum deflection occurs for rectangular webs whereas minimum deflection occurs for triangular web configuration.
- Prediction of the buckling eigen value by using the method of sub structuring shows approximately 6-10% difference from the 3D buckling analysis under thermal loads.
- The low fidelity 2D finite element model is fitted with a high quality surrogate, which is corrected by the use of a small number of high fidelity 3D finite element analyses. By doing this multi-fidelity approach, one can substantially improve the accuracy of the fit without doing large number of 3D finite element analysis.
- One can choose the best correction model based on the data without the test points, and the test points also confirmed the choice.

Recommendations

Now that a general framework for FE based homogenization and reverse homogenization procedure has been established with this research work, new structure geometries can be explored. For the corrugated core design, buckling of the edges is one of the major factors influencing the design. For example, buckling of the web-edges close to the panel edges under thermal load is one of the first buckling modes. By tactically placing stiffeners in the webs and face sheets, such buckling modes can be prevented. Stiffeners do not add to the weight or heat conduction path of the ITPS significantly, while drastically improving the buckling resistance of the structure. Therefore, this line of design enhancement has a possibility for reducing the ITPS weight significantly.

Another thing which was done for this research was that the unit cells were of equal lengths. Instead unit cells of different length could be tried. Also there could be

large number of webs near the boundaries as most of the design drivers are near the boundaries. One can also use thicker webs near the boundaries and thinner webs at the center as they do not have high stresses near the center. Plane loads were not tried in this research. Adding in plane loads could make the design even heavier.

We also found that the transverse shear stiffness for a corrugated core structure is very high in one direction (along *x*) as compared to the other direction (along *y*). This is a very unbalanced structure. One suggestion is that we can use corrugations in both the directions (Figure 5-1). This way the shear stiffness can be equally distributed.

Three different types of correction approaches have been discussed in Chapter 4. There is another type of correction technique that can be applied for the multi-fidelity approach. This technique is called as space mapping. Suppose we have two design variables, we can generate a linear response surface based on these two design variables. We need to find the values of α, β, and γ, such that for that corresponding value, my 2D response surface will be closer to the 3D values. This is different type of multi-fidelity response surface and it is also represented in Equation 5-1 below.

$$S^{3D}(x_1, x_2) = S^{2D}(\alpha x_1 + \beta x_2 + \gamma) \tag{5-1}$$

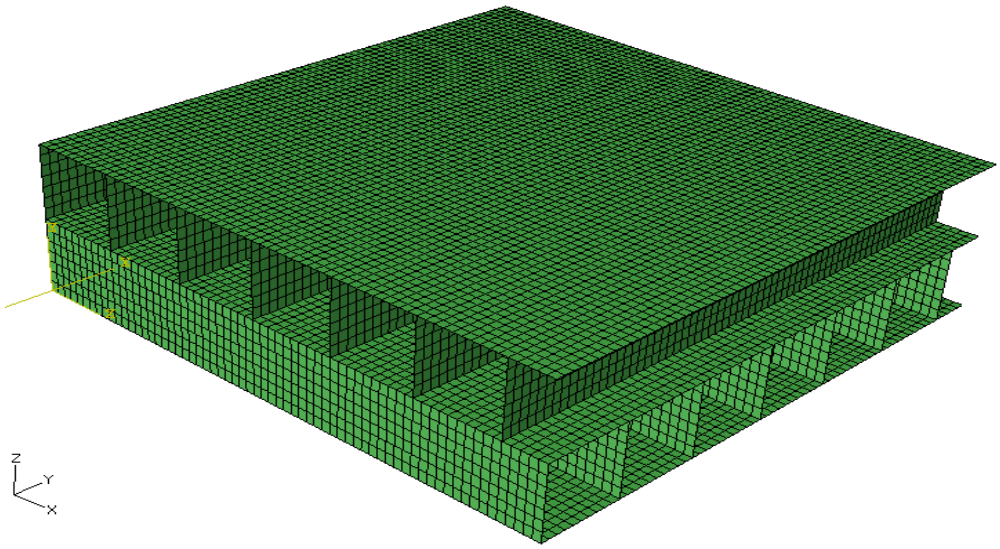

Figure 5-1. Sandwich structure with web corrugations in both *x*- and *y*- directions.

APPENDIX
MATERIAL PROPERTIES USED FOR THE RESEARCH WORK

Material Properties for Titanium Alloy: Ti-6Al-4V

Density: 4428.79 kg/m^3

Poisson's ratio: 0.31

Table A-1. Thermal conductivity, specific heat, and coefficient of thermal expansion of Ti-6Al-4V.

Thermal Conductivity (W/m/K)	Temperature (K)	Specific heat (J/kg/K)	Temperature (K)	CTE (K^{-1})	Temperature (K)
1.545	24	562.706	277.83	6.22E-06	17.06
5.002	147.44	547.215	362.44	7.82E-06	105.67
7.011	272.28	594.107	531.67	8.58E-06	248.36
7.551	356.83	625.508	613.56	9.12E-06	411.78
8.221	435.89	703.801	784.11	9.57E-06	569.61
9.992	563.56	751.112	871.33	1.01E-05	759.44
10.857	623.17	798.423	950.78	1.03E-05	956.33
12.477	741.17	866.249	1030.78	1.03E-05	1041.89
13.846	866.33	908.117	1094.67	1.03E-05	1137.44
14.365	921.89	944.961	1143.56		

Table A-2. Young's modulus and yield stress of Ti-6Al-4V.

Young's Modulus (GPa)	Temperature (K)	Yield Stress (MPa)	Temperature (K)
1.29E+11	19.83	1.61E+09	27.17
1.14E+11	172	1.28E+09	118.44
1.13E+11	229.49	1.19E+09	149.72
1.10E+11	288.47	1.10E+09	178.67
1.07E+11	338.61	1.03E+09	210.91
1.03E+11	390.22	9.53E+08	253.23
9.53E+10	497.83	8.11E+08	349
9.19E+10	552.44	7.54E+08	386.78
8.83E+10	602.56	6.90E+08	428
8.20E+10	695.44	5.87E+08	518.17
7.81E+10	735.28	5.57E+08	574.94
7.24E+10	766.22	5.38E+08	638.44
6.46E+10	791.28	5.13E+08	693
5.68E+10	810.5	4.81E+08	806.56
4.96E+10	866.33		
4.41E+10	921.89		
3.86E+10	977.44		

Material Properties for Beryllium Alloy

Density: 1855 kg/m^3

Poisson's ratio: 0.063

Table A-3. Thermal conductivity, Specific heat, and coefficient of thermal expansion of beryllium alloy.

Thermal Conductivity (W/m/K)	Temperature (K)	Specific heat (J/kg/K)	Temperature (K)	CTE (K^{-1})	Temperature (K)
180.618	279.18	1775.622	2.58E+02	1.11E-05	265.02
174.05	299.17	2025.574	3.44E+02	1.14E-05	295.41
160.648	365.22	2160.389	3.92E+02	1.22E-05	366
137.527	493.67	2565.671	5.83E+02	1.36E-05	529.83
127.764	571.67	2740.679	7.17E+02	1.40E-05	581.22
118.001	661.11	2838.65	7.96E+02	1.45E-05	688
109.48	754.56	2990.631	9.53E+02	1.48E-05	733.72
102.158	840.22	3054.689	1029.667	1.53E-05	840.78
94.88	933.56	3159.359	1165.222	1.55E-05	884.11
88.756	1026.89	3206.67	1216.889	1.57E-05	966.33
85.117	1.11E+03	3324.738	1345.778	1.58E-05	1015.78
79.037	1.21E+03	3382.097	1399.111	1.60E-05	1090.22
75.354	1.32E+03	3486.767	1490.222	1.61E-05	1137.44
71.715	1.40E+03	3533.659	1534.667	1.63E-05	1198.56
69.274	1.47E+03	3628.281	1622.444		

Table A-4.Young's modulus and yield stress of beryllium alloy.

Young's Modulus (GPa)	Temperature (K)	Yield Stress (MPa)	Temperature (K)
2.93E+11	2.56E+02	3.44E+08	256.9
2.91E+11	2.83E+02	3.45E+08	280.33
2.89E+11	3.71E+02	3.32E+08	334.89
2.86E+11	4.21E+02	3.20E+08	371.5
2.79E+11	5.21E+02	2.98E+08	455.67
2.73E+11	5.70E+02	2.83E+08	508.67
2.52E+11	6.87E+02	2.46E+08	624.83
2.32E+11	7.63E+02	2.10E+08	708.22
2.22E+11	797.61	1.93E+08	740.94
1.87E+11	871.89	1.56E+08	806.39
1.71E+11	899.11	1.38E+08	834.67
1.38E+11	954.11	1.06E+08	883
1.19E+11	981.89	9.01E+07	908
8.54E+10	1028	5.66E+07	959.11
7.19E+10	1049.11	4.35E+07	988

LIST OF REFERENCES

[1] Hunt, J. L., Lockwood, M. K., Petley, D. H., & Pegg, R. J. (1997, January). Hypersonic Airbreathing Vehicles Visions and Enhancing Technologies. Proceedings of the Space Technology and Applications International Forum, Albuquerque, NM, 387, 12851296.

[2] Blosser, M. L. (1996). Development of metallic thermal protection systems for the reusable launch vehicle. NASA TM110296.

[3] Christiansen, E. L., & Friesen, L. (1997). Penetration for thermal protection materials. International Journal of Impact Engineering, 20, 153164.

[4] Behrens, B., and Müller, M. (2004). Technologies for thermal protection systems applied on reusable launcher. Acta Astronautica, 55(39), 529536.

[5] Bohon, H. L., Shideler, J. L., & Rummler, D. R. (1977). Radiative metallic thermal protection systems: a status report. Journal of Spacecraft, 14(10), 626631.

[6] Bekey, I., Powell, R., Austin, R., "NASA Studies Access to Space," *Aerospace America*, Vol. 32, No. 5, May 1994, pp. 38–43.

[7] Futron Corporation, "Space Transportation Costs: Trends in Price Per to Orbit 1990 – 2000," Bethesda, MD: Author.

[8] Blosser, M. L., Chen, R. R., Schmidt, J. T., Dorsey, J. T., Poteet, C. C., Bird, R. K., & Wurster, K. E. (2004). Development of advanced thermal protection system prototype hardware. Journal of Spacecraft and Rockets, 41(2), 183194.

[9] Blosser, M. L., "Advanced Metallic Thermal Protection Systems for Reusable Launch Vehicles," *Ph.D. Dissertation*, University of Virginia, May 2000.

[10] Dorsey, J. T., Poteet, C. C., Wurster, K. E., and Chen, R. R., "Metallic Thermal Protection System Requirements, Environments, and Integrated Concepts," *Journal of Spacecraft and Rockets*, Vol. 41, No. 2, Mar–Apr 2004, pp. 162–172.

[11] Erb, R. B., Greenshields, D. H., Chauvin, L. T., Pavlosky, J. E., and Statham, C. L, "Apollo Thermal-Protection System Development," *Journal of Spacecraft (and Rockets)*, Vol. 7, No. 6, June 1970, pp. 727–734.

[12] Lee, G., "Ablation Effects on Apollo Afterbody Heat Transfer," *AIAA Journal*, Vol. 7, No. 8, 1969, pp. 1616–1618.

[13] Braun, R. D., Powell, R. W., Evans Lyne, J., "Earth Aerobraking Strategies for Manned Return from Mars," *Journal of Spacecraft and Rockets*, Vol. 29, No. 3, May–June 1992, pp. 297–304.

[14] Williams, S. D., Curry, D. M., Bouslog, S. A., Rochelle, W. C., “Thermal Protection System-Design Studies for Lunar Crew Module,” *Journal of Spacecraft and Rockets*, Vol. 32, No. 3, May–Jun 1995, pp. 456–462.

[15] Bartlett, E. P., Anderson, L. W., and Curry, D. M., “An Evaluation of Ablation Mechanisms for the Apollo Heat Shield Material,” *Journal of Spacecraft (and Rockets)*, Vol. 8, No. 5, May 1971, pp. 463–469.

[16] Boynton, J. H., and Kleinknecht, K. S., “Systems Design Experience from Three Manned Space Programs,” *Journal of Spacecraft (and Rockets)*, Vol. 7, No. 7, 1970, pp. 770 – 784.

[17] Lyne, J. E., Tauber, M. E., Braun, R. D, “Parametric Study of Manned Aerocapture. 1. Earth Return from Mars,” *Journal of Spacecraft and Rockets*, Vol. 29, No. 6, Nov–Dec 1992, pp. 808–813.

[18] Zhu, H. (2004). Design of metallic foams as insulation in thermal protection systems. Unpublished Ph.D. dissertation, University of Florida, Gainesville, FL.

[19] Cooper, P. A., and Holloway, P. F., “The Shuttle Tile Story,” *Astronautics and Aeronautics*, Jan 1981, pp. 24–34.

[20] Bapanapalli, S.K. (2007). Design of an integral thermal protection system for future space vehicles. Unpublished Ph.D. dissertation, University of Florida, Gainesville, FL.

[21] Martinez, O. (2007). Micromechanical analysis and design of an integrated thermal protection system for future space vehicles. Unpublished Ph.D. dissertation, University of Florida, Gainesville, FL.

[22] Poteet, C. C., Abu-Khajeel, H., and Hsu, S.Y., “Preliminary Thermal-Mechanical Sizing of a Metallic Thermal Protection System,” *Journal of Spacecraft and Rockets*, Vol. 41, No. 2, Mar–Apr 2004, pp. 173–182.

[23] Blosser, M. L., “Fundamental Modeling and Thermal Performance Issues for Metallic Thermal Protection System Concept,” *Journal of Spacecraft and Rockets*, Vol. 41, No. 2, Mar–Apr 2004, pp. 195–206.

[24] Glass, D.E.,”Ceramic Matrix Composite (CMC) Thermal Protection Systems (TPS) and Hot Structures for Hypersonic Vehicles”, 15th Space plane and Hypersonic Systems and Technologies Conference, AIAA 2008–2682.

[25] Glass, D. E., Camarda, C. J., “Preliminary Thermal/Structural analysis of a Carbon-Carbon/Refractory-Metal Heat-Pipe-Cooled Wing Leading Edge, Thermal Structures and Materials for High Speed Flight,” edited by E. A. Thornton, Vol. 140, *Progress in Astronautics and Aeronautics*, AIAA, Washington D.C., 1992, pp. 301–322.

[26] Stewart, J. D., & Greenshields, D. H. (1969). Entry vehicles for space programs. Journal of Space and Rockets, 6(10), 10891102.

[27] Laub, B. & Venkatapathy, E., “Thermal protection system technology and facility needs for demanding future planetary missions”. Proceedings of the International Workshop Planetary Probe Atmospheric Entry and Descent Trajectory Analysis and Science, 6–9 October 2003, Lisbon, Portugal. ESA Publications Division, ISBN 92-9092-855-7, 2004, p. 239–247.

[28] Lyle, K.H., & Fasanella, E.L., "Permanent set of the Space Shuttle Thermal Protection System Reinforced Carbon–Carbon material",Journal of Composites, Part A 40 (2009) 702–708.

[29] http://science.ksc.nasa.gov/shuttle/technology/sts-newsref/sts-tps.html.

[30] Leiser, Daniel B., “Shuttle Thermal Protection System”, American Ceramic Society Bulletin; Aug2004, Vol. 83 Issue 8, p44–47.

[31] Surface Heating Effects of X-33 Vehicle Thermal-Protection-System Panel Bowing, Palmer, G., and Sherman, B., Journal of Spacecraft and Rockets, Vol. 36, No. 6, November–December 1999.

[32] Norris, B., “Fabrication and Evaluation of ODS Structural Sandwich Panels for Lightweight, Very High Temperature, Aerospace Applications,”, Proceedings of the 14th International Plansee Seminar, RM28, 1997, p. 263.

[33] Jager, H., et al., “Forging of Nickelbase-ODS-Alloys”, Proceedings of the 13th International Plansee Seminar, RM 90, 1993, p. 782.

[34] Inco Alloys Handbook, “Inconel Alloy 617,” Inco Alloys International, Inc., Publication IAI–38, Huntington,WV, 1988, p. 55–60.

[35] Thornton, E. A.(1992). Thermal structures: 4 decades of progress. Journal of Aircraft, 29(3), 485498.

[36] Blosser, M., "Thermal Protection Systems for Reusable Launch Vehicles”, Short Course: Thermal Control Hardware, Thermal & Fluids Analysis Workshop, Hampton, VA, August 22, 2003.

[37] Scotti, S.J., Clay, C., Rezin, M.,"Structural and Materials Technologies for Extreme Environments Applied to Reusable Launch Vehicles", AIAA/ICAS International Symposium and Exposition, AIAA–2003–2697.

[38] Myers, D.E., Martin, C.J., and Blosser, M. L., "Parametric Weight Comparison of Advanced Metallic, Ceramic Tile, and Ceramic Blanket Thermal Protection Systems",NASA/TM–2000–210289.

[39] Chiu, S.A., and Pitts, W.C.,"Reusable Surface Insulation for Reentry Spacecraft", AIAA Paper 91–0695, 29th Aerospace Sciences Meeting, Jan. 1991.

[40] DiChiara, R.A.,"Thermal insulation system employing oxide ceramic matrix composites", US Patent App. 10/689,809, 2003.

[41] Hirose, Y., Matsuda, H., Matsubara, G., Inamura, F., Hojo, M.,"Evaluation of New Crack Suppression Method for Foam Core Sandwich Panel Via Fracture Toughness Tests and Analyses Under Mode-I Type Loading", Journal of Sandwich Structures, Vol. 11, No. 6, p. 55–60.

[42] Hyun, S., Karlsson, A. M., Torquato, S., Evans, A. G., “Simulated Properties of Kagome and Tetragonal Truss Core Panels,” *International Journal of Solids and Structures*, Vol. 40, 2003, pp. 6989–6998.

[43] Valdevit, L., Hutchinson, J. W., Evans, A. G., “Structurally Optimized Sandwich Panels with Prismatic Cores,” *International Journal of Solids and Structures*, Vol. 41, 2004, pp. 5105–5124.

[44] Rathbun, H. J., et al, “Measurement and Simulation of the Performance of a Lightweight Metallic Sandwich Structure with a Tetrahedral Truss Core,” *Journal of Applied Mechanics-Transaction of ASME*, Vol. 71, May 2004, pp. 368–374.

[45] Wei, Z., Zok, F. W., Evans, A. G., “Design of Sandwich Panels with Prismatic Cores,” *Journal of Engineering Materials and Technology – Transactions of ASME*, Vol. 128, April 2006, pp. 186–192.

[46] Rathbun, H. J., Zok, F. W., Evans, A. G., “Strength Optimization of Metallic Sandwich Panels Subject to Bending,” *International Journal of Solids and Structures*, Vol. 42, 2005, pp. 6643–6661.

[47] Zok, F. W., Rathbun, H. J., Wei, Z., Evans, A. G., “Design of Metallic Textile Core Sandwich Panels,” *International Journal of Solids and Structures*, Vol. 40, 2003, pp. 5707–5722.

[48] Zenkert, D., "An Introduction to Sandwich Construction", Chamelon Press, London, 1997.

[49] Vinson, J. R., "The Behavior of Sandwich Structures of Isotropic and Composite Materials", Technomic, Lancaster, 1999.

[50] Chang, W., Venstel, E., Krauthammer, T., & John, J. (2005). Bending behavior of corrugatedcore sandwich plates. Composite Structures, 70(1), 8189.

[51] Libove, C., & Batdorf, S. B. (1948). A general small deflection theory for flat sandwich plates. National Advisory Committee for Aeronautics Technical Note (NACA TN) 1526.

[52] Libove, C., & Hubka, R. E. (1951). Elastic constants for corrugated core sandwich plates. National Advisory Committee for Aeronautics Technical Note (NACA TN)2289.

[53] Wicks, N., Hutchinson, J. W., “Optimal Truss Plates,” *International Journal of Solids and Structures*, Vol. 38, 2001, pp. 5165–5183.

[54] Wicks, N., Hutchinson, J. W., “Performance of Sandwich Plates with Truss Cores,” *Mechanics of Materials*, Vol. 36, 2004, pp. 739–751.

[55] Fung, T. C., Tan, K. H., & Lok, T. S. (1994), "Elastic constants for zcore sandwich panels", Journal of Structural Engineering, 120(10), 30463065.

[56] Fung, T. C., Tan, K. H., & Lok, T. S. (1996), "Shear stiffness dQy for ccore sandwich panels", Journal of Structural Engineering, ASCE, 122(8), 958966.

[57] Lok, T. S., & Cheng, Q. (2000), "Elastic stiffness properties and behavior of trusscore sandwich panel", Journal of Structural Engineering, 126(5), 552559.

[58] Lok, T. S., Cheng, Q. H., and Heng, L. (1999), "Equivalent stiffness parameters of truss-core sandwich panel", Proc., 9th Int. Offshore and Polar Eng. Conf., Vol. 4, 282–288.

[59] Carlsson, L. A., Nordstrand. T., & Westerland, B. (2001), "On the elastic stiffnesses of corrugated core sandwich", Journal of Sandwich Structures and Materials, 3, 253267.

[60] Biancolini, M.E., “Evaluation of equivalent stiffness properties of corrugated board,” Composite Structures, 69 (2005), 322 – 328.

[61] Buannic, N., Cartraud, P., Quesnel T., “Homogenization of corrugated core sandwich panels,” Composite Structures, 59 (2003), 299 – 312.

[62] Nordstrand, T., Carlsson, L.A., Allen, H.G., "Transverse shear stiffness of structural core sandwich", Journal of Composite structures, 1994;27:317–329.

[63] Talbi, N., Batti, A., Ayad, R., Guo, Y. Q., "An analytical homogenization model for finite element modelling of corrugated cardboard", Journal of Composite Structures 88 (2009) 280–289.

[64] Isaksson, P., Krusper, A., Gradin, P.A., "Shear correction factors for corrugated core structures", Journal of Composite Structures 80 (2007) 123–130.

[65] Martinez, O., Sankar, B.V., Haftka, R., Blosser, M., Bapanapalli, S.K. (2007), “Micromechanical Analysis of a Composite Corrugated-Core Sandwich Panel for Integral Thermal Protection Systems,” *AIAA Journal,* 45(9), 2323–2336.

[66] Martinez, O., Bapanapalli, S.K., Sankar, B.V., Haftka, R., Blosser, M., “Micromechanical Analysis of a Composite Truss-Core Sandwich Panels for Integral Thermal Protection Systems,” *47th AIAA/ASME/ASCE/AHS/ASC Structures, Structural Dynamics, and Materials Conference*, Newport, RI, May 2006.

[67] Bapanapalli, S.K., Martinez, O., Gogu, C., Sankar, B.V., Haftka, R., "Analysis and Design of Corrugated-Core Sandwich Panels for Thermal Protection Systems of Space Vehicles", 47th AIAA/ASME/ASCE/AHS/ASC Structures, Structural Dynamics, and Materials Conference, Newport, RI, May 2006.

[68] Copenhaver, D. C., Scott, E.P., Hanuska, A., "Thermal characterization of honeycomb core sandwich structures", Journal of Spacecraft and Rockets; 1998, vol.35 no.4 (539–545).

[69] Martinez, O., Sharma, A., Sankar, B.V., Haftka, R., “Thermal Force and Moment Determination of an Integrated Thermal Protection System,” *AIAA Journal,* 48(1), January, 2010.

[70] Sharma, A., Gogu, C., Martinez, O.M., Sankar, B.V., Haftka, “Multi-Fidelity Design of an Integrated Thermal Protection System for Spacecraft Reentry”, AIAA Paper 2008-2062, 49th AIAA Multidisciplinary Design Optimization Specialists Conference, Schaumburg, Illinois, 7–10 April 2008.

[71] Vitali, R., Haftka, R.T., Sankar, B.V., "Multi-fidelity design of stiffened composite panel with a crack", Volume 23, Number 5 / June, 2002, Pages 347–356.

[72] Haftka, R.T. 1991, "Combining global and local approximations", AIAA J. 29, 1523–1525.

[73] Chang, K.J.; Haftka, R.T.; Giles, G.L.; Kao, P.J. 1993, "Sensitivity-based scaling for approximating structural response", J. Aircraft 30, 2, 283–287.

[74] Toropov, V.V.; Keulen, F.V.; Markine, V.L.; Alvarez, L.F. 1999, "Multipoint approximation based on response surface fitting", a summary of recent developments. First ASMO UK/ISSMO (held in Ilkley, UK), pp. 371–380.

[75] Mason, B.H.; Haftka, R.T.; Johnson, E.R.; Farley, G.L 1994, "Variable complexity design of composite fuselage frames by response surface techniques", Thin Wall Struct. 32, 235–261.

[76] Kaufman, K.; Balabanov, V.; Burgee, S.L.; Giunta, A.A.; Grossman, B.; Mason, W.H.; Watson, L.T. 1996; "Variable complexity response surface approximation for wing structural weight in HSCT design", Comp. Mech. 18, 112–126.

[77] Vitali, R.; Park, O.; Haftka, R.T.; Sankar, B.V. 1997; "Structural optimization of a hat stiffened panel by response surface techniques", Proc. 38th AIAA/ASME/ASCE/AHS/ ASC Structures, Structural Dynamics and Materials Conf. (held in Kissimmee, FL), Vol. 4, pp. 2983–2993.

[78] Vitali, R.; Haftka, R.T.; Sankar, B.V. 1998; "Correction response approximation for stress intensity factors for composite stiffened plates", Proc. 39th AIAA/ ASME/ASCE/AHS /ASC Structures, Structural Dynamics and Materials Conf. (held in Long Beach, CA), Vol. 4, pp. 2917–2922.

[79] Vitali, R.; Haftka, R.T.; Sankar, B.V. 1999; "Multi-fidelity design of stiffened composite panel with a crack", WCSMO–3, Third World Congr. of Structural and Multidisciplinary Optimization (held in Buffalo, NY), CD-Rom.

[80] Knill, D.L.; Giunta, A.A.; Baker, C.A.; Grossman, B.; Mason, W.H.; Haftka, R.T.; Watson, L.T. 1999; "Response surface model combining linear and euler aerodynamics for supersonic transport design", J. Aircraft 36, 75–86.

[81] Balabanov, V.; Giunta, A.A.; Golovidov, O.; Grossman, B.; Mason, W.H.; Watson, L.T.; Haftka, R.T. 1999; "A reasonable design space approach to response surface approximations", J. Aircraft 36, 308–315.

[82] Sharma, A., Sankar, B.V., Haftka, “Multi-Fidelity Analysis of Corrugated-Core Sandwich Panels for Integrated Thermal Protection Systems”, AIAA Paper 2009-2201, AIAA/ASME/ASCE/AHS/ASC Structures, Structural Dynamics, and Materials Conference, Palm Springs, California, 4–7 May 2009.

[83] Haftka, R. T., Gurdal, Z. (1992). Elements of Structural Optimization (3 rd ed.). Dordrecht, The Netherlands: Kluwer Academic Publishers.

[84] Queipo, V.N., Haftka, R. T., Shyy W., Goel, T., Vaidyanathan, R., Tucker, P.K., “Surrogate-based analysis and optimization”, Progress in Aerospace Sciences 41 (2005) 1–28.

[85] Whitney, M., Structural Analysis of Laminated Anisotropic Plates, Technomic, Lancaster, PA, 1987.

BIOGRAPHICAL SKETCH

Anurag Sharma received his Bachelor of Engineering degree in mechanical engineering from BMS College of Engineering, Bangalore, India in 2005. Between 2005 and 2006, he worked for a software company, Silver Software Private Limited, as a software engineer in India. In August 2006, he was admitted to the graduate program in the Department of Mechanical and Aerospace Engineering at the University of Florida where he is currently completing the requirements for a Doctor of Philosophy degree in mechanical engineering at the University of Florida. Upon graduation, he will be working as a module and integration yield engineer for Intel Corporation in Hillsboro, Oregon.